New Concepts in Quantum Metrology: Dynamics, Machine Learning, and Bounds on Measurement Precision

DISSERTATION

vorgelegt von
LUKAS J. FIDERER
aus Baden-Baden

Tübingen

2019

Abstract

This cumulative thesis is concerned with theoretical quantum metrology, the theory of measurement and estimation using quantum resources [23, 60]. Possible applications of quantum-enhanced sensors include the measurement of magnetic fields [62, 57], gravitational wave detection [25, 1], navigation [21], remote sensing [2], or the improvement of frequency standards [35].

Many proposals for quantum-enhanced sensors rely on the preparation of non-classical initial states and integrable dynamics [51]. However, such non-classical states are generally difficult to prepare and to protect against decoherence [38, 13]. As an alternative, in this thesis, we propose so-called quantum-chaotic sensors [16] which make use of classical initial states that are easy to prepare while quantum enhancements are applied to the dynamics. This approach is motivated by the insight that quantum chaos and quantum metrology are both characterized by the sensitivity to small changes of the dynamics [26, 41]. At the example of the quantum kicked top model [31], where nonlinear control pulses render the dynamics quantum-chaotic, we explore different dynamical regimes for quantum sensors. Further, we demonstrate that quantum chaos is able to alleviate the detrimental effects of decoherence [16]. In particular, we present a proposal for a quantum-chaotic cesium-vapor magnetometer [8, 17].

With the help of reinforcement learning, we further optimize timing and strength of the nonlinear control pulses for the kicked top model with superradiant damping. In this case, the optimized control policy is identified as a dynamical form of spin squeezing [55].

Another part of this thesis deals with Bayesian quantum estimation [36] and, in particular, with the problem of experiment design heuristics. We train neural networks with a combination of supervised and reinforcement learning to become fast and strong experiment design heuristics [19]. We demonstrate the versatility of this method using examples of single and multi-parameter estimation where the trained neural networks surpass the performance of well-established heuristics [14, 64].

Finally, this thesis deals with a long-time outstanding conjecture in quantum metrology [45]: we prove this conjecture and find an expression for the maximal quantum Fisher information for any mixed initial state and any unitary dynamics, provide conditions for optimal state preparation and optimal control of the dynamics, and utilize these results to prove that Heisenberg scaling can be achieved even with thermal states of arbitrary (finite) temperature [18].

Contents

List of Publications

Accepted Publications

1. Fiderer, L. J. and Braun, D. (2018). Quantum metrology with quantum-chaotic sensors. *Nature Communications*, 9(1):1351

2. Fiderer, L. J. and Braun, D. (2019). A quantum-chaotic cesium-vapor magnetometer. In Shahriar, S. M. and Scheuer, J., editors, *Optical, Opto-Atomic, and Entanglement-Enhanced Precision Metrology*, volume 10934, page 109342S. SPIE.

3. Fiderer, L. J., Fraïsse, J. M. E., and Braun, D. (2019a). Maximal Quantum Fisher Information for Mixed States. *Phys. Rev. Lett.*, 123:250502.

4. Schuff, J., Fiderer, L. J., and Braun, D. (2020). Improving the dynamics of quantum sensors with reinforcement learning. *New Journal of Physics*, 22(3):035001.

Submitted Manuscripts

5. Fiderer, L. J., Schuff, J., and Braun, D. (2020). Neural-Network Heuristics for Adaptive Bayesian Quantum Estimation. *arXiv preprint arXiv:2003.02183*.

Contribution to Publications

No.	Authors	Position of candidate in list of authors	Scientific ideas (%)	Numerical/ analytic calculations (%)	Interpretation of the results (%)	Paper writing (%)
1	Fiderer, Braun	1	10	100	50	50
2	Fiderer, Braun	1	10	100	50	100
3	Fiderer, Fraïsse, Braun	1	50	100	33	50
4	Schuff, Fiderer, Braun	2	50	0	33	50
5	Fiderer, Schuff, Braun	1	90	100	100	100

Table 1 Summary of the candidate's contributions to the publications. Numbers in the left column refer to the numbered publications in the list of publications. Author names are abbreviated. Percentages in the 4 columns from the right are approximations of the candidate's contribution to the publications.

Chapter 1

Introduction

In this chapter we introduce several selected basic concepts of quantum metrology which are essential for the understanding of this work. Note that the publications and manuscripts, and *only* the publications and manuscripts, provide a precise formulation of all results of this thesis and provide an overview of the related literature. Therefore, I would like to refer to the corresponding publications [16–18, 55, 19] (see Appendix) for a precise formulation of results and a summary of the relevant literature.

Quantum metrology is a sub-discipline of quantum information and as such is part of theoretical quantum physics. The objective of quantum metrology is to estimate a parameter or multiple parameters of interest (magnetic fields, temperature, . . .) with the help of quantum experiments. Quantum metrology provides the theoretical framework which relates properties of experiments with the estimation of parameters.

With the objective of quantum metrology in mind, it is clear that we aim to design quantum experiments which allow us to perform parameter estimation in the best possible way. Therefore, it is important to introduce a figure of merit for the estimation of parameters. To this end, we first introduce a model of a paradigmatic quantum experiment in the context of quantum metrology, see Figure 1.1. We distinguish between four steps: (i) state preparation, (ii) dynamics, (iii) measurement, and (iv) processing of the measurement outcomes [23].

The motivation for such a model comes from the insight that parameter estimation based on measurement outcomes requires knowledge about the experiment. Imagine
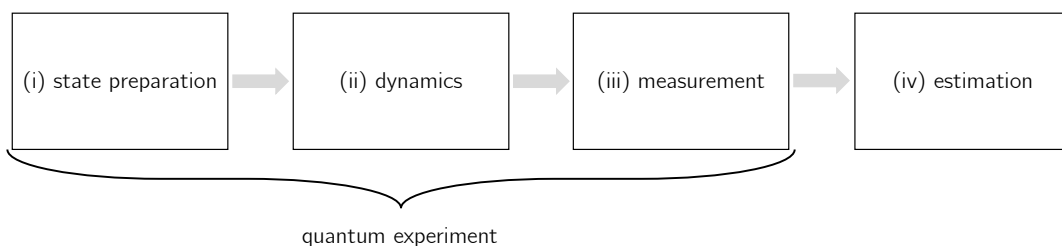

Figure 1.1 Model for a quantum sensor. It consists of a quantum experiment with state preparation, dynamics, and measurement [steps (i) to (iii)] and a post processing of the measurement outcomes [step (iv)].
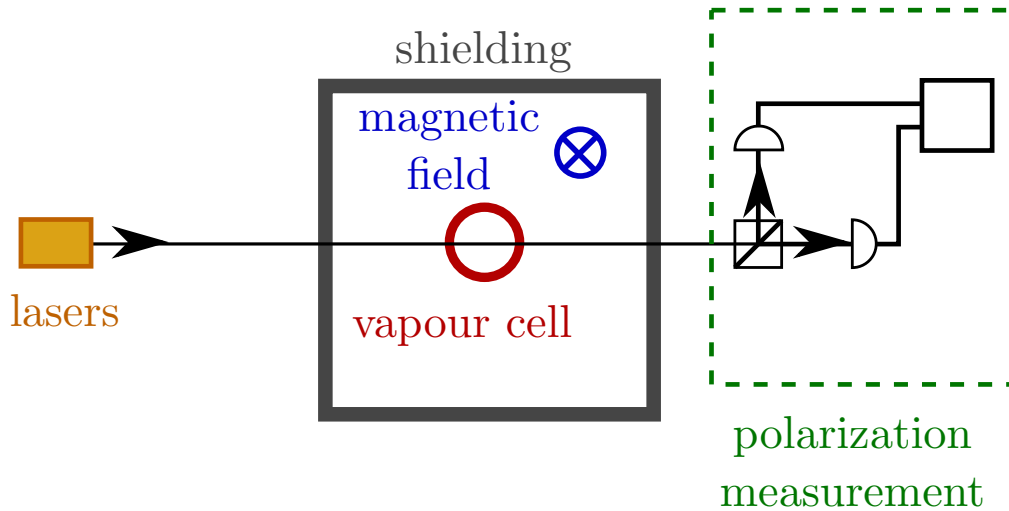
Figure 1.2 Example of a quantum sensor. An alkali-vapor magnetometer with two lasers (depicted as one) for state preparation and readout. State preparation consists of polarizing the spins of the alkali atoms. Readout consists of measuring the (Faraday-rotated) polarization of transmitted (linearly polarized, off-resonant) light. Figure adapted from Ref. [17].

there are unknown, possibly time-dependent influences on the quantum system under consideration. Generally, such influences can have an unknown effect on the (statistic of) measurement outcomes. Then, it will be impossible or at least problematic to infer the parameters of interest from the measurement outcomes because changes in the measurement outcomes may either originate from changes in the parameters of interest or from the unknown influences. This is the reason why we aim to design experiments where the only unknown influences on the statistic of measurement outcomes is given by the parameters of interest.

In step (i), a quantum system is prepared in an initial state. For example, consider the problem of magnetic field estimation with the spins of atoms at room temperature [3, 54, 11, 56], see Figure 1.2. Given a bunch of atoms with non-zero atomic spin in a vapor cell, we want to prepare the collective spin of these atoms in a polarized state, i.e., ideally all the individual spins are oriented equally. This can, for instance, be achieved with a laser pulse. In this way we avoid that the measurement outcomes will be determined by the otherwise random orientation of the atomic spins. However, there are effects competing with the optical polarization process, for instance, originating from interactions between the atoms [4]. In such cases, the process of state preparation itself requires an appropriate model such that we know the resulting prepared state. Let us denote the initial state by ρ, which is a density matrix that characterizes the initial state.

In step (ii), the quantum system is subjected to a dynamics. The purpose of this step is to encode the parameters of interest in the state of the quantum system. Information is transferred from an environment to the quantum system. This means that the resulting state, after the dynamics, depends on these parameters (unless an

eigenstate of the dynamics was prepared in step (i); obviously, it does not make much sense to do this). Let us denote the parameters that we want to estimate by a vector $\boldsymbol{\theta} = (\theta_1, \theta_2, \dots)$ where θ_j is the jth parameter of interest. In case of single-parameter estimation, $\boldsymbol{\theta}$ is replaced by a scalar θ. The dynamics can be described by a quantum channel, a completely positive and trace-preserving map from density matrices to density matrices. Unitary dynamics is a special case that is often considered for idealized models of quantum sensors. Let us denote the state after the dynamics as $\rho(\boldsymbol{\theta})$.

Returning to our example of magnetic field estimation with atomic spins, let us assume that we know the orientation of a given external magnetic field and that we would like to estimate its amplitude. To do so, we let the atomic spins precess in the magnetic field for a given time (this is a unitary evolution of the quantum system). This process is well known as Larmor precession: the precession frequency of the atomic spins is proportional to the magnetic field amplitude, with known proportionality constant $g\mu_{\mathrm{B}}$, where g is the Landé g factor and μ_{B} is the Bohr magneton. Thus, for a given precession time, the resulting state, i.e., the orientation of the spins, depends on the magnetic field amplitude. Under realistic conditions, the interactions between atoms or interactions of the atoms with the walls of the vapor cell contribute to the dynamics. Such processes are summarized as *decoherence* processes or, in case of energy exchange with an environment (such as the walls), as *dissipative* processes. However, even such complicated processes can be taken into account (for instance, by numerically solving the corresponding master equations) and one obtains an effective dynamics for each atomic spin [4].

In step (iii), the state $\rho(\boldsymbol{\theta})$ is measured. This is when information is transferred from the quantum system to a classical processing unit for post processing the measurement outcomes. The physical processes involved during the measurement process may be very complicated. Nevertheless, quantum metrology provides a concise framework to characterize the relevant properties of the measurement process: with the help of a so-called positive operator-valued measure (POVM) we can calculate the expected probabilities for a measurement outcome for a given state $\rho(\boldsymbol{\theta})$ [32, 46]. A POVM consists of N positive semidefinite operators $\{\Pi_j\}_{j=1}^{N}$, $\Pi_j \geq 0$, which satisfy $\sum_{j=1}^{N} \Pi_j = \mathbb{1}$ and correspond to N different measurement outcomes (a generalization to a continuous range of measurement outcomes is possible). Then, the probability p_x of obtaining the xth measurement outcome is obtained according to the Born rule, $p_x = \mathrm{tr}\left[\Pi_x \rho(\boldsymbol{\theta})\right]$. POVMs represent the most general way to characterize measurements and include the well-known von Neumann measurement as a special case. Also weak and continuous measurements can be described based on POVMs [37].

Returning once again to our example of magnetic field estimation with polarized atoms, one way to measure the spin state relies on the Faraday effect. Shooting with a linearly polarized laser beam at the polarized atoms, the polarization of the laser pulse is rotated depending on the polarization of the atoms. Then, information about the magnetic field amplitude is encoded in the polarization of the transmitted laser

pulse, which, in turn, can be measured easily using a polarization beam splitter and photodetectors, see Figure 1.2.

Step (iv) consists of the post processing the collected data in order to estimate $\boldsymbol{\theta}$. From a mathematical perspective, this is a problem of statistical inference [33]. We can distinguish two important approaches to statistical inference: the frequentist and the Bayesian one, which both will be discussed in the following.

1.1 The Frequentist Approach to Quantum Parameter Estimation

In the frequentist approach, we collect data, i.e., measurement outcomes, typically by repeating the experiment [steps (i) to (iii)] many times or by at least performing experiments in a predefined way (collecting all the measurement outcomes). Then, we estimate $\boldsymbol{\theta}$ using an estimator function. Intuitively, we would like to pick an estimate $\hat{\boldsymbol{\theta}}$ which is most likely given by the observed measurement outcomes. This notion can be formulated mathematically and is well known as maximum likelihood estimation (MLE) [33]. MLE provides us with a strong estimate and as a figure of merit for the goodness of the estimation we typically consider the variance of the estimator $\hat{\boldsymbol{\theta}}_{\mathrm{MLE}}$.

For the sake of simplicity, let us assume for the moment that we repeat an experiment M times. Then, the problem of experiment design, i.e., how to design steps (i) to (iii), is reduced to how to design one experiment (that is repeated M times). This problem can be tackled *a priori*, i.e., before the measurements are performed. Clearly, a solution of this problem will generally depend on many factors such as properties of the estimator function of our choice, the number of repetitions M, our prior knowledge about $\boldsymbol{\theta}$, and even the true value of $\boldsymbol{\theta}$.

While the general problem of experiment design is very challenging, there exists a very powerful framework which deals with an interesting limiting case, and experiments are often designed according to this framework even if the conditions, which we will shortly introduce, are not exactly fulfilled. It is about the framework of quantum Cramér–Rao bound and quantum Fisher information which represents an extension of the corresponding classical framework well known in estimation theory. Let D be the collected data, i.e., the measurement outcomes $\{x_j\}_{j=1}^M$ from M measurements. The Cramér–Rao bound holds for unbiased estimators. An estimator is unbiased if $\mathrm{E}_{D|\boldsymbol{\theta}}(\hat{\boldsymbol{\theta}}) = \boldsymbol{\theta}$ for all $\boldsymbol{\theta}$, where $\mathrm{E}_{D|\boldsymbol{\theta}}$ is the expectation value with respect to all possible data D for a given $\boldsymbol{\theta}$. This means that the estimator returns on average (with respect to all possible data) the true value $\boldsymbol{\theta}$. The Cramér–Rao bound is a special case of the Cramér–Rao inequality which considers not just the estimation of $\boldsymbol{\theta}$ but more generally the estimation of a function $g(\boldsymbol{\theta})$. For the sake of simplicity, we limit ourselves here to the case where we directly estimate a single parameter θ.

Further, as a figure of merit for the goodness of an estimator $\hat{\theta}$, we will consider its

variance,

$$\mathrm{Var}_{D|\theta}(\hat{\theta}) = \mathrm{E}_{D|\theta}\left[\left(\hat{\theta} - \mathrm{E}_{D|\theta}\left[\hat{\theta}\right]\right)^2\right]. \tag{1.1}$$

A smaller variance corresponds to a more trustworthy, a more precise estimate. Then, provided that some technical regularity conditions hold, the Cramér–Rao bound provides a lower bound for the variance of the estimator,

$$\mathrm{Var}_{D|\theta}(\hat{\theta}) \geq \frac{1}{MI_{\mathrm{Fisher}}(\theta)}, \tag{1.2}$$

where $I_{\mathrm{Fisher}}(\theta)$ denotes the Fisher information, which is defined as

$$I_{\mathrm{Fisher}}(\theta) = \mathrm{E}_{D|\theta}\left[\left(\frac{\partial}{\partial\theta}\ln[p(D|\theta)]\right)^2\right], \tag{1.3}$$

and $p(D|\theta)$ is the probability of obtaining measurement outcomes $D = \{x_j\}_{j=1}^{M}$ given that the parameter is θ. $p(D|\theta)$ can be calculated with the Born rule and reads

$$p(D|\theta) = \prod_{j=1}^{M} \mathrm{tr}\left[\Pi_{x_j}\rho_j(\theta)\right], \tag{1.4}$$

where Π_{x_j} is the POVM element corresponding to the outcome x_j of the jth measurement of $\rho_j(\theta)$, the resulting state of the jth experiment. This shows that $p(D|\theta)$ and, thus, the Fisher information depend not only on the true value of θ but also via Π_{x_j} and $\rho_j(\theta)$ on steps (i) to (iii), i.e., on the experiment design. Therefore, a possible policy for experiment design would be to design experiments which maximize the Fisher information (and thus minimize the lower bound (1.2) on the variance of the estimator). The only problem is that minimizing a lower bound [see the inequality (1.2)] does not guarantee that the variance is minimized as well.

However, in case of single-parameter estimation, the Cramér–Rao bound exhibits a very remarkable property. In the limit of many measurements, $M \to \infty$, the Cramér–Rao bound (1.2) becomes tight [23]. Note that this does not hold for multi-parameter estimation in general. The convergence of $\mathrm{Var}(\hat{\theta})$ to the lower bound (1.2) was tested numerically for various examples and it was found that the number of measurements needed to reach the threshold depends on the initial state [9, 52]; often, $M \gtrsim 100$ measurement are enough, but for some non-classical states $M \gtrsim 10^3$ measurements are required. Nevertheless, the Fisher information is an important and convenient figure of merit for experiment design.

Maximizing the Fisher information by optimizing with respect to different aspects of the experiment design is an important branch of quantum metrology. The optimization with respect to possible measurements [step (iii)] is particularly straightforward from a theoretical point of view. Using the Cauchy–Schwarz inequality, we can maximize the Fisher information in full generality with respect to the set of all possible POVMs.

This yields another lower bound on the variance of the estimator which no longer depends on the POVM: The *quantum* Cramér–Rao bound (QCRB) reads

$$\mathrm{Var}_{D|\theta}(\hat{\theta}) \geq \frac{1}{MI(\theta)}. \tag{1.5}$$

$I(\theta)$ is the so-called *quantum* Fisher information (QFI) which is defined as

$$I(\theta) = \mathrm{tr}\left[L^2_{\rho(\theta)}\rho(\theta)\right], \tag{1.6}$$

where we used the symmetric logarithmic derivative $L_{\rho(\theta)}$ which is defined implicitly via $\partial_\theta\rho(\theta) = (L_{\rho(\theta)}\rho(\theta) + \rho(\theta)L_{\rho(\theta)})/2$. Explicit expressions for the QFI can be obtained by expanding $\rho(\theta)$ with respect to a basis.

Being independent of the POVM, the QFI is often more convenient for analytic calculations than the Fisher information. In particular, given a certain parameter estimation problem and a model for steps (i) and (ii), the scaling with important resources such as the number of probes (atoms, photons) or the consumed time can be established with the help of the QFI.

In terms of resources, time is special if it is possible to arbitrarily change the time for an experiment (we assume here that preparation and measurement are instantaneous compared to the dynamics, and that there is no waiting time between the repetitions of experiments). For example, instead of one experiment we can do two experiments with half of the time. This leads to a tradeoff between time and the number of measurements (the latter enters as $1/M$ in the QCRB). This tradeoff can be taken into account by considering a rescaled QFI instead, $I(\theta)/t$, where t is the total time of all experiments. With the help of the rescaled QFI it is then possible to compare different estimation strategies which consume different amounts of time [16, 17].

Also note that the QCRB framework is useful in the context of the frequentist approach but is not limited to it. More importantly, the QCRB framework falls into the category of *local* parameter estimation: the QCRB generally depends on the true value of the parameter θ. Further, if experiments are designed according to the QCRB framework, we usually need to know θ and the experiments might be suboptimal for other values of the parameter. Thus, it is a local optimization of experiment design tailored to a particular value of θ. In practice this does not pose a problem. For example, the parameter θ can be often estimated in a "warming-up phase" consuming a small fraction of the available resources [9, 52]. Then, when we already have a good estimate of θ at hand, we can apply the QCRB framework in order to find (close to) optimal experiment designs with the remaining resources. Independent of such practical considerations, the QCRB is very useful as an ultimate lower bound on the achievable measurement precision.

An important discovery was that quantum metrology, in principle, allows for the so-called Heisenberg scaling of the QFI [22, 34, 65]. Heisenberg scaling means $I(\theta) \propto N^2$ where N is the number of probes. In our example of magnetic field estimation with

polarized atoms, N would be the number of atoms. Heisenberg scaling of the QFI corresponds to a standard deviation $\sqrt{\mathrm{Var}(\hat{\theta})}$ that scales as N^{-1} (when the QCRB is saturated). Classically, we would expect that N probes allow us in principle to perform N experiments, each consuming one probe. Then, the central limit theorem dictates only a $N^{-1/2}$ scaling of the standard deviation. This discrepancy between classical and quantum limits is an ongoing driving force for research in quantum metrology [7, 51]. Roughly speaking, the quantum supremacy results from non-classical correlations which can be established in quantum states but are classically impossible. For example, a non-classical state of atomic spins could be obtained by introducing entanglement between the atoms [59]. Doing this in the right way, i.e., by maximizing the QFI, Heisenberg scaling is in principle possible (ignoring decoherence).

In practice, there are several obstacles on the path towards Heisenberg scaling. While some of these obstacles depend on the actual system under consideration, the following points apply to many cases. First of all, due to various sources of noise, it is often difficult to merely reach the standard quantum limit ($\sqrt{\mathrm{Var}(\hat{\theta})} \propto N^{-1/2}$) which should be achievable *without* "quantum resources" such as entanglement. Once this problem is solved, preparing non-classical states and protecting them against decoherence is a challenge. In particular the creation of non-classical correlations over a large number of probes is often very difficult but necessary in order to outperform quantum sensors which use classical states with many probes. Finally, theoretical results show that in the presence of decoherence, Heisenberg scaling is often lost completely. Concerning the last point, it is important to note that this does not mean that quantum enhancements are not possible. It is still possible to increase the QFI with quantum enhancements (increasing the "prefactor" instead of the "scaling")[13].

1.2 The Bayesian Approach to Quantum Parameter Estimation

In the Bayesian framework, data collection (the acquisition of measurement outcomes) is seen as a process spread over time. The idea is to update our knowledge (or "beliefs", as it is often called in the context of Bayesian inference) about $\boldsymbol{\theta}$ every time we obtain new measurement outcomes. Let $D_k = \{x_j\}_{j=1}^{k}$ be the collected measurement outcomes up to the kth experiment. To begin with, this requires that we write down our initial knowledge about $\boldsymbol{\theta}$. For example, imagine the only prior knowledge about $\boldsymbol{\theta}$ is that $\boldsymbol{\theta}$ is restricted to some domain Θ. For the sake of simplicity, let us assume that each θ_j is restricted to an interval. Then, we represent our prior knowledge by a probability distribution $p(\boldsymbol{\theta})$ on Θ which is constant, a so-called uniform prior. Once we obtain the first measurement outcome x_1, we update our knowledge, i.e., $p(\boldsymbol{\theta})$ to $p(\boldsymbol{\theta}|D_1)$, where $p(\boldsymbol{\theta}|D_k)$ denotes the probability distribution on Θ which represents our knowledge about $\boldsymbol{\theta}$ after the kth experiment, and $p(\boldsymbol{\theta}|D_0) = p(\boldsymbol{\theta})$. The update is given by Bayes

law [33, 28],

$$p(\boldsymbol{\theta}|D_k) = \frac{p(x_k|\boldsymbol{\theta})p(\boldsymbol{\theta}|D_{k-1})}{p(x_k)}, \tag{1.7}$$

where $p(\boldsymbol{\theta}|D_k)$ is our updated knowledge (posterior), $p(\boldsymbol{\theta}|D_{k-1})$ is our prior knowledge (prior), and $p(x_k)$ is a normalization, $p(x_k) = \mathrm{E}_{\boldsymbol{\theta}}\left[p(x_k|\boldsymbol{\theta})\right]$. Given a model for the experiment [according to steps (i) to (iii)], $p(x_k|\boldsymbol{\theta})$ can be calculated with the Born rule. Using Bayes law, we are in principle able to take into account every new measurement outcome increasing our knowledge about $\boldsymbol{\theta}$ step by step if the measurements are informative.

Compared to the frequentist approach which relies on post processing the data after all measurement are done, the Bayesian one requires data processing (calculating the Bayes update) between the measurements. On the other hand, we do not have to store the measurement outcomes in the Bayesian approach; the only object we need to store after j experiments is $p(\boldsymbol{\theta}|D_j)$, i.e., our current knowledge about $\boldsymbol{\theta}$.

When it comes to estimating $\boldsymbol{\theta}$, the expected value of $\boldsymbol{\theta}$ over $p(\boldsymbol{\theta}|D_j)$,

$$\hat{\boldsymbol{\theta}}_j = \mathrm{E}_{\boldsymbol{\theta}|D_j}\left(\boldsymbol{\theta}\right), \tag{1.8}$$

immediately suggests itself for estimating $\boldsymbol{\theta}$. The index j for the estimator is necessary because the estimator corresponds to the estimation after j experiments.

In the context of Bayesian inference, one usually defines a figure of merit for the estimator $\hat{\boldsymbol{\theta}}_j$ by starting with a loss function. Let us consider the quadratic loss

$$L(\hat{\boldsymbol{\theta}}_j|\boldsymbol{\theta}) = \left|\left|\hat{\boldsymbol{\theta}}_j - \boldsymbol{\theta}\right|\right|^2 \tag{1.9}$$

as a loss function, where $||\bullet||^2$ denotes the L2-norm. The risk of the estimator is then given by

$$R(\hat{\boldsymbol{\theta}}_j) = \mathrm{E}_{D|\boldsymbol{\theta}}\left[\left|\left|\hat{\boldsymbol{\theta}}_j - \boldsymbol{\theta}\right|\right|^2\right], \tag{1.10}$$

and the Bayes risk is obtained by averaging the risk with respect to parameters,

$$r\left[\hat{\boldsymbol{\theta}}_j, p(\boldsymbol{\theta})\right] = \mathrm{E}_{\boldsymbol{\theta}}\left[R(\hat{\boldsymbol{\theta}}_j)\right]. \tag{1.11}$$

This defines the Bayes risk r of the estimator $\hat{\boldsymbol{\theta}}_j$ with respect to some prior $p(\boldsymbol{\theta})$. In the Bayesian setting, we aim to minimize the Bayes risk, i.e., we try to design experiments accordingly.

The optimization of adaptive experiment design is usually analytically intractable and numerically too expensive (in terms of run time) for practical applications. Only in a few idealized simple cases, solutions for adaptive experiment designs are known [12, 15]. In practice, one has to rely on heuristics for experiment design. These

heuristics are rather simple rules which are fast to compute and usually motivated by analytic insights from simplified models.

Chapter 2

Summary

A precise formulation of the results and the methods used to obtain them can be found in the publications [16–18, 55, 19]. Further, a quantum-chaotic cesium-vapor magnetometer is subject of a published patent publication [8]. In this chapter, the results of the publications will be summarized.

2.1 Dynamics of Quantum Sensors: Quantum Chaos and Reinforcement Learning

Publication [16] and a corresponding conference proceedings [17] deal with so-called quantum-chaotic sensors. The idea is to improve the dynamics of quantum sensors by rendering the dynamics quantum-chaotic. At the same time we avoid obstacles regarding the preparation of non-classical initial states by using classical initial states which are easy to prepare.

The motivation for improving the (usually integrable) dynamics of quantum sensors by rendering the dynamics quantum-chaotic, deserves an explanation: First of all, quantum chaos is not chaotic in the classical sense [30]. In particular, the unpredictability, which is characteristic for chaos and would be detrimental for quantum sensors, is not present in quantum chaos. Instead, quantum chaos is concerned with dynamical quantum systems which become chaotic in the classical limit. Furthermore, there
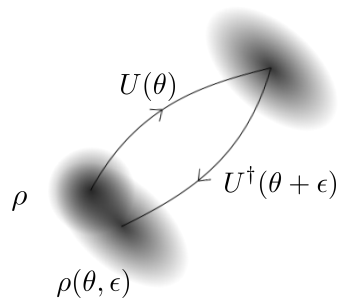

Figure 2.1 Schematic illustration of the Loschmidt echo, which is defined as the fidelity between the states ρ and $\rho(\theta, \epsilon)$.

is a well-known fundamental relation between two quantities: the quantum Fisher information (QFI) and the Loschmidt echo [26, 42, 10]. While we introduced the QFI in Chapter 1 as important figure of merit of quantum metrology, the Loschmidt echo is an important quantity in quantum chaos where it is used to study the sensitivity to changes of the dynamics of quantum chaotic systems.

As discussed in Chapter 1, the QFI for single-parameter estimation depends on a parameter-dependent state $\rho(\theta)$. Let us assume that $\rho(\theta)$ is the result of a unitary dynamics $U(\theta)$ [step (ii)] which is applied to an initial state ρ [step (i)]. The Loschmidt echo for ρ and $U(\theta)$ is defined as the fidelity between ρ and $\rho(\theta, \epsilon) = U^\dagger(\theta + \epsilon)U(\theta)\rho[U^\dagger(\theta + \epsilon)U(\theta)]^\dagger$, i.e., the same state propagated forward with $U(\theta)$ and propagated backward with $U^\dagger(\theta + \epsilon)$. The fidelity for two states ρ and σ is given by $||\sqrt{\rho}\sqrt{\sigma}||_{\text{tr}}^2$, with the trace norm $||A||_{\text{tr}} = \text{tr}\left(\sqrt{A^\dagger A}\right)$ [44]. Hence, the Loschmidt echo for a state ρ and dynamics U_θ with perturbation ϵ in the parameter θ is defined by [26, 39]

$$F(\theta, \epsilon) = ||\sqrt{\rho}\sqrt{\rho(\theta, \epsilon)}||_{\text{tr}}^2. \tag{2.1}$$

By rewriting the QFI with the Bures distance (see publication [16]) and expressing the Bures distance with the fidelity, we obtain for the QFI $I(\theta)$ [10],

$$I(\theta) = \lim_{\epsilon \to 0} 4 \frac{1 - F(\theta, \epsilon)}{\epsilon^2}. \tag{2.2}$$

From Eq. (2.2) it is clear that the QFI is directly related to the Loschmidt echo in the limit of small ϵ, i.e., small perturbations of the parameter θ. This limiting case of small ϵ is referred to as the perturbative regime of the Loschmidt echo, and linear response expressions for the Loschmidt echo correspond to exact expressions for the quantum Fisher information. The insight that this regime of quantum chaos has favorable metrological properties represents the main motivation for this work.

Now, that we have recapitulated the motivation, let us summarize the results. The latter are all based on the kicked top model [31] (see also Eq. (1) in publication [16] or Eq. (3) in publication [55]) in its pure form with unitary dynamics, in combination with decoherence models such as superradiant damping and phase damping, or by simulating experiments which implement the kicked top model. The results include:

(i) Results for the linear response regime of the Loschmidt echo are transferred to the QFI in order to understand and characterize the behavior of the QFI in the fully chaotic regime. In particular, we identify different time regimes separated by the Ehrenfest and Heisenberg times.

(ii) Different dynamical regimes such as mixed phase spaces and the different regions in mixed phase spaces (islands of stability, chaotic sea, and the border between them) are explored numerically by calculating the QFI for spin-coherent initial states centered around points in phase space corresponding to respective regions.

The QFI proves to be a good signature of chaos in the sense that it is generally larger for chaotic phase space regions than for those with regular dynamics.

(iii) We demonstrate that quantum chaos is able to fight the detrimental effects of decoherence at the example of superradiant damping. In particular, we find that the non-linear kicks (being part of the kicked top model), are particularly well-suited to fight the dissipative effects of superradiant damping: a further numerical optimization of the timing of the kicks reveals a new dynamical control strategy (see publication [55]). The numerical optimization relies on reinforcement learning where we use the QFI as a reward function. The control strategy discovered with reinforcement learning brings us away from quantum chaos but leads to a kind of adaptive spin squeezing (as can be seen by plotting the Wigner function of the state). The spin squeezing is renewed during the dynamics when otherwise the superradiant damping would destroy the squeezed state quickly. While even this optimized strategy is not able to fully defeat decoherence, it nevertheless makes the QFI increase for a much longer time than it would be the case without the non-linear kicks.

(iv) The robustness against fluctuations in the strength of the control pulses (non-linear kicks) is verified numerically.

(v) A quantum-chaotic cesium-vapor magnetometer is proposed and part of a patent application (published patent application [8]). The conference proceedings [17] focuses on the details. The idea is to add non-linear kicks to a standard spin-precession magnetometer (as described in Chapter 1). The magnetometer operates in the spin-exchange relaxation-free regime, and the kicks are implemented optically with a linearly polarized, off-resonant laser beam exploiting the AC-Stark effect. The numerical simulation takes into account all relevant decoherence effects (spin-exchange and spin-destruction relaxation), imperfect state preparation by describing the state as a spin-temperature distribution, Doppler broadening (the sensor operates at room temperature), a finite length of the kicks (in contrast to the infinitesimal short kicks of the kicked top model), and jump processes induced by the optical implementation of the kicks.

2.2 Maximal Quantum Fisher Information for Mixed States

Publication [18] provides analytic results concerning the maximal quantum Fisher information for mixed states. We assume unitary sensor dynamics [for step (ii), as described in Chapter 1] and unitary state preparation [step (i)] from a given (generally mixed) state. If pure states are available, then the maximal QFI and the corresponding optimal state preparation are well known for any unitary sensor dynamics [23, 6]. In this work, we extend this general result to the case when only mixed states are available

- this is typically the case in experiments due to imperfect state preparation. Note that the initial purity (or more precisely, the spectrum) of an available mixed state remains invariant because state preparation and dynamics are assumed to be unitary. We provide the maximum QFI and the corresponding optimal state preparation for *any* available mixed state and *any* unitary sensor dynamics. These results allow us to give tighter bounds on the measurement precision if only mixed states are available. Further, optimal states for quantum metrology are of high interest also in other theoretical branches of quantum information such as the characterization of quantumness [47, 24] or in the context of resource theories [58]. This result proves a conjecture by Modi, Vedral et al. [45].

Publication [18] also provides for the same unitary model an analytic solution for the maximal QFI when we optimize with respect to both, the initial state and the dynamical control. The dynamical control is given by an additional control Hamiltonian such that the dynamics is the unitary transformation which corresponds to the original (parameter-dependent) Hamiltonian plus the control Hamiltonian. The optimal solution holds again in full generality, i.e., for any available mixed state and for any (parameter-dependent) Hamiltonian of the dynamics. Previously, only the case for pure initial states was known [50]. The concept of Hamiltonian control during the dynamics can be seen as a possibility to keep the state in the most sensitive state for any time. In experiments, Hamiltonian control will typically accomplish the task of compensating unwanted interactions between probes and guiding the state such that it is always most sensitive [20, 50]. As regards theoretical perspectives, it would be an important improvement to further generalize our results to non-unitary dynamics.

The kicked top model used in the previously discussed publications can actually be seen as well in the context of Hamiltonian control: the precession corresponds to the parameter-dependent dynamics and the kicks are control pulses applied to the dynamics. However, while the bounds that we found in publication [18] are valid, they are not tight and the optimal Hamiltonian control does not apply because we do not study the kicked top model with optimal initial states. The bounds can be saturated only if both, the initial state and the Hamiltonian control, are optimized.

2.3   Neural-Network Heuristics for Adaptive Bayesian Quantum Estimation

Finally, in publication [18], we demonstrate the usefulness of the new bounds for mixed states by considering the case that thermal states are available and that the dynamics is given by a phase-shift (precession) Hamiltonian (along the lines of the magnetometer discussed in Chapter 1). We find that using the optimal unitary state preparation Heisenberg scaling can be reached even with thermal states. A proof is given for Heisenberg scaling with respect to the size of the individual probes as well as the number of probes. The Heisenberg scaling prevails for any finite temperature (of the thermal state); the QFI is damped with increasing temperatures only polynomially.

The last manuscript [19] included in this thesis deals with adaptive Bayesian quantum estimation (for an introduction see Chapter 1). Building on a powerful framework for numerically approximating the Bayesian update [40, 36, 29, 27] based on particle filtering and the sequential Monte-Carlo method, we provide a versatile numerical solution for generating fast and strong experiment-design heuristics (EDHs). The motivation is to find a general receipt for creating EDHs. So far, heuristics have been found manually with the help of analytic arguments derived under idealized conditions. This approach is cumbersome because what distinguishes a good heuristic depends on the estimation problem and the available resources. Our approach can instead utilize such analytical insights but does not have to rely on them. Further, it promises EDHs which are tailored to the specific constraints of the estimation problem and the available resources. Our method is based on a combination of supervised and reinforcement learning. Supervised learning is used to train a neural network to imitate the behavior of an already existing heuristic. This is also known as behavior cloning or imitation learning. In a second step we use reinforcement learning to further improve the heuristic. One advantage of reinforcement learning is that there is no teacher, no other heuristic, which the neural network is supposed to imitate. This means, that the success of reinforcement learning is not limited by our "expert" knowledge and the performance of the heuristics can surpass any previously known heuristic. We also show that the first step of imitation learning is useful if strong heuristics are already known but not necessary: we provide a receipt for creating heuristics using only reinforcement learning.

We demonstrate our neural network approach to experiment design at the to date best explored (in the context of adaptive Bayesian quantum estimation) example of frequency estimation with a qubit, e.g., estimating a magnetic field with a spin-1/2 particle [14, 64, 63, 53, 61, 49, 43]. The experiment design consists of choosing the precession time. The model is studied with and without decoherence (T_2 relaxation). For this model, several strong heuristics are known such that reliable benchmarks are available. We find that the neural-network heuristics surpass the performance of the best known heuristics. In addition, for a two-parameter estimation problem (frequency and relaxation rate), the neural-network heuristics outperform all other benchmark heuristics.

Our approach to experiment design works well together with the numerical framework for Bayesian updates. This framework also allows for a simple computation of confidence regions [5, 28]. We use this tool for visualizing the performance of different experiment-design heuristics. The success of the joint framework of Bayesian update and experiment design in practice depends in many cases on the run time. Long run times will easily ruin the overall performance of the sensor because time is usually a limited resource if not even the most important resource. The run time (for one call) of our neural networks is comparable with one numerical Bayesian update (single core computation). As a matter of fact, the practical success of the numerical framework depends on the properties of the sensor such as insensitive intervals [53],

transmission times of data, the implementation of the numerical framework (e.g., on a field-programmable gate array [48]) and, of course, on the estimation problem under consideration.

As regards theoretical perspectives, the training of neural networks for experiment design could be made more efficient in terms of run time, for instance, by using other reinforcement learning algorithms. Furthermore, the run time of the neural networks could be reduced by using smaller neural networks. Alternatively, the number of calls could be reduced, i.e., the neural-network heuristic is would not be called after every experiment but, for instance, only after every nth experiment. Then, the neural-network heuristic would have to choose experiment designs for the next n experiments. Hence, the total run time of the heuristic would be reduced at the cost of adaptivity after each experiment.

In conclusion, this thesis deals with various topics related to quantum metrology. Full-fledged machine learning techniques are used to tackle problems of dynamical control and experiment design. The results are relevant for both theory and experiment. We are confident that future experimental work will demonstrate the feasibility of quantum-chaotic sensors and the usefulness of neural-network heuristics for adaptive Bayesian quantum estimation.

Bibliography

[1] Aasi, J., Abadie, J., Abbott, B., Abbott, R., Abbott, T., Abernathy, M., Adams, C., Adams, T., Addesso, P., Adhikari, R., et al. (2013). Enhanced sensitivity of the LIGO gravitational wave detector by using squeezed states of light. *Nature Photonics*, 7(8):613.

[2] Allen, E. H. and Karageorgis, M. (2008). Radar systems and methods using entangled quantum particles. US Patent 7,375,802.

[3] Allred, J. C., Lyman, R. N., Kornack, T. W., and Romalis, M. V. (2002). High-Sensitivity Atomic Magnetometer Unaffected by Spin-Exchange Relaxation. *Phys. Rev. Lett.*, 89(13):130801.

[4] Appelt, S., Baranga, A. B.-A., Erickson, C. J., Romalis, M. V., Young, A. R., and Happer, W. (1998). Theory of spin-exchange optical pumping of ^{3}He and ^{129}Xe. *Phys. Rev. A*, 58:1412–1439.

[5] Blume-Kohout, R. (2010). Optimal, reliable estimation of quantum states. *New Journal of Physics*, 12(4):043034.

[6] Boixo, S., Flammia, S. T., Caves, C. M., and Geremia, J. (2007). Generalized Limits for Single-Parameter Quantum Estimation. *Phys. Rev. Lett.*, 98(9):090401.

[7] Braun, D., Adesso, G., Benatti, F., Floreanini, R., Marzolino, U., Mitchell, M. W., and Pirandola, S. (2018). Quantum-enhanced measurements without entanglement. *Rev. Mod. Phys.*, 90:035006.

[8] Braun, D. and Fiderer, L. J. (2018). Quantenchaotischer Magnetfeldsensor. *(Published Patent Application)*, (DE 10 2018 000 118 A1).

[9] Braunstein, S. L. (1992). Quantum limits on precision measurements of phase. *Phys. Rev. Lett.*, 69(25):3598–3601.

[10] Braunstein, S. L. and Caves, C. M. (1994). Statistical distance and the geometry of quantum states. *Phys. Rev. Lett.*, 72(22):3439–3443.

[11] Budker, D. and Romalis, M. (2007). Optical magnetometry. *Nature physics*, 3(4):227.

[12] Childs, A. M., Preskill, J., and Renes, J. (2000). Quantum information and precision measurement. *Journal of Modern Optics*, 47(2-3):155–176.

[13] Escher, B., de Matos Filho, R., and Davidovich, L. (2011). General framework for estimating the ultimate precision limit in noisy quantum-enhanced metrology. *Nature Physics*, 7(5):406.

[14] Ferrie, C., Granade, C. E., and Cory, D. G. (2012a). Adaptive Hamiltonian estimation using Bayesian experimental design. *AIP Conference Proceedings*, 1443(1):165–173.

[15] Ferrie, C., Granade, C. E., and Cory, D. G. (2012b). How to best sample a periodic probability distribution, or on the accuracy of Hamiltonian finding strategies. *Quantum Information Processing*, 12(1):611–623.

[16] Fiderer, L. J. and Braun, D. (2018). Quantum metrology with quantum-chaotic sensors. *Nature Communications*, 9(1):1351.

[17] Fiderer, L. J. and Braun, D. (2019). A quantum-chaotic cesium-vapor magnetometer. In Shahriar, S. M. and Scheuer, J., editors, *Optical, Opto-Atomic, and Entanglement-Enhanced Precision Metrology*, volume 10934, page 109342S. SPIE.

[18] Fiderer, L. J., Fraïsse, J. M. E., and Braun, D. (2019). Maximal Quantum Fisher Information for Mixed States. *Phys. Rev. Lett.*, 123:250502.

[19] Fiderer, L. J., Schuff, J., and Braun, D. (2020). Neural-Network Heuristics for Adaptive Bayesian Quantum Estimation. *arXiv preprint arXiv:2003.02183*.

[20] Fraïsse, J. M. E. and Braun, D. (2017). Enhancing sensitivity in quantum metrology by Hamiltonian extensions. *Phys. Rev. A*, 95:062342.

[21] Giovannetti, V., Lloyd, S., and Maccone, L. (2001). Quantum-enhanced positioning and clock synchronization. *Nature*, 412(6845):417–419.

[22] Giovannetti, V., Lloyd, S., and Maccone, L. (2004). Quantum-Enhanced Measurements: Beating the Standard Quantum Limit. *Science*, 306(5700):1330–1336.

[23] Giovannetti, V., Lloyd, S., and Maccone, L. (2006). Quantum Metrology. *Phys. Rev. Lett.*, 96(1):010401.

[24] Giraud, O., Braun, P., and Braun, D. (2010). Quantifying quantumness and the quest for Queens of Quantum. *New Journal of Physics*, 12(6):063005.

[25] Goda, K., Miyakawa, O., Mikhailov, E. E., Saraf, S., Adhikari, R., McKenzie, K., Ward, R., Vass, S., Weinstein, A. J., and Mavalvala, N. (2008). A quantum-enhanced prototype gravitational-wave detector. *Nature Physics*, 4(6):472–476.

[26] Gorin, T., Prosen, T., Seligman, T. H., and Žnidarič, M. (2006). Dynamics of Loschmidt echoes and fidelity decay. *Physics Reports*, 435(2-5):33–156.

[27] Granade, C., Ferrie, C., Casagrande, S., Hincks, I., Kononenko, M., Alexander, T., and Sanders, Y. (2016). QInfer: Library for Statistical Inference in Quantum Information.

[28] Granade, C., Ferrie, C., Hincks, I., Casagrande, S., Alexander, T., Gross, J., Kononenko, M., and Sanders, Y. (2017). QInfer: Statistical inference software for quantum applications. *Quantum*, 1:5.

[29] Granade, C. E., Ferrie, C., Wiebe, N., and Cory, D. G. (2012). Robust online Hamiltonian learning. *New Journal of Physics*, 14(10):103013.

[30] Haake, F. (2001). *Quantum Signatures of Chaos*. Springer Berlin Heidelberg.

[31] Haake, F., Kuś, M., and Scharf, R. (1987). Classical and quantum chaos for a kicked top. *Zeitschrift für Physik B Condensed Matter*, 65(3):381–395.

[32] Helstrom, C. W. (1976). *Quantum Detection and Estimation Theory*. Elsevier.

[33] Hogg, R. V., Tanis, E. A., and Zimmerman, D. L. (1977). *Probability and statistical inference*, volume 993. Macmillan New York.

[34] Holland, M. J. and Burnett, K. (1993). Interferometric detection of optical phase shifts at the Heisenberg limit. *Phys. Rev. Lett.*, 71:1355–1358.

[35] Huelga, S. F., Macchiavello, C., Pellizzari, T., Ekert, A. K., Plenio, M. B., and Cirac, J. I. (1997). Improvement of Frequency Standards with Quantum Entanglement. *Phys. Rev. Lett.*, 79(20):3865–3868.

[36] Huszár, F. and Houlsby, N. M. T. (2012). Adaptive Bayesian quantum tomography. *Phys. Rev. A*, 85:052120.

[37] Jacobs, K. and Steck, D. A. (2006). A straightforward introduction to continuous quantum measurement. *Contemporary Physics*, 47(5):279–303.

[38] Leibfried, D. (2004). Toward Heisenberg-Limited Spectroscopy with Multiparticle Entangled States. *Science*, 304(5676):1476–1478.

[39] Liu, J., Jing, X.-X., Zhong, W., and Wang, X. (2014a). Quantum Fisher information for density matrices with arbitrary ranks. *Communications in Theoretical Physics*, 61(1):45–50. arXiv preprint arXiv:1312.6910.

[40] Liu, J. and West, M. (2001). Combined Parameter and State Estimation in Simulation-Based Filtering. In *Sequential Monte Carlo Methods in Phys. Rev. Actice*, pages 197–223. Springer New York.

[41] Liu, J., Xiong, H.-N., Song, F., and Wang, X. (2014b). Fidelity susceptibility and quantum Fisher information for density operators with arbitrary ranks. *Physica A: Statistical Mechanics and its Applications*, 410:167–173.

[42] Liu, J., Xiong, H.-N., Song, F., and Wang, X. (2014c). Fidelity susceptibility and quantum Fisher information for density operators with arbitrary ranks. *Physica A: Statistical Mechanics and its Applications*, 410:167–173.

[43] Lumino, A., Polino, E., Rab, A. S., Milani, G., Spagnolo, N., Wiebe, N., and Sciarrino, F. (2018). Experimental Phase Estimation Enhanced by Machine Learning. *Phys. Rev. Applied*, 10(4):044033.

[44] Miszczak, J. A., Puchała, Z., Horodecki, P., Uhlmann, A., and Życzkowski, K. (2008). Sub– and super–fidelity as bounds for quantum fidelity. *arXiv preprint arXiv:0805.2037*.

[45] Modi, K., Cable, H., Williamson, M., and Vedral, V. (2011). Quantum Correlations in Mixed-State Metrology. *Phys. Rev. X*, 1:021022.

[46] Nielsen, M. A. and Chuang, I. (2002). *Quantum computation and quantum information*. AAPT.

[47] Ollivier, H. and Zurek, W. H. (2001). Quantum Discord: A Measure of the Quantumness of Correlations. *Phys. Rev. Lett.*, 88:017901.

[48] Omondi, A. R. and Rajapakse, J. C. (2006). *FPGA implementations of neural networks*, volume 365. Springer.

[49] Paesani, S., Gentile, A., Santagati, R., Wang, J., Wiebe, N., Tew, D., O'Brien, J., and Thompson, M. (2017). Experimental Bayesian Quantum Phase Estimation on a Silicon Photonic Chip. *Phys. Rev. Lett.*, 118(10):100503.

[50] Pang, S. and Jordan, A. N. (2017). Optimal adaptive control for quantum metrology with time-dependent Hamiltonians. *Nature Communications*, 8:14695.

[51] Pezzè, L., Smerzi, A., Oberthaler, M. K., Schmied, R., and Treutlein, P. (2018). Quantum metrology with nonclassical states of atomic ensembles. *Rev. Mod. Phys.*, 90:035005.

[52] Rubio, J., Knott, P., and Dunningham, J. (2018). Non-asymptotic analysis of quantum metrology protocols beyond the Cramér–Rao bound. *Journal of Physics Communications*, 2(1):015027.

[53] Santagati, R., Gentile, A., Knauer, S., Schmitt, S., Paesani, S., Granade, C., Wiebe, N., Osterkamp, C., McGuinness, L., Wang, J., Thompson, M., Rarity, J., Jelezko, F., and Laing, A. (2019). Magnetic-Field Learning Using a Single Electronic Spin in Diamond with One-Photon Readout at Room Temperature. *Phys. Rev. X*, 9(2):021019.

[54] Savukov, I. M. and Romalis, M. V. (2005). Effects of spin-exchange collisions in a high-density alkali-metal vapor in low magnetic fields. *Phys. Rev. A*, 71:023405.

[55] Schuff, J., Fiderer, L. J., and Braun, D. (2020). Improving the dynamics of quantum sensors with reinforcement learning. *New Journal of Physics*, 22(3):035001.

[56] Sheng, D., Li, S., Dural, N., and Romalis, M. V. (2013). Subfemtotesla Scalar Atomic Magnetometry Using Multipass Cells. *Phys. Rev. Lett.*, 110(16):160802.

[57] Simmons, S., Jones, J. A., Karlen, S. D., Ardavan, A., and Morton, J. J. L. (2010). Magnetic field sensors using 13-spin cat states. *Phys. Rev. A*, 82:022330.

[58] Streltsov, A., Adesso, G., and Plenio, M. B. (2017). Colloquium: quantum coherence as a resource. *Reviews of Modern Physics*, 89(4):041003.

[59] Takeuchi, M., Ichihara, S., Takano, T., Kumakura, M., Yabuzaki, T., and Takahashi, Y. (2005). Spin Squeezing via One-Axis Twisting with Coherent Light. *Phys. Rev. Lett.*, 94(2):023003.

[60] Tóth, G. and Apellaniz, I. (2014). Quantum metrology from a quantum information science perspective. *Journal of Physics A: Mathematical and Theoretical*, 47(42):424006.

[61] Wang, J., Paesani, S., Santagati, R., Knauer, S., Gentile, A. A., Wiebe, N., Petruzzella, M., O'Brien, J. L., Rarity, J. G., Laing, A., and Thompson, M. G. (2017). Experimental quantum Hamiltonian learning. *Nature Physics*, 13(6):551–555.

[62] Wasilewski, W., Jensen, K., Krauter, H., Renema, J. J., Balabas, M. V., and Polzik, E. S. (2010). Quantum Noise Limited and Entanglement-Assisted Magnetometry. *Phys. Rev. Lett.*, 104(13):133601.

[63] Wiebe, N. and Granade, C. (2016). Efficient Bayesian Phase Estimation. *Phys. Rev. Lett.*, 117(1):010503.

[64] Wiebe, N., Granade, C., Ferrie, C., and Cory, D. (2014). Hamiltonian Learning and Certification Using Quantum Resources. *Phys. Rev. Lett.*, 112(19):190501.

[65] Zwierz, M., Pérez-Delgado, C. A., and Kok, P. (2010). General Optimality of the Heisenberg Limit for Quantum Metrology. *Phys. Rev. Lett.*, 105:180402.

Quantum metrology with quantum-chaotic sensors

Lukas J. Fiderer[1] & Daniel Braun[1]

Quantum metrology promises high-precision measurements of classical parameters with far reaching implications for science and technology. So far, research has concentrated almost exclusively on quantum-enhancements in integrable systems, such as precessing spins or harmonic oscillators prepared in non-classical states. Here we show that large benefits can be drawn from rendering integrable quantum sensors chaotic, both in terms of achievable sensitivity as well as robustness to noise, while avoiding the challenge of preparing and protecting large-scale entanglement. We apply the method to spin-precession magnetometry and show in particular that the sensitivity of state-of-the-art magnetometers can be further enhanced by subjecting the spin-precession to non-linear kicks that renders the dynamics chaotic.

[1] Institute for Theoretical Physics, University of Tübingen, Auf der Morgenstelle 14, 72076 Tübingen, Germany. Correspondence and requests for materials should be addressed to L.J.F. (email: lukas.fiderer@uni-tuebingen.de) or to D.B. (email: daniel.braun@uni-tuebingen.de)

Quantum-enhanced measurements (QEM) use quantum effects in order to measure physical quantities with larger precision than what is possible classically with comparable resources. QEMs are therefore expected to have large impact in many areas, such as improvement of frequency standards[1–5], gravitational wave detection[6,7], navigation[8], remote sensing[9], or measurement of very small magnetic fields[10]. A well-known example is the use of so-called NOON states in an interferometer, where a state with N photons in one arm of the interferometer and zero in the other is superposed with the opposite situation[11]. It was shown that the smallest phase shift that such an interferometer could measure scales as $1/N$, a large improvement over the standard $1/\sqrt{N}$ behavior that one obtains from ordinary laser light. The latter scaling is known as the standard quantum limit (SQL), and the $1/N$ scaling as the Heisenberg limit (HL). So far the SQL has been beaten only in few experiments, and only for small N (see e.g., [3,12,13]), as the required non-classical states are difficult to prepare and stabilize and are prone to decoherence.

Sensing devices used in quantum metrology so far have been based almost exclusively on integrable systems, such as precessing spins (e.g., nuclear spins, NV centers, etc.) or harmonic oscillators (e.g., modes of an electro-magnetic field or mechanical oscillators), prepared in non-classical states (see ref. [14] for a recent review). The idea of the present work is to achieve enhanced measurement precision with readily accessible input states by disrupting the parameter coding by a sequence of controlled pulses that renders the dynamics chaotic. At first sight this may appear a bad idea, as measuring something precisely requires well-defined, reproducible behavior, whereas classical chaos is associated with unpredictible long-term behavior. However, the extreme sensitivity to initial conditions underlying classically chaotic behavior is absent in the quantum world with its unitary dynamics in Hilbert space that preserves distances between states. In turn, quantum-chaotic dynamics can lead to exponential sensitivity with respect to parameters of the system[15].

The sensitivity to changes of a parameter of quantum-chaotic systems has been studied in great detail with the technique of Loschmidt echo[16], which measures the overlap between a state propagated forward with a unitary operator and propagated backward with a slightly perturbed unitary operator. In the limit of infinitesimally small perturbation, the Loschmidt echo turns out to be directly related to the quantum Fisher information (QFI) that determines the smallest uncertainty with which a parameter can be estimated. Hence, a wealth of known results from quantum chaos can be immediately translated to study the ultimate sensitivity of quantum-chaotic sensors. In particular, linear response expressions for fidelity can be directly transfered to the exact expressions for the QFI.

Ideas of replacing entanglement creation by dynamics were proposed previously[17–21], but focussed on initial state preparation, or robustness of the readout[22,23], without introducing or exploiting chaotic dynamics during the parameter encoding. They are hence comparable to spin-squeezing of the input state[24]. Quantum chaos is also favorable for state tomography of random initial states with weak continuous time measurement[25,26], but no attempt was made to use this for precision measurements of a parameter. A recent review of other approaches to quantum-enhanced metrology that avoid initial entanglement can be found in ref. [27].

We study quantum-chaotic enhancement of sensitivity at the example of the measurement of a classical magnetic field with a spin-precession magnetometer. In these devices that count amongst the most sensitive magnetometers currently available[28–32], the magnetic field is coded in a precession frequency of atomic spins that act as the sensor. We show that the precision of the magnetic-field measurement can be substantially enhanced by

non-linearly kicking the spin during the precession phase and driving it into a chaotic regime. The initial state can be chosen as an essentially classical state, in particular a state without initial entanglement. The enhancement is robust with respect to decoherence or dissipation. We demonstrate this by modeling the magnetometer on two different levels: firstly as a kicked top, a well-known system in quantum chaos to which we add dissipation through superradiant damping; and secondly with a detailed realistic model of a spin-exchange-relaxation-free atom-vapor magnetometer including all relevant decoherence mechanisms[28,33], to which we add non-linear kicks.

Results

Physical model of a quantum-chaotic sensor. As a sensor we consider a kicked top (KT), a well-studied quantum-chaotic system[34–36] described by the time-dependent Hamiltonian

$$H_{KT}(t) = \alpha J_z + \frac{k}{2J} J_y^2 \sum_{n=-\infty}^{\infty} \tau \delta(t - n\tau), \qquad (1)$$

where J_i ($i = x, y, z$) are components of the (pseudo-)angular momentum operator, $J \equiv j + 1/2$, and we set $\hbar = 1$. J_z generates a precession of the (pseudo-)angular momentum vector about the z-axis with precession angle α which is the parameter we want to estimate. "Pseudo" refers to the fact that the physical system need not be an actual physical spin, but can be any system with $2j + 1$ basis states on which the J_i act accordingly. For a physical spin-j in a magnetic field B in z-direction, α is directly proportional to B. The J_y^2-term is the non-linearity, assumed to act instantaneously compared to the precession, controlled by the kicking strength k and applied periodically with a period τ that leads to chaotic behavior. The system can be described stroboscopically with discrete time t in units of τ (set to $\tau = 1$ in the following),

$$|\psi(t)\rangle = U_\alpha(k)|\psi(t-1)\rangle = U_\alpha^t(k)|\psi(0)\rangle \qquad (2)$$

with the unitary Floquet-operator

$$U_\alpha(k) = T \exp\left(-i \int_t^{t+1} dt' H_{KT}(t')\right) = e^{-ik \frac{J_y^2}{2J}} e^{-i\alpha J_z} \qquad (3)$$

that propagates the state of the system from right after a kick to right after the next kick[34–36]. T denotes time-ordering. The total spin is conserved, and $1/J$ can be identified with an effective $\hbar$, such that the limit $j \to \infty$ corresponds to the classical limit, where $X = J_x/J$, $Y = J_y/J$, $Z = J_z/J$ become classical variables confined to the unit sphere. (Z, ϕ) can be identified with classical phase space variables, where ϕ is the azimuthal angle of $\mathbf{X} = (X, Y, Z)$[36]. For $k = 0$, the dynamics is integrable, as the precession conserves Z and increases ϕ by α for each application of $U_\alpha(0)$. Phase space portraits of the corresponding classical map show that for $k \lesssim 2.5$, the dynamics remains close to integrable with large visible Kolmogorov–Arnold–Moser tori, whereas for $k \gtrsim 3.0$ the chaotic dynamics dominates[36].

States that correspond most closely to classical phase space points located at (θ, ϕ) are SU(2)-coherent states ("spin-coherent states", or "coherent states" for short), defined as

$$|j, \theta, \phi\rangle = \sum_{m=-j}^{j} \sqrt{\binom{2j}{j-m}} \sin(\theta/2)^{j-m} \cos(\theta/2)^{j+m} e^{i(j-m)\phi}|jm\rangle \qquad (4)$$

in the usual notation of angular momentum states $|jm\rangle$ (eigenbasis of $\mathbf{J}^2$ and J_z with eigenvalues $j(j+1)$ and m, $2j \in \mathbb{N}$, $m = -j, -j+1, \ldots, j$). They are localized at polar and azimuthal angles θ, ϕ with smallest possible uncertainty of all spin-j states
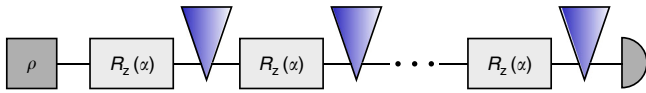
Fig. 1 Schematic representation of the parameter encoding: propagation starts on the left with an initial state ρ and ends on the right with a measurement (semi-circle symbol). The encoding through linear precession $R_z(\alpha)$ about the z-axis by an angle α is periodically disrupted through parameter independent, non-linear, controlled kicks (blue triangles) that can render the system chaotic

(associated circular area $\sim 1/j$ in phase space). They remain coherent states under the action of $U_\alpha(0)$, i.e., just get rotated, $\phi \mapsto \phi + \alpha$. For the KT, the parameter encoding of α in the quantum state breaks with the standard encoding scheme (initial state preparation, parameter-dependent precession, measurement) by periodically disrupting the coding evolution with parameter-independent kicks that generate chaotic behavior (see Fig. 1).

An experimental realization of the kicked top was proposed in ref. [37], including superradiant dissipation. It has been realized experimentally[38] in cold cesium vapor using optical pulses (see Supplementary Note 1 for details).

Quantum parameter estimation theory. Quantum measurements are most conveniently described by a positive-operator valued measure (POVM) $\{\Pi_\xi\}$ with positive operators Π_ξ (POVM elements) that fulfill $\int d\xi \Pi_\xi = \mathbf{1}$. Measuring a quantum state described by a density operator ρ_α yields for a given POVM and a given parameter α encoded in the quantum state a probability distribution $p_\alpha(\xi) = \text{tr}(\Pi_\xi \rho_\alpha)$ of measurement results ξ. The Fisher information $I_{\text{Fisher},\alpha}$ is then defined by

$$I_{\text{Fisher},\alpha} := \int d\xi \frac{(dp_\alpha(\xi)/d\alpha)^2}{p_\alpha(\xi)}. \quad (5)$$

The minimal achievable uncertainty, i.e., the variance of the estimator $\text{Var}(\alpha_{\text{est}})$, with which a parameter α of a state ρ_α can be estimated for a given POVM with M independent measurements is given by the Cramér–Rao bound, $\text{Var}(\alpha_{\text{est}}) \geq 1/(M I_{\text{Fisher},\alpha})$. Further optimization over all possible (POVM-)measurements leads to the quantum-Cramér–Rao bound (QCRB),

$$\text{Var}(\alpha_{\text{est}}) \geq \frac{1}{M I_\alpha}, \quad (6)$$

which presents an ultimate bound on the minimal achievable uncertainty, where I_α is the quantum Fisher information (QFI), and M the number of independent measurements[39].

The QFI is related to the Bures distance ds^2_{Bures} between the states ρ_α and $\rho_{\alpha+d\alpha}$, separated by an infinitesimal change of the parameter α, $ds^2_{\text{Bures}}(\rho,\sigma) \equiv 2(1 - \sqrt{F(\rho,\sigma)})$. The fidelity $F(\rho,\sigma)$ is defined as $F(\rho,\sigma) = \left\| \rho^{1/2}\sigma^{1/2} \right\|_1^2$, and $\|A\|_1 \equiv \text{tr}\sqrt{AA^\dagger}$ denotes the trace norm[40]. With this[41],

$$I_\alpha = 4 ds^2_{\text{Bures}}(\rho_\alpha, \rho_{\alpha+d\alpha})/d\alpha^2. \quad (7)$$

For pure states $\rho = |\psi\rangle\langle\psi|$, $\sigma = |\phi\rangle\langle\phi|$, the fidelity is simply given by $F(\rho,\sigma) = |\langle\psi|\phi\rangle|^2$. A parameter coded in a pure state via the unitary transformation $|\psi_\alpha\rangle = e^{-i\alpha G}|\psi(0)\rangle$ with hermitian generator G gives the QFI[42]

$$I_\alpha = 4\text{Var}(G) \equiv 4(\langle G^2 \rangle - \langle G \rangle^2), \quad (8)$$

which holds for all α, and where $\langle\cdot\rangle \equiv \langle\psi_\alpha| \cdot |\psi_\alpha\rangle$.

Loschmidt echo. The sensitivity to changes of a parameter of quantum-chaotic systems has been studied in great detail with the technique of Loschmidt echo[16], which measures the overlap $F_\epsilon(t)$ between a state propagated forward with a unitary operator $U_\alpha(t)$ and propagated backward with a slightly perturbed unitary operator $U_{\alpha+\epsilon}(-t) = U^\dagger_{\alpha+\epsilon}(t)$, where $U_\alpha(t) = T\exp\left(-\frac{i}{\hbar}\int_0^t dt' H_\alpha(t')\right)$ with the time ordering operator T, the Hamiltonian, $H_{\alpha+\epsilon}(t) = H_\alpha(t) + \epsilon V(t)$ and the perturbation $V(t)$,

$$F_\epsilon(t) = |\langle\psi(0)|U_\alpha(t)U_{\alpha+\epsilon}(-t)\psi(0)\rangle|^2. \quad (9)$$

F_ϵ is exactly the fidelity that enters via the Bures distance in the definition Eq. (7) of the QFI for pure states, such that $I_\alpha(t) = \lim_{\epsilon\to 0} 4\frac{1-F_\epsilon(t)}{\epsilon^2}$.

Benchmarks. In order to assess the influence of the kicking on the QFI, we calculate as benchmarks the QFI for the (integrable) top with Floquet operator $U_\alpha(0)$ without kicking, both for an initial coherent state and for a Greenberger–Horne–Zeilinger (GHZ) state $|\psi_{\text{GHZ}}\rangle = (|j,j\rangle + |j,-j\rangle)/\sqrt{2}$. The latter is the equivalent of a NOON state written in terms of (pseudo-)angular momentum states. The QFI for the time evolution Eq. (2) of a top with Floquet operator $U_\alpha(0)$ is given by Eq. (8) with $G = J_z$. For an initial coherent state located at θ, ϕ it results in a QFI

$$I_\alpha(t) = 2t^2 j\sin^2\theta. \quad (10)$$

As expected, $I_\alpha(t) = 0$ for $\theta = 0$ where the coherent state is an eigenstate of $U_\alpha(0)$. The scaling $\propto t^2$ is typical of quantum coherence, and $I_\alpha(t) \propto j$ signifies a SQL-type scaling with $N = 2j$, when the spin-j is composed of N spin-$\frac{1}{2}$ particles in a state invariant under permutations of particles. For the benchmark, we use the optimal value $\theta = \pi/2$ in Eq. (10), i.e., $I_{\text{top,CS}} \equiv 2t^2 j$. For a GHZ state, the QFI becomes

$$I_\alpha(t) = 4t^2 j^2 \equiv I_{\text{top,GHZ}}, \quad (11)$$

which clearly displays the HL-type scaling $\propto (2j)^2 \equiv N^2$.

Results for the kicked top without dissipation. In the fully chaotic case, known results for the Loschmidt echo suggest a QFI of the KT $\propto tj^2$ for times t with $t_E < t < t_H$, where $t_E = \frac{1}{\lambda}\ln\left(\frac{\Omega_V}{h^d}\right)$ is the Ehrenfest time, and $t_H = \hbar/\Delta$ the Heisenberg time; λ is the Lyapunov exponent, Ω_V the volume of phase-space, h^d with d the number of degrees of freedom the volume of a Planck cell, and Δ the mean energy level spacing[16,36,43]. For the kicked top, $h^d \simeq \Omega_V/(2J)$. More precisely, we find for $t \simeq t_E$ a QFI $I_\alpha \propto tj^2$ and for $t \gg t_H$ (see Methods)

$$I(t) = 8s\sigma_{\text{cl}}t^2 J, \quad (12)$$

where s denotes the number of invariant subspaces s of the Hilbert space ($s = 3$ for the kicked top with $\alpha = \pi/2$, see page 359 in ref. [15]), and σ_{cl} is a transport coefficient that can be calculated numerically. The infinitesimally small perturbation relevant for the QFI makes that one is always in the perturbative regime[44,45]. The Gaussian decay of Loschmidt echo characteristic of that regime becomes the slower the smaller the perturbation and goes over into a power law in the limit of infinitesimally small perturbation[16].

The numerical results for the QFI in Fig. 2 illustrate a crossover of power-law scalings in the fully chaotic case ($k = 30$) for an initial coherent state located on the equator $(\theta, \phi) = (\pi/2, \pi/2)$. The analytical Loschmidt echo results are nicely reproduced: a smooth transition in scaling from $tj^2 \to t^2 j$ for $t = t_E \to t \gtrsim t_H$ can be observed and confirms Eqs. (15) and (16) in the Methods for
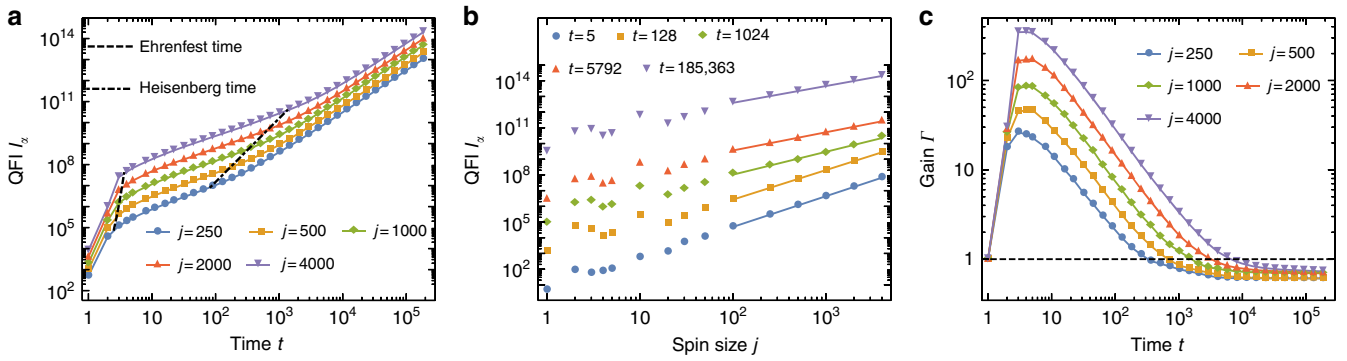
Fig. 2 Quantum-chaotic enhancement of sensitivity. **a** t-scaling of the quantum Fisher information (QFI) I_α in the strongly chaotic case. Dashed and dash-dotted lines indicate Ehrenfest and Heisenberg times, respectively. **b** j-scaling of the QFI. Fits have slopes 1.96, 1.88, 1.46, 1.16, and 1.08 in increasing order of t. **c** Gain $\Gamma = I_{\alpha,\mathrm{KT}}/I_{\mathrm{top,CS}}$ as function of time t for different values of spin size j. The dashed black line marks the threshold $\Gamma = 1$. Kicking strength $k = 30$, and initial coherent state at $(\theta, \phi) = (\pi/2, \pi/2)$ in all plots
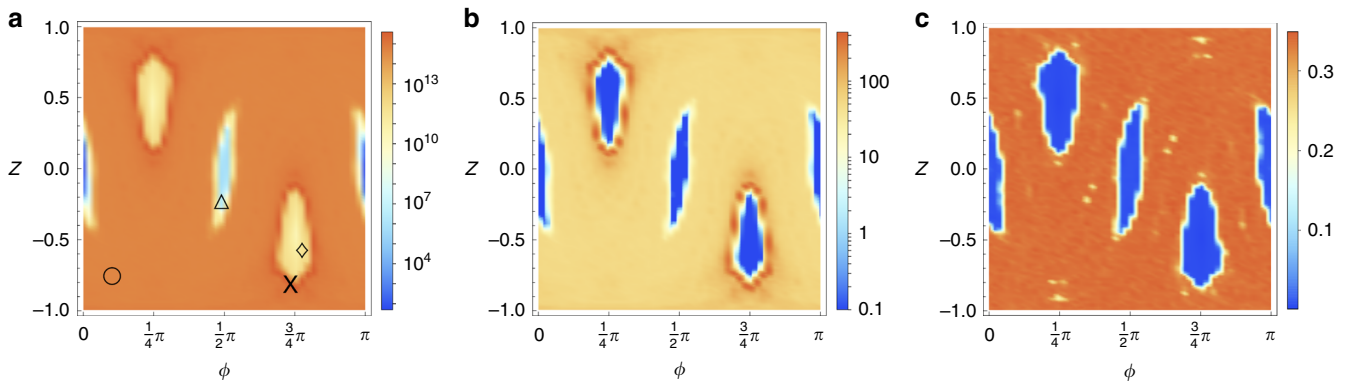

Fig. 3 Portraits of a mixed phase space for large spin size $j = 4000$. The heat maps depict quantum Fisher information (QFI) in panel **a** and gain Γ in panel **b** at time $t = 2^{15}$ and kicking strength $k = 3$. $\Gamma < 0.1$ is depicted as $\Gamma = 0.1$ to simplify the representation. A gain of more than two orders of magnitude in the QFI is observed for edge states, localized on the border of the stability islands. For comparison, panel **c** depicts the classical Lyapunov exponent λ
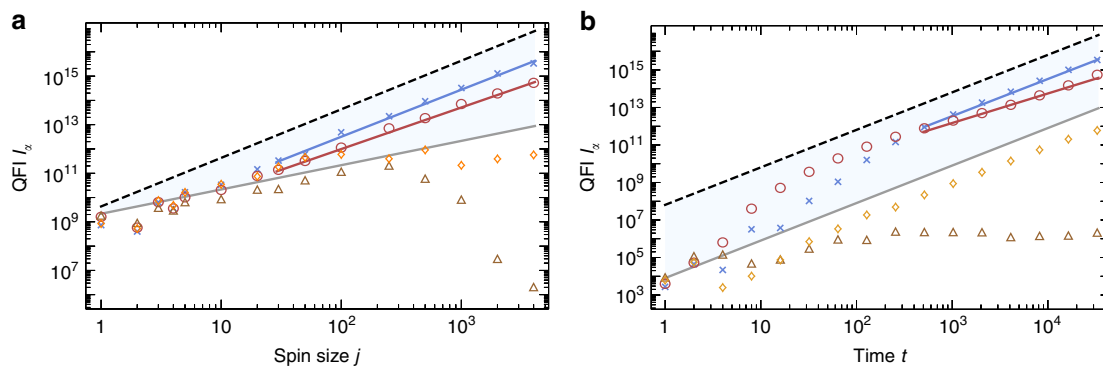
Fig. 4 Scaling of quantum Fisher information (QFI) in different areas of a mixed phase space. QFI $I_\alpha(j)$ (panel **a** for time $t = 2^{15}$) and $I_\alpha(t)$ (panel **b** for spin size $j = 4000$) for kicking strength $k = 3$ and different initial coherent states $|\theta, \phi\rangle$ (as marked in panel **a** of Fig. 3): inside an equatorial (brown triangles, $|1.82, 1.54\rangle$) and a non-equatorial (orange diamonds, $|2.20, 2.44\rangle$) stability island, in the chaotic sea (red circles, $|2.46, 0.32\rangle$), and an edge state (blue crosses, $|2.56, 2.31\rangle$). Benchmarks $I_{\mathrm{top,CS}}$ (gray line) and $I_{\mathrm{top,GHZ}}$ (black dashed line) represent the standard quantum limit and Heisenberg limit, respectively. Fits for the edge state and the state in the chaotic sea exhibit a slope of 1.94 and 1.71 for the j-scaling, and 1.98 and 1.57 for the t-scaling

$t > t_\mathrm{E} = \ln(2J)/\lambda$, with the numerically determined Lyapunov exponent $\lambda \simeq 2.4733$, and Eq. (12) for $t \gtrsim t_\mathrm{H} \simeq J/3$[16]. We find for relatively large j ($j \gtrsim 10^2$) a scaling $I_\alpha \propto j^{1.08}$ in good agreement with Eq. (12) predicting a linear j-dependence for large $t \gtrsim t_\mathrm{H}$. During the transient time $t < t_\mathrm{E}$, when the state is spread over the phase space, QFI shows a rapid growth that can be attributed to the generation of coherences that are particularly sensitive to the precession.

The comparison of the KT's QFI $I_{\alpha,\mathrm{KT}}$ with the benchmark $I_{\mathrm{top,CS}}$ of the integrable top in Fig. 2c shows that a gain of more than two orders of magnitude for $j = 4000$ can be found at $t \lesssim t_\mathrm{E}$. Around t_E the state has spread over the phase space and has developed coherences while for larger times $t > t_\mathrm{E}$ the top catches up due to its superior time scaling (t^2 vs. t). The long-time behavior yields a constant gain <1, which means that the top
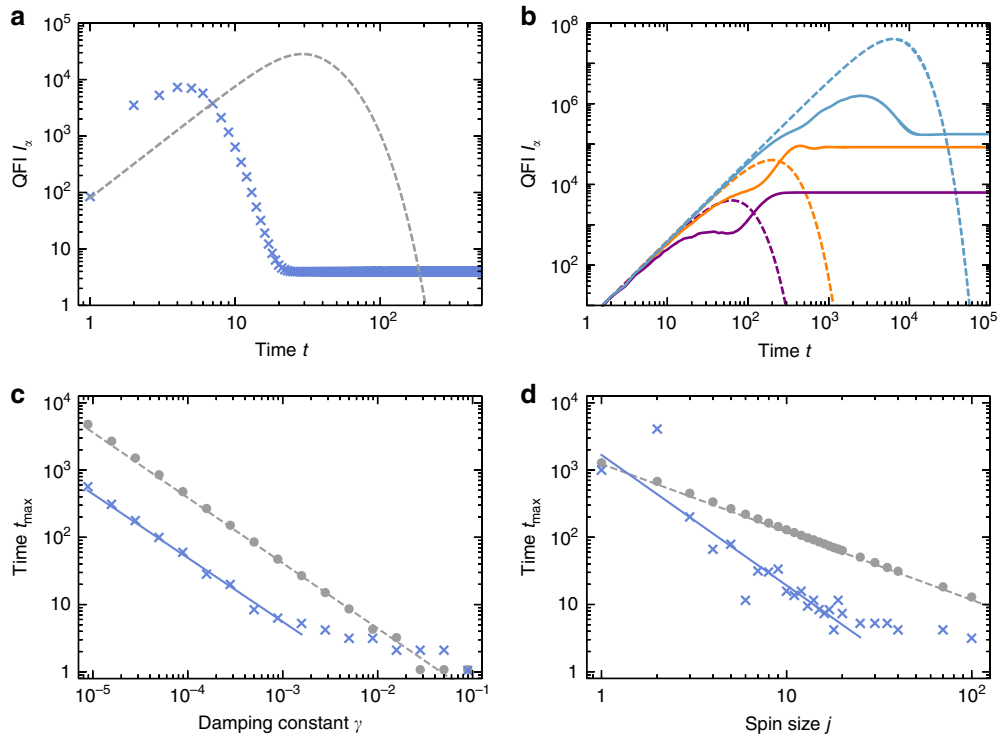
Fig. 5 Time evolution of the quantum Fisher information (QFI) for the dissipative kicked top. In all subplots, we look at an initial coherent state at $(\theta, \phi) = (\pi/2, \pi/2)$. **a** Exemplary behavior as function of time for a dissipative top (DT, dashed gray line) and a chaotic (kicking strength $k = 30$) dissipative kicked top (DKT, blue crosses) for spin size $j = 40$, damping constant $\gamma = 0.5 \times 10^{-3}$. **b** High plateau values of the QFI are achieved for $j = 2$ and $k = 30$ for various values of the damping constant ($\gamma = 0.5 \times 10^{-2}$ for the purple line, $\gamma = 1.58 \times 10^{-3}$ for the orange line, and $\gamma = 0.5 \times 10^{-4}$ for the blue line), while dashed lines represent corresponding QFI with $k = 0$. **c**, **d** Time t_{max} at which the QFI of the DT (gray dots) and DKT (blue crosses) reaches its maximum as function of γ and j, respectively. The fits for the DT (gray line) exhibit a slope of -0.97 and -1.01, and the fits for the DKT (blue, dashed) a slope of -0.95 and -1.94 for scaling with γ and j, respectively. Parameters $j = 15$ in **c** and $\gamma = 0.5 \times 10^{-3}$ in **d**. The plotted range of the fits corresponds to the fitted data

achieves a higher QFI than the KT in this regime. The gain becomes constant as both top and KT exhibit a t^2 scaling of the QFI.

Whereas in the fully chaotic regime the memory of the initial state is rapidly forgotten, and the initial state can therefore be chosen anywhere in the chaotic sea without changing much the QFI, the situation is very different in the case of a mixed phase space, in which stability islands are still present. Figure 3 shows phase space distributions for $k = 3$ of QFI and gain $\Gamma = I_{\alpha,KT}/I_{top,CS}$ exemplarily for large t and j ($t = 2^{15}$, $j = 4000$) in comparison with the classical Lyapunov exponent, where ϕ, Z signify the position of the initial coherent state.

The QFI nicely reproduces the essential structure in classical phase space for the Lyapunov exponent λ (see Methods for the calculation of λ). Outside the regions of classically regular motion, the KT clearly outperforms the top by more than two orders of magnitude. Remarkably, the QFI is highest at the boundary of non-equatorial islands of classically regular motion. Coherent states located on that boundary will be called edge states.

The diverse dynamics for different phase space regions calls for dedicated analyses. Figure 4 depicts the QFI with respect to j and t. The blue area is lower and upper bounded by the benchmarks $I_{top,CS}$ and $I_{top,GHZ}$, Eq. (11), respectively.

We find that initial states in the chaotic sea perform best for small times while for larger times ($t \gtrsim 300$ for $j = 4000$) edge states perform best. Note that this is numerically confirmed up to very high QFI values ($>10^{14}$). The superiority of edge states holds for $j \gtrsim 10$ for large times ($t \gtrsim 10^3$, see Fig. 4a). Large values of j allow one to localize states essentially within a stability island. A coherent state localized within a non-equatorial stability island shows a quadratic t-scaling analog to the regular top. For a state

$|\psi_{eq}\rangle$ localized around a point within an equatorial island of stability the QFI drastically decays with increasing j (brown triangles). The scaling with t for $j = 4000$ reveals that QFI does not increase with t in this case, it freezes. One can understand the phenomenon as arising from a freeze of fidelity due to a vanishing time averaged perturbation[16,46]: the dynamics restricts the states to the equatorial stability island with time average $\overline{\langle \psi_{eq} | (U_\alpha^t)^\dagger (k) J_z U_\alpha^t (k) | \psi_{eq} \rangle} = 0$. This can be verified numerically, and contrasted with the dynamics when initial states are localized in the chaotic sea or on a non-equatorial island.

Results for the dissipative kicked top. For any quantum-enhanced measurement, it is important to assess the influence of dissipation and decoherence. We first study superradiant damping[47–51] as this enables a proof-of-principle demonstration with an analytically accessible propagator for the master equation with spins up to $j \simeq 200$ and correspondingly large gains. Then, in the next subsection, we show by detailed and realistic modeling including all the relevant decoherence mechanisms that sensitivity of existing state-of-the-art alkali-vapor-based spin-precession magnetometers in the spin-exchange-relaxation-free (SERF) regime can be enhanced by non-linear kicks.

At sufficiently low temperatures ($k_B T \ll \hbar\omega$, where $\hbar\omega$ is the level spacing between adjacent states $|jm\rangle$) superradiance is described by the Markovian master equation for the spin-density matrix $\rho(t)$ with continuous time,

$$\frac{d}{dt}\rho(t) = \gamma([J_-, \rho(t)J_+] + [J_-\rho(t), J_+]) \equiv \rho(t), \quad (13)$$

where $J_\pm \equiv J_x \pm iJ_y$, with the commutator $[A, B] = AB - BA$, and γ is the dissipation rate, with the formal solution $\rho(t) = \exp(\Lambda t) \rho(0) \equiv D(t)\rho(0)$. The full evolution is governed by $d\rho(t)/dt = \Lambda\rho(t) - i\hbar[H_{KT}(t), \rho(t)]$. Dissipation and precession about the z-axis commute, $\Lambda(J_z\rho J_z) = J_z(\Lambda\rho)J_z$. Λ can therefore act permanently, leading to the propagator P of ρ from discrete time t to $t + \tau$ for the dissipative kicked top (DKT)[36,52]

$$\rho(t + \tau) = P\rho(t) = U_\alpha(k)(D(\tau)\rho(t))U_\alpha^\dagger(k). \quad (14)$$

For the sake of simplicity, we again set the period $\tau = 1$, and t is taken again as discrete time in units of τ. Then, $\gamma\tau \equiv \gamma$ controls the effective dissipation between two unitary propagations. Classically, the DKT shows a strange attractor in phase space with a fractal dimension that reduces from $d = 2$ at $\gamma = 0$ to $d = 0$ for large γ, when the attractor shrinks to a point attractor and migrates towards the ground state $|j, -j\rangle$[52]. Quantum mechanically, one finds a Wigner function with support on a smeared out version of the strange attractor that describes a non-equilibrium steady state reached after many iterations. Such a non-trivial state is only possible through the periodic addition of energy due to the kicking. Because of the filigrane structure of the strange attractor, one might hope for relatively large QFI, whereas without kicking the system would decay to the ground state, where the QFI vanishes. Creation of steady non-equilibrium states may therefore offer a way out of the decoherence problem in quantum metrology, see also section V.C in ref. [27] for similar ideas.

Vanishing kicking strength, i.e., the dissipative top (DT) obtained from the DKT by setting $k = 0$, will serve again as benchmark. While in the dissipation-free regime, we took the top's QFI and with it its SQL-scaling ($\propto jt^2$) as reference, SQL-scaling no longer represents a proper benchmark, because damping typically corrupts QFI with increasing time. To illustrate the typical behavior of QFI, we exemplarily choose certain spin sizes j and damping constants γ here and in the following, such as $j = 40$ and $\gamma = 0.5 \times 10^{-3}$ in Fig. 5a, while computational limitations restrict us to $j \lesssim 200$.

Figure 5 shows the typical overall behavior of the QFI of the DT and DKT as function of time: after a steep initial rise $\propto t^2$, the QFI reaches a maximum whose value is the larger the smaller the dissipation. Then the QFI decays again, dropping to zero for the DT, and a plateau value for the DKT. The time at which the maximum value is reached decays roughly as $1/(j\gamma)$ for the DT, and as $1/j^{0.95}$ and $1/\gamma^{1.94}$ for the DKT. The plateau itself is in general relatively small for the limited values of j that could be investigated numerically, but it should be kept in mind that (i) for the DT the plateau does not even exist (QFI always decays to zero for large time, as dissipation drives the system to the ground state $|j, -j\rangle$ which is an eigenstate of J_z and hence insensitive to precession); and (ii) there are exceptionally large plateau values even for small j, see e.g., the case of $j = 2$ in Fig. 5b. There, for $\gamma = 1.58 \times 10^{-3}$, the plateau value is larger by a factor 2.35 than the DT's QFI optimized over all initial coherent states for all times. Note that since $\Lambda(J_z\rho J_z) = J_z(\Lambda\rho)J_z$, for the DT an initial precession about the z-axis that is part of the state preparation can be moved to the end of the evolution and does not influence the QFI of the DT. Optimizing over the initial coherent state can thus be restricted to optimizing over θ.

When considering dynamics, it is natural also to include time as a resource. Indeed, experimental sensitivities are normally given as uncertainties per square root of Hertz: longer (classical) averaging reduces the uncertainty as $1/\sqrt{T_{av}}$ with averaging time $t = T_{av}$. For fair comparisons, one multiplies the achieved uncertainty with $\sqrt{T_{av}}$. Correspondingly, we now compare rescaled QFI and Fisher information, namely $I_\alpha^{(t)} \equiv I_\alpha/T_{av}$,
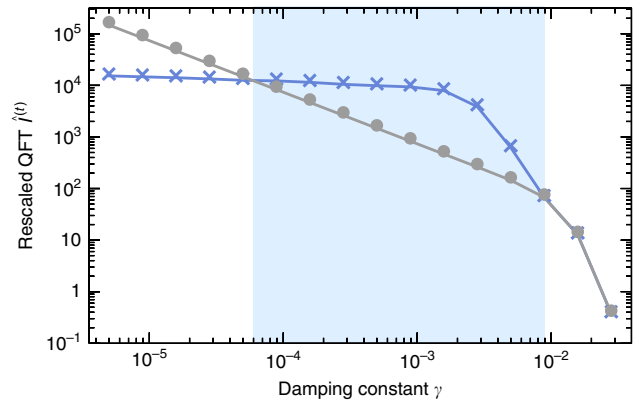
Fig. 6 Enhancement in measurement precision through kicking (blue crosses) is found over a broad range of damping strengths. Comparison of the maximal rescaled quantum Fisher information $\hat{I}_\alpha^{(t)}$ for the dissipative top (gray dots) and the dissipative kicked top (blue crosses); kicking strength $k = 30$ and spin size $j = 100$. In both cases, $\hat{I}_\alpha^{(t)}$ was optimized over the location of initial coherent states. The blue-shaded area marks the range $1.2 \lesssim 2\gamma j^2 \lesssim 180$ where the reference is outperformed

$I_{Fisher,\alpha}^{(t)} \equiv I_{Fisher,\alpha}/T_{av}$. A protocol that reaches a given level of QFI more rapidly has then an advantage, and best precision corresponds to the maximum rescaled QFI or Fisher information, $\hat{I}_\alpha^{(t)} \equiv \max_t I_\alpha^{(t)}$ or $\hat{I}_{Fisher,\alpha}^{(t)} \equiv \max_t I_{Fisher,\alpha}^{(t)}$.

Figure 6 shows that in a broad range of dampings that are sufficiently strong for the QFI to decay early, the maximum rescaled QFI of the DKT beats that quantity of the DT by up to an order of magnitude. Both quantities were optimized over the location of the initial coherent states.

Figure 7 shows $\hat{I}_\alpha^{(t)}$ and the gain in that quantity compared to the non-kicked case as function of both the damping and the kicking strength. One sees that in the intermediate damping regime ($\gamma \simeq 10^{-3}$) the gain increases with kicking strength, i.e., increasingly chaotic dynamics.

For exploiting the enhanced sensitivity shown to exist through the large QFI, one needs also to specify the actual measurement of the probe. In principle, the QCRB formalism allows one to identify the optimal POVM measurement if the parameter is known, but these may not always be realistic. In Fig. 8, we investigate J_y as a feasible example for a measurement for a spin size $j = 200$ after $t = 2$ time steps. We find that there exists a broad range of kicking strengths where the reference (state-optimized but $k = 0$) is outperformed in both cases, with and without dissipation. In a realistic experiment, control parameters such as the kicking strength are subjected to variations. A 5% variance in k, which was reported in ref. [38], reduces the Fisher information only marginally and does not challenge the advantage of kicking. This can be calculated by rewriting the probability that enters in the Fisher information in Eq. (5) according to the law of total probability, $p_\alpha(\xi) = \int dk p(k)p_\alpha(\xi|k)$ where $p(k)$ is an assumed Gaussian distribution of k values with 5% variance and $p_\alpha(\xi|k) = tr[\Pi_\xi \rho_\alpha(k)]$ with Π_ξ a POVM element and $\rho_\alpha(k)$ the state for a given k value. The advantage from kicking remains when investigating a rescaled and time-optimized Fisher information (not shown in Fig. 8).

Improving a SERF magnetometer. We finally show that quantum-chaotically enhanced sensitivity can be achieved in state-of-the-art magnetometers by investigating a rather realistic and detailed model of an alkali-vapor-based spin-precession magnetometer acting in the SERF regime. SERF magentometers count amongst the most sensitive magnetometers for detecting
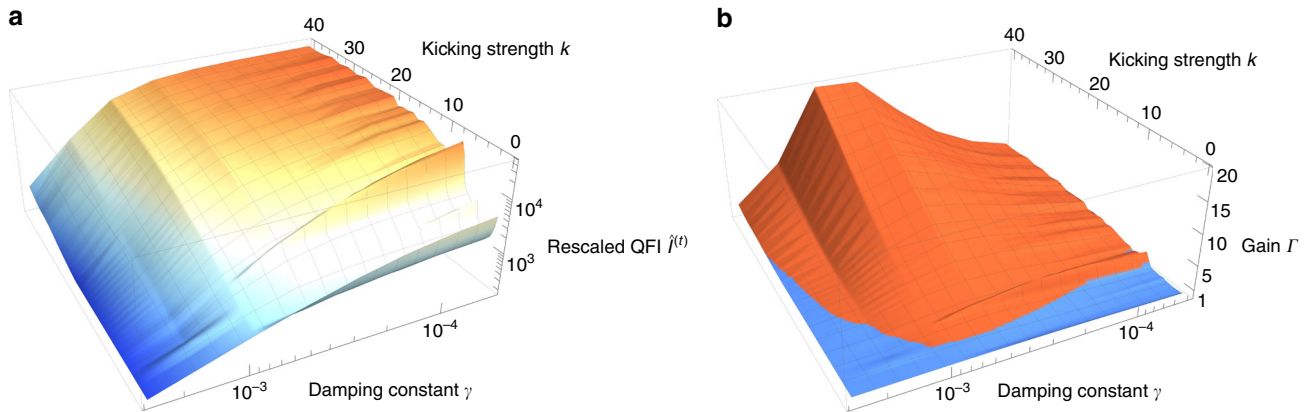
Fig. 7 Rescaled quantum Fisher information (QFI) and gains in measurement precision. Rescaled QFI of the dissipative kicked top $\hat{l}_{\alpha,\text{DKT}}^{(t)}(\theta = \pi/2, \phi = \pi/2)$ in panel **a** and gain $\Gamma = \frac{\hat{l}_{\alpha,\text{DKT}}^{(t)}(\theta=\pi/2,\phi=\pi/2)}{\hat{l}_{\alpha,\text{DT}}^{(t)}}$ in panel **b** as function of damping constant γ and kicking strength k at $j = 200$. Note that in this case $\hat{l}_{\alpha}^{(t)}$ is optimized over initial states only for the dissipative top
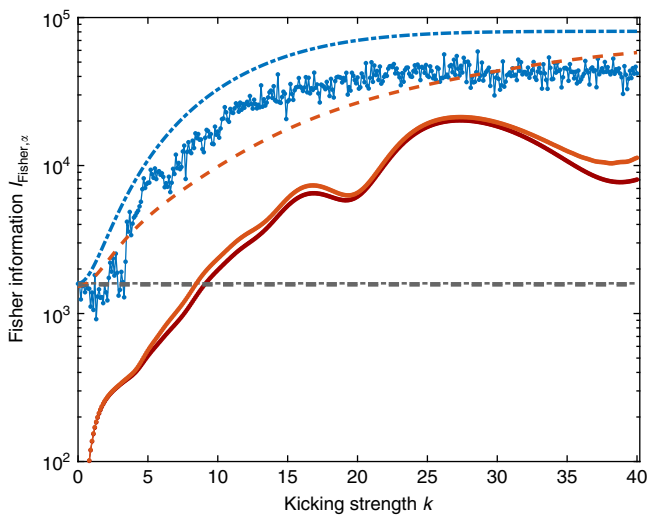
Fig. 8 Performance of an exemplary spin-component measurement with superradiance damping. Fisher information $I_{\text{Fisher},\alpha}$ related to measuring the y-component of the spin, J_y, after $t = 2$ time steps without dissipation (blue line) as well as in the presence of dissipation (bright red line, damping constant $\gamma = 0.5 \times 10^{-3}$), upper bounded by corresponding quantum Fisher informations (blue dash-dotted and red dashed lines), for spin size $j = 200$, and an initial state at $(\theta, \phi) = (\pi/2, \pi/2)$. For the dissipative case, Fisher information with a 5% uncertainty in the kicking strength is given by the dark red line slightly below the bright red line. Horizontal gray lines represent benchmarks (kicking strength $k = 0$) for $t = 2$ optimized over initial states (dashed with dissipation and dash-dotted without; lines are almost on top of each other). In both cases the benchmark is clearly outperformed for $k \gtrsim 3.5$ and $k \gtrsim 10.6$ without and with dissipation, respectively

small quasi-static magnetic fields[28–32]. We consider a cesium-vapor magnetometer at room temperature in the SERF regime similar to experiments with rubidium in ref. [53]. Kicks on the single cesium-atom spins can be realized as in ref. [38] by exploiting the spin-dependent rank-2 (ac Stark) light-shift generated with the help of an off-resonant laser pulse. Typical SERF magnetometers working at higher temperatures with high buffer-gas pressures exhibit an unresolved excited state hyperfine splitting due to pressure broadening, which makes kicks based on rank-2

light-shifts ineffective. Dynamics are modeled in the electronic ground state $6^2S_{1/2}$ of ^{133}Cs that splits into total spins of $f = 3$ and $f = 4$, where kicks predominantly act on the $f = 3$ manifold.

The model is quite different from the foregoing superradiance model because of a different decoherence mechanism originating from collisions of Cs atoms in the vapor cell: We include spin-exchange and spin-destruction relaxation, as well as additional decoherence induced by the optical implementation of the kicks. With this implementation of kicks one is confined to a small spin size $f = 3$ of single atoms, such that the large improvements in sensitivity found for the large spins discussed above cannot be expected. Nevertheless, we still find a clear gain in the sensitivity and an improved robustness to decoherence due to kicking. Details of the model described with a master equation[33,54] can be found in the Supplementary Note 2.

Spins of cesium atoms are initially pumped into a state spin-polarized in z-direction orthogonal to the magnetic field $\mathbf{B} = B\hat{\mathbf{y}}$ in y-direction, whose strength B is the parameter α to be measured. We let spins precess in the magnetic field, and, by incorporating small kicks about the x-axis, we find an improvement over the reference (without kicks) in terms of rescaled QFI and the precision based on the measurement of the electron-spin component S_z orthogonal to the magnetic field. The best possible measurement precision ΔB in units of $T/\sqrt{Hz}$ per 1 cm^3 vapor volume is $\Delta B = 1/\sqrt{n I_B^{(t)}}$ where $n \simeq 2 \times 10^{10}$ is the number of cesium atoms in 1 cm^3. For a specific measurement, $I_B^{(t)}$ must be replaced by the corresponding rescaled Fisher information $I_{\text{Fisher},B}^{(t)}$. We compare the models with and without kicks directly on the basis of the Fisher information rather than modeling in addition the specific optical implementation and the corresponding noise of the measurement of S_z. Neglecting this additional read-out-specific noise leads to slightly better precision bounds than given in the literature, but does not distort the comparison.

The magnetic field was set to $B = 4 \times 10^{-14}$ T in y-direction, such that the condition for the SERF regime is fulfilled, i.e., the Larmor frequency is much smaller than the spin-exchange rate, and the period is set to $\tau = 1$ ms. Since kicks induce decoherence in the atomic spin system, we have to choose a very small effective kicking strength of $k \simeq 6.5 \times 10^{-4}$ for the kicks around the x-axis (with respect to the $f = 3$ ground-state manifold), generated with an off-resonant 2 μs light pulse with intensity $I_{\text{kick}} = 0.1$ mW/cm^2 linearly polarized in x-direction, to find an advantage over the reference.
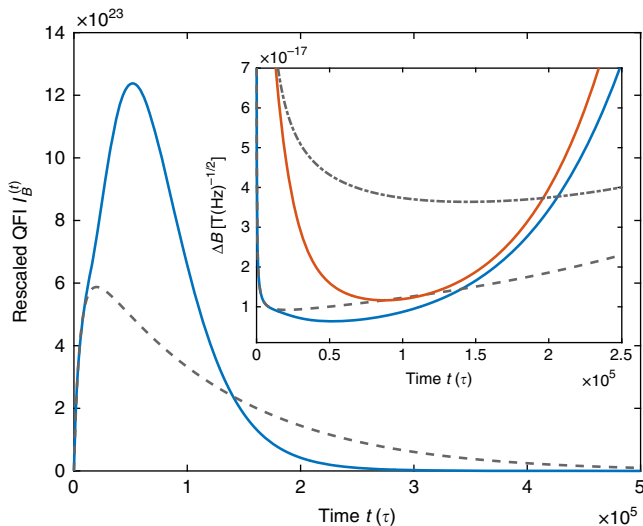
Fig. 9 Performance of a magnetic-field measurement with a kicked atomic-vapor magnetometer. While the gray dashed line shows the rescaled quantum Fisher information $I_B^{(t)}$ for measuring the magnetic field B with an spin-exchange-relaxation-free magnetometer, the blue line is obtained by adding a short optical kick at the end of each period τ. The inset shows precision ΔB in units of T per $\sqrt{\text{Hz}}$ for an optimal measurement (gray dashed line and blue line without and with kicks, respectively) and for measuring the z-component of the electronic spin S_z (gray dash-dotted and red line without and with kicks, respectively)

The example of Fig. 9 shows about 31% improvement in measurement precision ΔB for an optimal measurement (QFI, upper right inset) and 68% improvement in a comparison of S_z measurements (inset), which is impressive in view of the small system size. The achievable measurement precision of the kicked dynamics exhibits an improved robostness to decoherence: rescaled QFI for the kicked dynamics continues to increase and sets itself apart from the reference around the coherence time associated with spin-destruction relaxation. The laser light for these pulses can be provided by the laser used for the read out, which is typically performed with an off-resonant laser. A further improvement in precision is expected from additionally measuring kick pulses for readout or by applying kicks not only to the $f = 3$ but also to the $f = 4$ ground-state manifold of ^{133}Cs. Further, it might be possible to dramatically increase the relevant spin-size by applying the kicks to the joint spin of the cesium atoms, for instance, through a double-pass Faraday effect[55].

Discussion

Rendering the dynamics of quantum sensors chaotic allows one to harvest a quantum enhancement for quantum metrology without having to rely on the preparation or stabilization of highly entangled states. Our results imply that existing magnetic field sensors[31,56] based on the precession of a spin can be rendered more sensitive by disrupting the time-evolution by non-linear kicks. The enhancement persists in rather broad parameter regimes even when including the effects of dissipation and decoherence. Besides a thorough investigation of superradiance damping over large ranges of parameters, we studied a cesium-vapor-based atomic magnetomter in the SERF regime based on a detailed and realistic model[28–31,53]. Although the implementation of the non-linearity via a rank-2 light shift introduces additional decoherence and despite the rather small atomic spin size $f \leq 4$, a considerable improvement in measurement sensitivity is found (68% for a read-out scheme based on the measurement of the electronic spin-component S_z). The required non-linearity that

can be modulated as function of time has been demonstrated experimentally in ref. [38] in cold cesium vapor.

Even higher gains in sensitivity are to be expected if an effective interaction can be created between the atoms, as this opens access to larger values of total spin size for the kicks. This may be achieved e.g., via a cavity as suggested for pseudo-spins in ref. [57], or the interaction with a propagating light field as demonstrated experimentally in refs. [55,58] with about 10^{12} cesium atoms. More generally, our scheme will profit from the accumulated knowledge of spin-squeezing, which is also based on the creation of an effective interaction between atoms. Finally, we expect that improved precision can be found in other quantum sensors that can be rendered chaotic as well, as the underlying sensitivity to change of parameters is a basic property of quantum-chaotic systems.

Methods

QFI for kicked time-evolution of a pure state. The QFI in the chaotic regime with large system dimension $2J$ and times larger than the Ehrenfest time, $t > t_E$, is given in linear-response theory by an auto-correlation function $C(t) \equiv \langle \tilde{V}(t)\tilde{V}(0)\rangle - \langle \tilde{V}(t)\rangle\langle\tilde{V}(0)\rangle$ of the perturbation of the Hamiltonian in the interaction picture, $H_{\alpha+\epsilon}(t) = H_\alpha(t) + \epsilon V(t)$, $\tilde{V}(t) = U_\alpha(-t)V(t)U_\alpha(t)$:

$$I_\alpha(t) = 4\left(tC(0) + 2\sum_{t'=0}^{t-1}\left(t-t'\right)C(t')\right). \quad (15)$$

In our case, the perturbation $V(t) = J_z$ is proportional to the parameter-encoding precession Hamiltonian, and the first summand in Eq. (15) can be calculated for an initial coherent state,

$$C(0) = \frac{1}{3}j(j+1), \quad (16)$$

giving a tj^2-scaling starting from t_E. Due to the finite Hilbert-space dimension of the kicked top, the auto-correlation function decays for large times to a finite value $\overline{C}$, leading to a term quadratic in t from the sum in Eq. (15) that simplifies to $I_\alpha = 4\overline{C}t^2$ for $t \gg t_H$. If one rescales $J_z \rightarrow J_z/J$ such that it has a well defined classical limit, random matrix theory allows one to estimate the average value of $C(t)$ for large times: $\overline{C} = 2Js\sigma_{cl}$, and σ_{cl} is a transport coefficient that can be calculated numerically[16]. This yields Eq. (12).

Lyapunov exponent. A data point located at (Z, ϕ) for the Lyapunov exponent in Fig. 2c was obtained numerically by averaging over 100 initial conditions equally distributed within a circular area of size $1/j$ (corresponding to the coherent state) centered around (Z, ϕ).

References

1. Huelga, S. F. et al. Improvement of frequency standards with quantum entanglement. *Phys. Rev. Lett.* **79**, 3865–3868 (1997).
2. Meyer, V. et al. Experimental demonstration of entanglement-enhanced rotation angle estimation using trapped ions. *Phys. Rev. Lett.* **86**, 5870–5873 (2001).
3. Leibfried, D. et al. Toward Heisenberg-limited spectroscopy with multiparticle entangled states. *Science* **304**, 1476–1478 (2004).
4. Wasilewski, W. et al. Quantum noise limited and entanglement-assisted magnetometry. *Phys. Rev. Lett.* **104**, 133601 (2010).
5. Koschorreck, M., Napolitano, M., Dubost, B. & Mitchell, M. W. Sub-projection-noise sensitivity in broadband atomic magnetometry. *Phys. Rev. Lett.* **104**, 093602 (2010).
6. Goda, K. et al. A quantum-enhanced prototype gravitational-wave detector. *Nat. Phys.* **4**, 472–476 (2008).
7. Aasi, J. et al. Enhanced sensitivity of the LIGO gravitational wave detector by using squeezed states of light. *Nat. Photonics* **7**, 613–619 (2013).
8. Giovannetti, V., Lloyd, S. & Maccone, L. Quantum-enhanced positioning and clock synchronization. *Nature* **412**, 417–419 (2001).

9. Allen, E. H. & Karageorgis, M. Radar systems and methods using entangled quantum particles. US Patent 7,375,802 (2008).

10. Taylor, J. et al. High-sensitivity diamond magnetometer with nanoscale resolution. *Nat. Phys.* **4**, 810–816 (2008).

11. Boto, A. N. et al. Quantum interferometric optical lithography: exploiting entanglement to beat the diffraction limit. *Phys. Rev. Lett.* **85**, 2733–2736 (2000).

12. Higgins, B. L., Berry, D. W., Bartlett, S. D., Wiseman, H. M. & Pryde, G. J. Entanglement-free Heisenberg-limited phase estimation. *Nature* **450**, 393–396 (2007).

13. Nagata, T., Okamoto, R., O'Brien, J. L. & Takeuchi, K. S. S. Beating the standard quantum limit with four-entangled photons. *Science* **316**, 726–729 (2007).

14. Pezzè, L., Smerzi, A., Oberthaler, M. K., Schmied, R. & Treutlein, P. Quantum metrology with nonclassical states of atomic ensembles. Preprint at https://arxiv.org/abs/1609.01609v2 (2016).

15. Peres, A. in *Quantum Chaos* (eds Cerdeira, H. A., Ramaswamy, R., Gutzwiller, M. C., Casati, G.) (World Scientific, Singapore, 1991).

16. Gorin, T., Prosen, T., Seligman, T. H. & Žnidarič, M. Dynamics of Loschmidt echoes and fidelity decay. *Phys. Rep.* **435**, 33–156 (2006).

17. Boixo, S. et al. Quantum metrology: dynamics versus entanglement. *Phys. Rev. Lett.* **101**, 040403 (2008).

18. Xiao-Qian, W., Jian, M., Xi-He, Z. & Xiao-Guang, W. Chaos and quantum Fisher information in the quantum kicked top. *Chin. Phys. B* **20**, 050510 (2011).

19. Song, L., Ma, J., Yan, D. & Wang, X. Quantum Fisher information and chaos in the Dicke model. *Eur. Phys. J. D* **66**, 201 (2012).

20. Weiss, C. & Teichmann, N. Signatures of chaos-induced mesoscopic entanglement. *J. Phys. B* **42**, 031001 (2009).

21. Fröwis, F., Sekatski, P. & Dür, W. Detecting large quantum Fisher information with finite measurement precision. *Phys. Rev. Lett.* **116**, 090801 (2016).

22. Macrì, T., Smerzi, A. & Pezzè, L. Loschmidt echo for quantum metrology. *Phys. Rev. A* **94**, 010102 (2016).

23. Linnemann, D. et al. Quantum-enhanced sensing based on time reversal of nonlinear dynamics. *Phys. Rev. Lett.* **117**, 013001 (2016).

24. Ma, J., Wang, X., Sun, C. & Nori, F. Quantum spin squeezing. *Phys. Rep.* **509**, 89–165 (2011).

25. Madhok, V., Riofrío, C. A., Ghose, S. & Deutsch, I. H. Information gain in tomography–a quantum signature of chaos. *Phys. Rev. Lett.* **112**, 014102 (2014).

26. Madhok, V., Riofrío, C. A. & Deutsch, I. H. Review: characterizing and quantifying quantum chaos with quantum tomography. *Pramana* **87**, 65 (2016).

27. Braun, D. et al. Quantum enhanced measurements without entanglement. Preprint at https://arxiv.org/abs/1701.05152 (2017).

28. Allred, J., Lyman, R., Kornack, T. & Romalis, M. High-sensitivity atomic magnetometer unaffected by spin-exchange relaxation. *Phys. Rev. Lett.* **89**, 130801 (2002).

29. Kominis, I. K., Kornack, T. W., Allred, J. C. & Romalis, M. V. A subfemtotesla multichannel atomic magnetometer. *Nature* **422**, 596–599 (2003).

30. Savukov, I. & Romalis, M. Effects of spin-exchange collisions in a high-density alkali-metal vapor in low magnetic fields. *Phys. Rev. A* **71**, 023405 (2005).

31. Budker, D. & Romalis, M. Optical magnetometry. *Nat. Phys.* **3**, 227–234 (2007).

32. Sheng, D., Li, S., Dural, N. & Romalis, M. Subfemtotesla scalar atomic magnetometry using multipass cells. *Phys. Rev. Lett.* **110**, 160802 (2013).

33. Appelt, S. et al. Theory of spin-exchange optical pumping of ^{3}He and ^{129}Xe. *Phys. Rev. A* **58**, 1412–1439 (1998).

34. Haake, F., Kuś, M. & Scharf, R. Classical and quantum chaos for a kicked top. *Z. Phys. B Condens. Matter* **65**, 381–395 (1987).

35. Haake, F., Kuś, M. & Scharf, R. in *Coherence, Cooperation, and Fluctuations* (eds Haake, F., Narducci, L., Walls, D.) (Cambridge University Press, Cambridge, 1986).

36. Haake, F. *Quantum Signatures of Chaos*, Vol. 54 (Springer Science & Business Media, Berlin, 2013).

37. Haake, F. Can the kicked top be realized? *J. Mod. Opt.* **47**, 2883–2890 (2000).

38. Chaudhury, S., Smith, A., Anderson, B., Ghose, S. & Jessen, P. S. Quantum signatures of chaos in a kicked top. *Nature* **461**, 768–771 (2009).

39. Helstrom, C. W. Quantum detection and estimation theory. *J. Stat. Phys.* **1**, 231–252 (1969).

40. Miszczak, J. A., Puchała, Z., Horodecki, P., Uhlmann, A. & Życzkowski, K. Sub- and super-fidelity as bounds for quantum fidelity. *Quantum Inf. Comput.* **9**, 0103–0130 (2009).

41. Braunstein, S. L. & Caves, C. M. Statistical distance and the geometry of quantum states. *Phys. Rev. Lett.* **72**, 3439–3443 (1994).

42. Braunstein, S. L. & Caves, C. M. Wringing out better Bell inequalities. *Ann. Phys.* **202**, 22–56 (1990).

43. Zaslavsky, G. M. Stochasticity in quantum systems. *Phys. Rep.* **80**, 157–250 (1981).

44. Jacquod, P., Silvestrov, P. & Beenakker, C. Golden rule decay versus Lyapunov decay of the quantum Loschmidt echo. *Phys. Rev. E* **64**, 055203 (2001).

45. Benenti, G. & Casati, G. Quantum-classical correspondence in perturbed chaotic systems. *Phys. Rev. E* **65**, 066205 (2002).

46. Sankaranarayanan, R. & Lakshminarayan, A. Recurrence of fidelity in nearly integrable systems. *Phys. Rev. E* **68**, 036216 (2003).

47. Dicke, R. H. Coherence in spontaneous radiation processes. *Phys. Rev.* **93**, 99–110 (1954).

48. Bonifacio, R., Schwendiman, P. & Haake, F. Quantum statistical theory of superradiance I. *Phys. Rev. A.* **4**, 302–313 (1971).

49. Haake, F. *Statistical Treatment of Open Systems by Generalized Master Equations, Springer Tracts in Modern Physics*, Vol. 66, 98-168 (Springer, Berlin, 1973).

50. Gross, M. & Haroche, S. Superradiance: an essay on the theory of collective spontaneous emission. *Phys. Rep.* **93**, 301–396 (1982).

51. Kaluzny, Y., Goy, P., Gross, M., Raimond, J. & Haroche, S. Observation of self-induced Rabi oscillations in two-level atoms excited inside a resonant cavity: the ringing regime of superradiance. *Phys. Rev. Lett.* **51**, 1175–1178 (1983).

52. Braun, D. *Dissipative Quantum Chaos and Decoherence, Springer Tracts in Modern Physics*, Vol. 172 (Springer, Berlin, 2001).

53. Balabas, M., Karaulanov, T., Ledbetter, M. & Budker, D. Polarized alkali-metal vapor with minute-long transverse spin-relaxation time. *Phys. Rev. Lett.* **105**, 070801 (2010).

54. Deutsch, I. H. & Jessen, P. S. Quantum control and measurement of atomic spins in polarization spectroscopy. *Opt. Commun.* **283**, 681–694 (2010).

55. Takeuchi, M. et al. Spin squeezing via one-axis twisting with coherent light. *Phys. Rev. Lett.* **94**, 023003 (2005).

56. Ledbetter, M., Savukov, I., Acosta, V., Budker, D. & Romalis, M. Spin-exchange-relaxation-free magnetometry with Cs vapor. *Phys. Rev. A* **77**, 033408 (2008).

57. Agarwal, G., Puri, R. & Singh, R. Atomic Schrödinger cat states. *Phys. Rev. A* **56**, 2249–2254 (1997).

58. Julsgaard, B., Kozhekin, A. & Polzik, E. S. Experimental long-lived entanglement of two macroscopic objects. *Nature* **413**, 400–403 (2001).

Acknowledgements

Author contributions

D.B. initiated the idea and L.F. made the calculations and numerical simulations. Both authors contributed to the interpretation of data and the writing of the manuscript.

Additional information

Supplementary Information accompanies this paper at https://doi.org/10.1038/s41467-018-03623-z.

Competing interests: The authors declare no competing interests.

Reprints and permission information is available online at http://npg.nature.com/reprintsandpermissions/

Publisher's note: Springer Nature remains neutral with regard to jurisdictional claims in published maps and institutional affiliations.

Quantum metrology with quantum-chaotic sensors

Fiderer et al.

Supplementary Information

Supplementary Note 1. Realization of the kicked top

The kicked top (KT) has been realized experimentally by Chaudhury et al. [1] using the atomic spin of a ^{133}Cs atom in the $f = 3$ hyperfine ground state. Linear precession of the spin was implemented through magnetic pulses, and the torsion through an off-resonant laser field that exploited a spin-dependent rank-2 (ac Stark) light shift.

An implementation of the KT using microwave superradiance was proposed by Haake [2]: The top is represented by the collective pseudo-spin of N two-level atoms coupled with the same coupling constant to a single mode of an electromagnetic field in a cavity, with a controlled detuning between mode and atomic frequencies. Large detuning compared to the Rabi frequency $\Omega = g\sqrt{N}$ with coupling strength g allows one to adiabatically eliminate the cavity mode and leads to an effective interaction of the type J_z^2 [3] (replacing our J_y^2), while superradiant damping as described by the master equation (13) in the main text for the reduced density operator of the atoms can still prevail [2]. Finally, a linear rotation about the x-axis can be achieved through resonant microwave pulses, replacing the linear precession about the z-axis of the KT. The parameter α is now proportional to the Rabi frequency of the microwave pulse.

Supplementary Note 2. Spin-exchange-relaxation-free Cs-vapor magnetometer

Adapting standard notation in atomic physics, atomic spin operators will be denoted in the following by $\mathbf{F} = (F_x, F_y, F_z)$ with spin size f, $F_z|fm\rangle = m|fm\rangle$, and total electronic angular momentum $\mathbf{J} = \mathbf{L} + \mathbf{S}$ with quantum number j, composed of orbital angular momentum $\mathbf{L}$ and electron spin $\mathbf{S}$. We model a room-temperature spin-exchange-relaxation-free (SERF) Cs-vapor magnetometer similar to the experiments with Rb-vapor of Balabas et al. [4]. The Cs spin sensitive to the magnetic field B is composed of a nuclear spin $K = 7/2$ and one valence electron with an electronic spin $s = 1/2$ which splits the ground state $6^2\mathrm{S}_{1/2}$ into two energy levels with total spin $f_1 = 3$ and $f_2 = 4$. This results in an effective Hilbert space of dimension $2(2K + 1) = 16$ for our model of a kicked SERF magnetometer.

The dominant damping mechanisms are related to collisions of cesium atoms with each

other and with the walls of the vapor cell.

In the SERF regime the spin-exchange rate is much greater than the rate of Larmor precession, typically realized by very small magnetic fields, a high alkali-atom density (10^{13} atoms per cm^3), high buffer-gas pressure, and heating of the vapor cell. Then, spin-exchange relaxation is so strong, that the population of hyperfine ground levels ($f_i = 3, 4$) is well described by a spin-temperature distribution. Here, we model a SERF magnetmeter with a lower alkali-atom density of 2×10^{10} atoms per cm^3 without buffer gas at room temperature $T = 294.13$ K. Modern alkene-based vapor-cell coatings support up to 10^6 collisions before atoms become depolarized [4]. For a spherical vapor-cell with a 1.5 cm radius it follows that collisions with walls limit the lifetime of spin polarization to $T_{\text{wall}} \simeq 92$ s. Since the effect of collisions among Cs atoms leads to stronger depolarization we neglect collisions with the walls in our model.

While the typical treatment proceeds by eliminating the nuclear-spin component we are interested in a dynamics that exploits the larger Hilbert space of the Cs spin. Therefore the evolution of the spin density matrix ρ is described by a master equation that includes damping originating from collisions of Cs atoms [5] and an interaction with an off-resonant light field in the low-saturation limit [6] modeling the kicks:

$$\frac{d\rho}{dt} = R_{\text{se}}\left[\varphi(1 + 4\langle\mathbf{S}\rangle \cdot \mathbf{S}) - \rho\right] + R_{\text{sd}}\left[\varphi - \rho\right] + a_{\text{hf}}\frac{[\mathbf{K}\cdot\mathbf{S}, \rho]}{i\hbar} + \frac{H_{\text{A}}^{\text{eff}}\rho - \rho H_{\text{A}}^{\text{eff}\dagger}}{i\hbar}$$
$$+ \gamma_{\text{nat}} \sum_{q=-1}^{1}\left(\sum_{f,f_1} W_q^{ff_1} \rho_{f_1 f_1}\left(W_q^{ff_1}\right)^\dagger + \sum_{f_1 \neq f_2} W_q^{f_2 f_2} \rho_{f_2 f_1}\left(W_q^{f_1 f_1}\right)^\dagger\right) \tag{1}$$

The first two summands describe spin-exchange relaxation and spin-destruction relaxation, respectively, where R_{se} denotes the spin-exchange rate and R_{sd} the spin-destruction rate, and $\varphi = \rho/4 + \mathbf{S}\cdot\rho\mathbf{S}$ is called the purely nuclear part of the density matrix, where the electron-spin operator $\mathbf{S}$ only acts on the electron-spin component with expectation value $\langle\mathbf{S}\rangle = \text{tr}[\mathbf{S}\rho]$. The third summand is the hyperfine coupling of nuclear spin $\mathbf{K}$ and electronic spin $\mathbf{S}$ with hyperfine structure constant a_{hf}, and the fourth summand drives the dynamic with an effective non-hermitian Hamiltonian on both ground-state hyperfine manifolds $H_{\text{A}}^{\text{eff}} = H_{\text{A},f=3}^{\text{eff}} + H_{\text{A},f=4}^{\text{eff}}$, with

$$H_{\text{A},f}^{\text{eff}} = \hbar\Omega_{\text{Lar}}F_y + \sum_{f'} \frac{\hbar\Omega^2 C_{j'f'f}^{(2)}}{4(\Delta_{ff'} + i\gamma_{\text{nat}}/2)}\left|\boldsymbol{\epsilon}_{\text{L}}\cdot\mathbf{F}\right|^2 \tag{2}$$

that includes Larmor precession with frequency $\Omega_{\text{Lar}} = g_f\mu_{\text{B}}B/\hbar$ (with the Landé g-factor g_f

3

and the Bohr magneton μ_B) of the atomic spin in the external magnetic field $\mathbf{B} = B\hat{\mathbf{y}}$, and the rank-2 light-shift induced by a light pulse that is linearly polarized with unit polarization vector $\boldsymbol{\epsilon}_L$ of the light field and off-resonant with detuning $\Delta_{ff'}$ from the D1-line transition with $f \to f'$. Further, we have the characteristic Rabi frequency $\Omega = \gamma_{\text{nat}}\sqrt{I_{\text{kick}}/(2I_{\text{sat}})}$ of the D1 line, the natural line width γ_{nat}, kick-laser intensity I_{kick}, saturation intensity I_{sat}, and the coefficient

$$C^{(2)}_{j'f'f} = (-1)^{3f-f'} \frac{\sqrt{30}(2f'+1)}{\sqrt{f(f+1)(2f+1)(2f-1)(2f+3)}} \begin{Bmatrix} f & 1 & f' \\ 1 & f & 2 \end{Bmatrix} \left| o^{j'f'}_{1/2f} \right|^2, \qquad (3)$$

where the curly braces denote the Wigner $6j$ symbol and

$$o^{j'f'}_{jf} = (-1)^{f'+1+j'+K} \sqrt{(2j'+1)(2f+1)} \begin{Bmatrix} f & K & j' \\ j & 1 & f \end{Bmatrix}, \qquad (4)$$

where total angular momentum of ground and excited levels of the D1 line are $j = j' = 1/2$. Photon scattering is taken into account by the imaginary shift of $\Delta_{ff'}$ in the effective Hamiltonian and by the remaining parts of the master equation that correspond to optical pumping which leads to cycles of excitation to the $6P_{1/2}$ manifold and spontaneous emission to the ground-electronic manifold $6S_{1/2}$. When the laser is switched off the master equation solely involves the first four summands where H^{eff}_A reduces to the Larmor precession term.

The jump operators are given as

$$W^{f_b f_a}_q = \sum_{f'=3}^{4} \frac{\Omega/2}{\Delta_{f_a f'} + i\gamma_{\text{nat}}/2} \left(\mathbf{e}^*_q \cdot \mathbf{D}_{f_b f'}\right) \left(\boldsymbol{\epsilon}_L \cdot \mathbf{D}^\dagger_{f_a f'}\right), \qquad (5)$$

with the spherical basis $\mathbf{e}_1 = -(\hat{\mathbf{x}} + i\hat{\mathbf{y}})/\sqrt{2}$, $\mathbf{e}_0 = \hat{\mathbf{z}}$, $\mathbf{e}_{-1} = (\hat{\mathbf{x}} - i\hat{\mathbf{y}})/\sqrt{2}$ in the Cartesian basis $\hat{\mathbf{x}}, \hat{\mathbf{y}}, \hat{\mathbf{z}}$, and the raising operator $\mathbf{D}^\dagger_{ff'} = \sum_{q,m,m'} \mathbf{e}^*_q o^{j'f'}_{jf} \langle f'm'|fm;1q\rangle |f'm'\rangle\langle fm|$ with Clebsch-Gordan coefficients $\langle f'm'|fm;1q\rangle$ and magnetic quantum numbers m, m'.

Excited state hyperfine levels are Doppler and pressure broadened, but we neglect pressure broadening which is much smaller than Doppler broadening due to the very low vapor pressure. Doppler broadening is taken into account by numerically averaging the righthand side of the master equation (Supplementary Equation 1) over the Maxwell-Boltzmann distribution of velocities of an alkali atom. This translates into an average over detunings $\Delta_{ff'}$. Since $\Delta \gg \Omega$ must hold within the description of this master equation, we limit averaging over detunings to a 3σ interval.

By numerically solving the non-linear trace-preserving master equation (Supplementary Equation 1) with the Euler method (analog to Ref. [7] we take hyperfine coupling into account by setting off-diagonal blocks of the density matrix in the coupled $|fm\rangle$-basis after each Euler step to zero, because they oscillate very quickly with a_{hf}), we simulate dynamics similar to the dissipative kicked top described above with the difference that kicks are not assumed to be arbitrarily short, i.e. kicks and precession coexist during a light pulse. Kicks and corresponding dissipation are factored in by applying a superoperator to the state in each Euler step during a kick.

Spin-exchange and spin-destruction rates are estimated to $R_{\mathrm{se}} \simeq 12\,\mathrm{Hz}$ and $R_{\mathrm{sd}} \simeq 0.12\,\mathrm{Hz}$ from the known cross sections of Cs-Cs collisions, the mean relative thermal velocity of Cs atoms and their density.

For the concrete example of Fig. 7 we calculate with 2×10^{10} Cs atoms per $1\,\mathrm{cm}^3$ vapor volume, and kick laser pulses linearly polarized in x-direction, $\boldsymbol{\epsilon}_{\mathrm{L}} = \hat{\mathbf{x}}$, with intensity $I_{\mathrm{kick}} = 0.1\,\mathrm{mW/cm}^2$ and detuning halfway between the two components of the D1 line, and $\Delta_{34} \simeq -584\,\mathrm{MHz}$. The period is $\tau = 1\,\mathrm{ms}$ where during the last $2\,\mu\mathrm{s}$ of each period the laser pulse is applied (effective kicking strength for the lower hyperfine level of the ground state is $k \simeq 6.5 \times 10^{-4}$). We choose a small magnetic field $B = 40\,\mathrm{fT}$ in y-direction so that we are well within the SERF regime, $R_{\mathrm{se}} \gg \Omega_{\mathrm{Lar}}$.

With a circular polarized pump beam in z-direction resonant with the D1 line the initial spin-state is polarized which in the presence of spin-relaxation leads to an effective thermal state

$$\rho = \frac{e^{\beta K_z} e^{\beta S_z}}{Z_K Z_S},\tag{6}$$

with the partition sum $Z_j = \sum_{m=-j}^{j} e^{\beta m}$ and $\beta = \ln\frac{1+q}{1-q}$, with polarization $q = 0.95$. The readout is accomplished typically with the help of an off-resonant probe beam by measuring its polarization after it experienced a Faraday rotation when interacting with the atomic spin ensemble.

Supplementary References

[1] Chaudhury, S., Smith, A., Anderson, B., Ghose, S. & Jessen, P. S. Quantum signatures of chaos in a kicked top. *Nature* **461**, 768–771 (2009).

[2] Haake, F. Can the kicked top be realized? *Journal of Modern Optics* **47**, 2883–2890 (2000).

[3] Agarwal, G., Puri, R. & Singh, R. Atomic Schrödinger cat states. *Phys. Rev. A* **56**, 2249–2254 (1997).

[4] Balabas, M., Karaulanov, T., Ledbetter, M. & Budker, D. Polarized Alkali-Metal Vapor with Minute-Long Transverse Spin-Relaxation Time. *Phys. Rev. Lett.* **105**, 070801 (2010).

[5] Appelt, S. *et al.* Theory of spin-exchange optical pumping of ^{3}He and ^{129}Xe. *Phys. Rev. A* **58**, 1412–1439 (1998).

[6] Deutsch, I. H. & Jessen, P. S. Quantum control and measurement of atomic spins in polarization spectroscopy. *Optics Communications* **283**, 681–694 (2010).

[7] Savukov, I. & Romalis, M. Effects of spin-exchange collisions in a high-density alkali-metal vapor in low magnetic fields. *Phys. Rev. A* **71**, 023405 (2005).

A quantum-chaotic cesium-vapor magnetometer

Lukas J. Fiderer[a] and Daniel Braun[a]

[a]Institute for Theoretical Physics, University of Tübingen, Auf der Morgenstelle 14, 72076 Tübingen, Germany

ABSTRACT

Quantum-enhanced measurements represent the path towards the best measurement precision allowed by the laws of quantum mechanics. Known protocols usually rely on the preparation of entangled states and promise high or even optimal precision, but fall short in real-word applications because of the difficulty to generate entangled states and to protect them against decoherence. Here, we refrain from the preparation of entangled states but supplement the integrable parameter-encoding dynamics by non-linear kicks driving the system in the dynamical regime of quantum chaos. We show that large improvements in measurement precision are possible by modeling a spin-exchange relaxation-free alkali-vapor magnetometer where the non-linear kicks are realized by exploiting the ac Stark effect.

Keywords: magnetometer, atomic vapor, cesium, SERF, quantum chaos, kicked top, quantum Fisher information, non-linear, decoherence, master equation

1. INTRODUCTION

High-precision sensors are based more and more often on quantum systems such as NV centers,[1] photons in an interferometer,[2] or clouds of atoms.[3] Optimizing such sensors allows measurement precision to reach the standard quantum limit. To overcome this limit, it is necessary to exploit genuine quantum properties such as entanglement of the quantum systems under consideration. Such quantum-enhanced measurements were proposed to improve frequency standards,[4–8] navigation,[9] remote sensing,[10] measurement of magnetic fields,[11] or gravitational wave detection.[12, 13]

Common features of many propositions are the preparation of non-classical, entangled states and integrable dynamics of the quantum sensor.[14] Although the preparation of entangled states is a theoretically well-established resource that in principle allows one to reach optimal measurement precision, in practice, it represents a huge challenge to generate entanglement over large systems that is necessary to achieve large improvements in measurement precisions. Further, entangled states are prone to decoherence which leads, for instance, to a severe decrease of squeezing in interferometers that operate with squeezed vacuum. In particular, it has been shown that in most cases decoherence prevents reaching the desirable Heisenberg scaling of precision such that the quantum improvement reduces to a constant factor over the standard quantum limit.[15, 16]

Decoherence in quantum systems and experimental difficulties in generating entanglement call for quantum-enhanced protocols that perform well under decoherence without requiring the preparation of large-scale entanglement. The idea, we proposed in our work about quantum-chaotic sensors,[17] is the following: Prepare the quantum sensor in a coherent state, i.e., the most classical state, that is typically easy to prepare. Then, the dynamics that encodes the parameter to be measured is supplemented with non-linear kicks, corresponding to some non-linear Hamiltonian that does not commute with the Hamiltonian of the parameter-encoding dynamics. This can create quantum chaos, i.e., dynamics that becomes chaotic in the classical limit. The unpredictability of classical chaos originating from its exponential sensitivity to a change of initial conditions is absent in the quantum case; instead quantum chaos is characterized by its sensitivity to a change of the dynamics which can be quantified by the Loschmidt echo. The Loschmidt echo, however, is in the limit of small changes of the dynamics related to the quantum Fisher information which quantifies the achievable measurement precision

Send correspondence to L.J.F. or D.B.

L.J.F.: E-mail: lukas.fiderer@uni-tuebingen.de

D.B.: E-mail: daniel.braun@uni-tuebingen.de

(a more precise description is given in section 4.1), hinting at an underlying connection of quantum chaos and achievable measurement precision. At the example of the kicked top model, this correspondence has been studied numerically in the decoherence-free regime as well as under decoherence.[17]

Here we simulate a spin-exchange relaxation-free cesium-vapor magnetometer that is turned into a quantum-chaotic sensor by periodically applying nonlinear, short kicks to the cesium spins that precess in the magnetic field which has to be measured. Comparing the measurement performance with the same sensor in the absence of kicks, we find an improvement in measurement precision.

In section 2, we introduce the kicked top model, a standard model to study quantum chaos. In section 3, it is discussed how to turn an alkali-vapor magnetometer into a quantum-chaotic sensor based on the kicked top model. The master equation for such a quantum-chaotic magnetometer is given in section 3.2. Finally, in section 4, we introduce the framework of quantum Fisher information which is then used to quantify and compare the measurement precision of the quantum-chaotic magnetometer.

2. THE KICKED TOP MODEL

Consider an atomic spin of size f with spin operator $\mathbf{F} = (F_x, F_y, F_z)$, $F_z|fm\rangle = \hbar m|fm\rangle$ and $\mathbf{F}^2|fm\rangle = \hbar^2 f(f+1)|fm\rangle$, where f and m are atomic angular momentum quantum numbers. For such an atomic spin, or actually for any quantum system fulfilling the angular momentum algebra, we can set up the kicked top model[18–20] with time-dependent Hamiltonian

$$H_{\mathrm{KT}}(t) = \alpha F_y + \frac{k}{(2f+1)\hbar}F_x^2 \sum_{n=-\infty}^{\infty} \tau\delta(t-n\tau)\,. \tag{1}$$

Setting the period $\tau = 1$, the Floquet operator

$$U_\alpha(k) = e^{-ik\frac{F_x^2}{(2f+1)\hbar^2}} e^{-i\alpha\frac{F_y}{\hbar}} \tag{2}$$

describes the unitary dynamics from time t to $t+\tau$. The first term αF_y of the Hamiltonian generates a rotation or precession of the angular momentum around the y-axis by an angle α. The second term contains the non-linearity F_x^2 generating an instantaneous kick only if time t equals $n\tau$ where n can be any integer. k is the kicking strength. In total, the dynamics consist of continuous spin precession periodically disrupted by instantaneous nonlinear kicks. Figure 1 (c) shows the kicked top dynamics integrated in a measurement protocol measuring the precession angle α.

The kicked top is a standard model in quantum chaos because its dynamics is non-integrable for $k \geq 0$ and its classical limit shows a transition from regular to chaotic dynamics when k is increased. The kicked top has been realized with single-atom spins in a cold gas[21] as well as with a pair of spin-1/2 nuclei using NMR techniques.[22]

3. A KICKED CESIUM-VAPOR MAGNETOMETER

Alkali-vapor magnetometers in the spin-exchange relaxation-free (SERF) regime[23–27] typically consist of a glass cell filled with the alkali vapor with a density of about 10^{13} atoms per cm^3. The optically polarized spins of the alkali atoms are the quantum system of the magnetometer that reacts to a magnetic field with precession around the axis of orientation of the magnetic field. The dominant damping mechanisms originate from collisions of alkali atoms among each other and with the walls of the glass cell. Therefore, buffer gas is added to the cell and the inside walls are coated with an anti-relaxation coating. The SERF regime is determined by a spin-exchange rate that is much higher than the Larmor precession of the spins induced by the magnetic field to be measured; it is realized by small magnetic fields (10^{-13} T), high gas pressure in the cell, and heating of the atomic vapor.
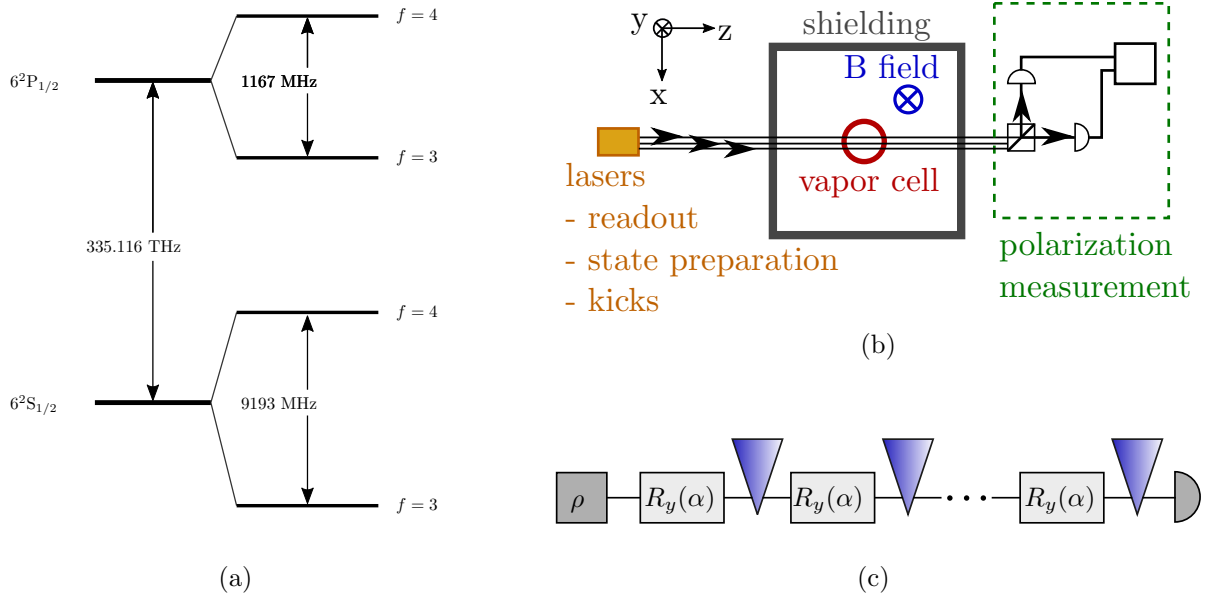
Figure 1: Panel (a): Hyperfine structure of the D1 line of ^{133}Cs (not to scale). Panel (b): Schematic setup of a kicked cesium-vapor magnetometer. State preparation consists of polarizing the atomic spins optically; non-linear kicks and readout are realized optically as well, where a polarization measurement is performed for the transmitted readout beam. Panel (c): Schematic procedure of a quantum chaotic measurement. A state ρ is prepared, precession $R_y(\alpha)$ encodes the parameter α to the system, non-linear kicks (blue wedges) are applied periodically, and final readout (semicircle) allows to estimate α.

3.1 Finding a proper parameter regime

In the following, we show how to implement the kicked top model in an alkali-vapor magnetometer in the spin-exchange relaxation-free (SERF) regime.[23–27] We model a cesium-vapor magnetometer at room temperature similar to the experiments with rubidium vapor of Balabas et al.[28]

The Cs spin is composed of a nuclear spin $K = 7/2$ and an electronic spin $s = 1/2$ of a single valence electron which splits the ground state $6^2S_{1/2}$ into two energy levels with total spin $f_1 = 3$ and $f_2 = 4$. This results in an effective Hilbert space of dimension $2(2K+1) = 16$ for our model of a kicked SERF magnetometer. Consider the D1 line of ^{133}Cs as depicted in figure 1 (a). The kicks will be realized exploiting the ac Stark effect, a rank-2 light shift generated by linearly-polarized, off-resonant light pulse. More precisely, with respect to the $6^2S_{1/2}$, $f_1 = 3$ ground state, the light pulse is tuned halfway between the two hyperfine components of $6^2P_{1/2}$ because the light shift is strongest there.[29,30] The ac Stark effect is present only if the hyperfine splitting of $6^2P_{1/2}$ is resolved which is *not* the case under conditions typical for SERF magnetometers due to pressure broadening. Therefore, we choose a density of only 2×10^{10} cesium atoms per cm^3 and no buffer gas. It was shown by Balabas et al.[28] that thanks to an alkene-based anti-relaxation coating of the walls of the glass cell it is still possible to reach the SERF regime. Then, pressure broadening is negligible compared to 357 MHz (FWHM) of Doppler broadening of the hyperfine levels of $6^2P_{1/2}$, which is obtained from the temperature (294 K, room temperature) and the mass of a cesium atom. Then, the relatively large hyperfine splitting of cesium (1167 MHz, figure 1 (a)) is large enough to be well resolved. Note that heating of the glass cell is counterproductive as it increases Doppler broadening.

This represents a parameter regime where magnetic precession of the cesium spins corresponds to the linear precession Hamiltonian in the kicked top model, and short off-resonant light pulses induce the ac Stark effect corresponding to the non-linear kicks. In the next section we give a master equation taking into account all relevant decoherence mechanisms including decoherence due to the off-resonant light pulses as well as the finite length of the light pulses in contrast to the idealized delta-shaped kicks of the kicked top model.

3.2 Master equation

Collisions of cesium atoms lead to spin-exchange and spin-destruction processes with rates $R_{se} \simeq 12\,\text{Hz}$ and $R_{sd} \simeq 0.12\,\text{Hz}$, respectively. These decay rates can be estimated from the cross sections of Cs-Cs collisions,[31] the mean relative thermal velocity of cesium atoms and their density.[32] The Larmor frequency is given by $\Omega_{\text{Lar}} = g_f \mu_B B / \hbar$ with the Landé g-factor g_f and the Bohr magneton μ_B, and we set the magnetic field strength to $B = 4 \times 10^{-14}$. In the electronic ground state $6^2 S_{1/2}$, we have $\Omega_{\text{Lar}} \simeq 0.44\,\text{mHz}$ such that $R_{se} \gg \Omega_{\text{Lar}}$, i.e., we are in the SERF regime. Then, the effective, joint dynamics of both hyperfine ground states of $6^2 S_{1/2}$ is unaffected by spin-exchange collisions. The alkene-based anti-relaxation coating from Balabas et al.[28] supports up to 10^6 collisions before the atomic spins become depolarized. For a spherical vapor-cell with $3\,\text{cm}$ diameter, this leads to a damping rate due to collisions with the wall of $R_{\text{wall}} \simeq 11\,\text{mHz}$. Since $R_{sd} \gg R_{\text{wall}}$, spin destruction is the dominant damping mechanism, and we neglect damping due to collisions with the wall.

In order to model non-integrable dynamics, the theoretical description must take into account the full Hilbert space of the electronic ground state in contrast to the standard modeling of SERF magnetometers where the nuclear-spin component is eliminated. We use the following notation: the atomic spin $\mathbf{F} = \mathbf{K} + \mathbf{J}$ can be decomposed in nuclear spin $\mathbf{K}$ and electronic angular momentum $\mathbf{J} = \mathbf{L} + \mathbf{S}$, where $\mathbf{L}$ is the orbital angular momentum and $\mathbf{S}$ the electron spin. The evolution of the spin density matrix ρ is described by a master equation that includes damping originating from collisions of cesium atoms[33] and an interaction with an off-resonant light field in the low-saturation limit[29] modeling the non-linear kicks:

$$\frac{d\rho}{dt} = R_{se}\left[\varphi(1 + 4\langle\mathbf{S}\rangle \cdot \mathbf{S}) - \rho\right] + R_{sd}\left[\varphi - \rho\right] + a_{\text{hf}}\frac{[\mathbf{K}\cdot\mathbf{S},\rho]}{i\hbar} + \frac{H_{\text{A}}^{\text{eff}}\rho - \rho H_{\text{A}}^{\text{eff}\dagger}}{i\hbar}$$
$$+ \gamma_{\text{nat}}\sum_{q=-1}^{1}\left(\sum_{f,f_1}W_q^{ff_1}\rho_{f_1f_1}\left(W_q^{ff_1}\right)^{\dagger} + \sum_{f_1\neq f_2}W_q^{f_2f_2}\rho_{f_2f_1}\left(W_q^{f_1f_1}\right)^{\dagger}\right). \tag{3}$$

The first summand describes spin-exchange relaxation, and $\varphi = \rho/4 + \mathbf{S}\cdot\rho\mathbf{S}$ is called the purely nuclear part of the density matrix, where the electron-spin operator $\mathbf{S}$ only acts on the electron-spin component with expectation value $\langle\mathbf{S}\rangle = \text{tr}[\mathbf{S}\rho]$. Spin-destruction relaxation is given by the second summand. The third summand describes the hyperfine coupling of nuclear spin $\mathbf{K}$ and electronic spin $\mathbf{S}$ with hyperfine structure constant a_{hf}, and the fourth summand drives the dynamics with an effective non-hermitian Hamiltonian on both ground-state hyperfine manifolds $H_{\text{A}}^{\text{eff}} = H_{\text{A},f=3}^{\text{eff}} + H_{\text{A},f=4}^{\text{eff}}$, with

$$H_{\text{A},f}^{\text{eff}} = \hbar\Omega_{\text{Lar}}F_y + \sum_{f'}\frac{\hbar\Omega^2 C_{j'f'f}^{(2)}}{4(\Delta_{ff'} + i\gamma_{\text{nat}}/2)}\left(\boldsymbol{\epsilon}_{\text{L}}\cdot\mathbf{F}\right)^2. \tag{4}$$

The effective Hamiltonian includes Larmor precession with frequency Ω_{Lar} of the atomic spin in the external magnetic field $\mathbf{B} = B\hat{\mathbf{y}}$ and the rank-2 light-shift induced by a linearly polarized light pulse with unit polarization vector $\boldsymbol{\epsilon}_{\text{L}}$ of the light field and off-resonant with detuning $\Delta_{ff'}$ from the D1-line transition with $f \to f'$. We take kick pulses to be polarized in x-direction, $\boldsymbol{\epsilon}_{\text{L}} = \hat{\mathbf{x}}$, while the pulse beam propagates in z-direction, as indicated in figure 1 (b). Further, the prefactor of the non-linearity consists of the characteristic Rabi frequency $\Omega = \gamma_{\text{nat}}\sqrt{I_{\text{kick}}/(2I_{\text{sat}})}$ of the D1 line, with saturation intensity of off-resonant linearly polarized light[34] $I_{\text{sat}} \simeq 2.5\,\text{mW}\,\text{cm}^{-2}$, natural line width γ_{nat}, kick-laser intensity I_{kick}, and coefficients

$$C_{j'f'f}^{(2)} = (-1)^{3f-f'}\frac{\sqrt{30}(2f'+1)}{\sqrt{f(f+1)(2f+1)(2f-1)(2f+3)}}\begin{Bmatrix}f & 1 & f'\\ 1 & f & 2\end{Bmatrix}\left|o_{1/2f}^{j'f'}\right|^2. \tag{5}$$

The curly braces denote the Wigner $6j$ symbol and $o_{jf}^{j'f'}$ is defined as

$$o_{jf}^{j'f'} = (-1)^{f'+1+j'+K}\sqrt{(2j'+1)(2f+1)}\begin{Bmatrix}f & K & j'\\ j & 1 & f\end{Bmatrix}, \tag{6}$$

where the total angular momenta of ground and excited levels of the D1 line are $j = j' = 1/2$. Photon scattering is taken into account by the imaginary shift $i\gamma_{\text{nat}}/2$ of the detuning $\Delta_{ff'}$ in the effective Hamiltonian and by the

remaining parts of the master equation that correspond to optical pumping which leads to cycles of excitation to the $6P_{1/2}$ manifold followed by spontaneous emission to the ground-electronic manifold $6S_{1/2}$. When the laser is switched off, the master equation solely involves the first four summands (spin exchange, spin destruction, hyperfine coupling, effective Hamiltonian) and the effective Hamiltonian reduces to the Larmor precession term.

The jump operators are given as[29]

$$W_q^{f_b f_a} = \sum_{f'=3}^{4} \frac{\Omega/2}{\Delta_{f_a f'} + i\gamma_{\text{nat}}/2} \left(\mathbf{e}_q^* \cdot \mathbf{D}_{f_b f'}\right) \left(\boldsymbol{\epsilon}_{\text{L}} \cdot \mathbf{D}_{f_a f'}^\dagger\right), \tag{7}$$

with the spherical basis $\mathbf{e}_1 = -(\hat{\mathbf{x}} + i\hat{\mathbf{y}})/\sqrt{2}$, $\mathbf{e}_0 = \hat{\mathbf{z}}$, $\mathbf{e}_{-1} = (\hat{\mathbf{x}} - i\hat{\mathbf{y}})/\sqrt{2}$, where $\hat{\mathbf{x}}, \hat{\mathbf{y}}, \hat{\mathbf{z}}$ denotes the Cartesian basis, and $\mathbf{D}_{ff'}^\dagger = \sum_{q,m,m'} \mathbf{e}_q^* o_{jf}^{j'f'} \langle f'm' | fm; 1q \rangle |f'm'\rangle\langle fm|$ is the raising operator with Clebsch-Gordan coefficients $\langle f'm' | fm; 1q \rangle$.

The Euler method is used to solve the non-linear trace-preserving master equation and hyperfine coupling is taken into account by setting off-diagonal blocks of the density matrix in the coupled $|fm\rangle$-basis after each Euler step to zero,[25] because they oscillate very quickly with frequency a_{hf}. In distinction from the kicked top model, kicks are not assumed to be arbitrarily short, i.e., kicks and precession coexist during a light pulse. In each Euler step during a kick, the non-linearity and the corresponding dissipation is factored in by calculating a superoperator and applying it to the state.

The period between pulses, and the duration and intensity of light pulses must be chosen such that the favorable effect of kicking outweighs the detrimental effect of induced decoherence. The intensity of the light pulses inducing the non-linear kicks is set to $I_{\text{kick}} = 0.1 \, \text{mW/cm}^2$ and light pulses are detuned halfway between the hyperfine splitting of $6^2P_{1/2}$, $\Delta_{34} \simeq -584 \, \text{MHz}$. The period is $\tau = 1 \, \text{ms}$ where during the last $2 \, \mu s$ of each period the light pulse is applied which corresponds to a very low effective kicking strength of $k \simeq 6.5 \times 10^{-4}$ for the lower hyperfine level of the ground state.

Doppler broadening is taken into account by numerically averaging the righthand side of the master equation over the Maxwell-Boltzmann distribution of velocities of an cesium atom. This translates into an average over detunings $\Delta_{ff'}$. We limit averaging over detunings to a 3σ interval because $\Delta \gg \Omega$ must hold within the description of the master equation.[29]

The initial spin-state is polarized with a circularly polarized pump beam in z-direction orthogonal to the magnetic field (see figure 1 (b)) resonant with the D1 line which in the presence of spin-relaxation leads to an effective thermal state[33]

$$\rho = \frac{e^{\beta K_z} e^{\beta S_z}}{Z_K Z_S}, \tag{8}$$

where $\beta = \ln \frac{1+q}{1-q}$, with polarization $q = 0.95$, and $Z_j = \sum_{m=-j}^{j} e^{\beta m}$ is the partition function. The readout is accomplished typically with the help of an off-resonant probe beam by measuring its polarization which experienced a Faraday rotation during the interaction with the atomic spin ensemble, see figure 1 (b). Since we are interested only in a comparison of measurement strategies, with kicks and without kicks, we do not model readout noise which is the same for both strategies.

4. MEASUREMENT PRECISION

We will first introduce Fisher information and quantum Fisher information and show the connection of the latter to fidelity establishing a fundamental relation between achievable measurement precision and quantum chaos. Then, we will compare measurement strategies (kicks versus no kicks) by means of these quantities.

4.1 Quantum Fisher information and fidelity

If the probability distribution of measurement outcomes depends on a parameter α, we can estimate α from the measurement outcomes. High measurement precision corresponds to a low variance (or standard deviation) of our estimate α_{est} of α which is lower bounded by the Cramér–Rao bound,

$$\text{Var}(\alpha_{\text{est}}) \geq \frac{1}{M I_{\text{Fisher},\alpha}}, \tag{9}$$

where M denotes the number of measurements and $I_{\mathrm{Fisher},\alpha}$ is the Fisher information.[35] It is given by

$$I_{\mathrm{Fisher},\alpha} := \int d\xi \frac{(dp_\alpha(\xi)/d\alpha)^2}{p_\alpha(\xi)}, \tag{10}$$

where $p_\alpha(\xi)$ denotes the probability of observing the measurement outcome ξ. Describing the parameter-dependent quantum state of the quantum sensor by a density operator ρ_α and the measurement by a positive operator-valued measure (POVM) $\{\Pi_\xi\}$ with positive operators Π_ξ that correspond to observing the measurement outcome ξ, the probability for observing ξ is given by the Born rule, $p_\alpha(\xi) = \mathrm{tr}\left[\Pi_\xi \rho_\alpha\right]$. Minimizing $\mathrm{Var}(\alpha_{\mathrm{est}})$ with respect to the choice of measurement, yields the quantum Cramér–Rao bound,

$$\mathrm{Var}(\alpha_{\mathrm{est}}) \geq \frac{1}{MI_\alpha}, \tag{11}$$

where I_α is the quantum Fisher information[36] (QFI),

$$I_\alpha = \lim_{\epsilon \to 0} 4\frac{1 - F_\epsilon}{\epsilon^2}, \tag{12}$$

with F_ϵ the fidelity between the state ρ_α and the perturbed state $\rho_{\alpha+\epsilon}$,

$$F_\epsilon = \left\|\sqrt{\rho_\alpha}\sqrt{\rho_{\alpha+\epsilon}}\right\|_2^2, \tag{13}$$

where $\|A\|_1 = \mathrm{tr}\sqrt{AA^\dagger}$ is the trace norm.

In the field of quantum chaos, fidelity, usually evaluated for pure states and unitary dynamics, is called Loschmidt echo and represents an important quantity to study the sensitivity to changes of a parameter of the dynamics.[37] As can be seen from equation (12), only in the limit of small perturbations, known as the perturbative regime,[38,39] QFI is given by the fidelity.

Comparing two measurement strategies by comparing the maximal QFI or Fisher information of both strategies is not fair in terms of resources if the maxima are reached at different times, i.e., if the two strategies consume different amounts of time. In principle, the faster measurement strategy could be followed up with another measurement until the other strategy is finished, or it might be better to not even wait until QFI is maximal but instead perform a series of shorter measurements*. This means that there is a tradeoff between measurement time and repetitions of a measurement which gives a prefactor M for the QFI (equation 11) for M repetitions. Therefore, we consider the rescaled QFI and rescaled Fisher information,

$$I_\alpha^{(t)} = \frac{I_\alpha}{t}, \tag{14}$$

$$I_{\mathrm{Fisher},\alpha}^{(t)} = \frac{I_{\mathrm{Fisher},\alpha}}{t}, \tag{15}$$

with measurement time t. Rescaled QFI (or rescaled Fisher information) decays if QFI (Fisher information) is $\propto t^x$ with $x < 1$ indicating that it is better to stop the measurement and start a new one; linear M scaling is then better than $\propto t^x$ scaling. Classical averaging over long times typically leads to a $x = 1$ scaling which motivates giving sensitivity (standard deviation of the estimator) in units of $1/\sqrt{\mathrm{Hz}}$ which is well established in experimental physics. On the other hand, quantum coherence typically leads to an $x = 2$ scaling. Rescaled QFI allows us to compare measurement strategies that use different amounts of time; best precision corresponds to the maximum rescaled QFI or Fisher information.

4.2 Comparison of a cesium-vapor magnetometer with and without kicks

We compare now the kicked cesium-vapor magnetometer in the SERF regime as described above (section 3.2) with exactly the same magnetometer in the absence of kicks, denoted as reference in the following. Figure

---

*The underlying assumption is that it is always possible to interrupt and repeat a measurement and that preparation and readout times of single measurements can be neglected.
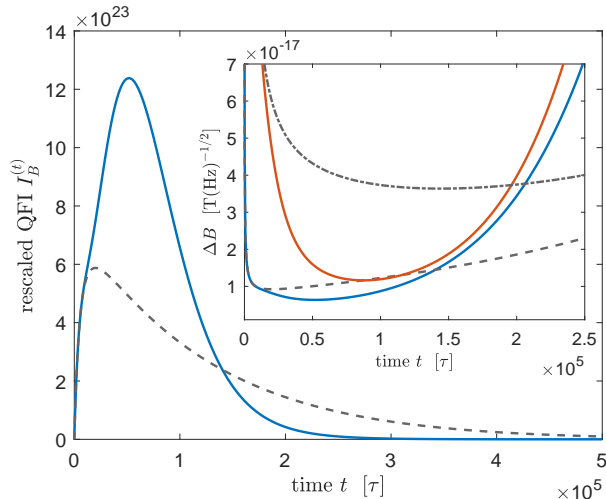
Figure 2: Performance of a magnetic-field measurement with a kicked cesium-vapor magnetometer. The gray dashed line shows the rescaled quantum Fisher information $I_B^{(t)}$ for measuring the magnetic field B, the blue line is obtained by periodically adding short optical kicks every $\tau = 1\,\mathrm{ms}$. The inset shows precision ΔB in units of $\mathrm{T}/\sqrt{\mathrm{Hz}}$ for an optimal measurement (gray dashed line and blue line without and with kicks, respectively) and for measuring the z-component of the electronic spin S_z (gray dash-dotted and red line without and with kicks, respectively).

2 shows rescaled QFI for both measurement strategies: It is remarkable that the rescaled QFI for the kicked magnetometer continues to increase when the reference already starts to decay due to decoherence although kicks introduce additional decoherence. The inset shows the measurement precision ΔB in units of $\mathrm{T}/\sqrt{\mathrm{Hz}}$ per $1\,\mathrm{cm}^3$ vapor volume. It is defined by $\Delta B = 1/\sqrt{n I_B^{(t)}}$, where $n \simeq 2 \times 10^{10}$ is the number of cesium atoms in $1\,\mathrm{cm}^3$, and for a specific measurement $I_B^{(t)}$ must be replaced by the corresponding rescaled Fisher information $I_{\mathrm{Fisher},\,B}^{(t)}$. We find about 31% improvement in measurement precision ΔB for an optimal measurement and 68% improvement in a comparison of measurements of the electronic spin component S_z. Such an S_z measurement is easily realized by measuring the Faraday rotation of an off-resonant readout beam with a polarization measurement as indicated in figure 1 (b).

5. DISCUSSION

We propose a method to improve sensitivity of a cesium-vapor magnetometer in the spin-exchange relaxation-free regime. We do not need to prepare an initial entangled states but supplement the spin-precession dynamics of the magnetometer with nonlinear kicks generated with off-resonant light pulses via the ac Stark effect. The interplay of precession in the magnetic field and non-linear kicks put the dynamics in the regime of quantum chaos. A simulation of the magnetometer based on a master equation including all relevant decoherence mechanisms reveals improved robustness with respect to decoherence by including non-linear kicks to the dynamics even though kicks induce additional decoherence.[17] In our concrete example we find up to 68% improvement in measurement precision over a the same magnetometer in the absence of kicks. We expect a further improvement in precision if the transmission of the off-resonant kick pulses is measured. Large improvements can be expected by increasing the system size, which is restricted to single cesium spins in our case because the non-linear kicks act only on single atom spins. Applying the non-linear kicks to the joint spin of cesium atoms in the vapor cell could be realized by exploiting effective interactions between the atoms in a cavity as suggested in[40] or by using the interaction with a propagating light field as demonstrated experimentally in[41, 42] with about 10^{12} cesium atoms. Finally, the idea of a quantum-chaotic sensor[17] is very general and we expect improvements in many other quantum sensors that can be rendered chaotic as well; candidates are BECs or arrays of NV centers exploiting interactions leading to an effective non-linearity.

Acknowledgments

Competing Interests

The authors declare no competing interests.

REFERENCES

[1] H. Mamin, M. Kim, M. Sherwood, C. Rettner, K. Ohno, D. Awschalom, and D. Rugar, "Nanoscale nuclear magnetic resonance with a nitrogen-vacancy spin sensor," *Science* **339**(6119), pp. 557–560, 2013.

[2] B. H. Lee, Y. H. Kim, K. S. Park, J. B. Eom, M. J. Kim, B. S. Rho, and H. Y. Choi, "Interferometric fiber optic sensors," *sensors* **12**(3), pp. 2467–2486, 2012.

[3] A. Peters, K. Y. Chung, and S. Chu, "High-precision gravity measurements using atom interferometry," *Metrologia* **38**(1), p. 25, 2001.

[4] S. F. Huelga, C. Macchiavello, T. Pellizzari, A. K. Ekert, M. B. Plenio, and J. I. Cirac, "Improvement of Frequency Standards with Quantum Entanglement," *Phys. Rev. Lett.* **79**(20), pp. 3865–3868, 1997.

[5] V. Meyer, M. A. Rowe, D. Kielpinski, C. A. Sackett, W. M. Itano, C. Monroe, and D. J. Wineland, "Experimental Demonstration of Entanglement-Enhanced Rotation Angle Estimation Using Trapped Ions," *Phys. Rev. Lett.* **86**, pp. 5870–5873, Jun 2001.

[6] D. Leibfried, M. Barrett, T. Schaetz, J. Britton, J. Chiaverini, W. Itano, J. Jost, C. Langer, and D. Wineland, "Toward Heisenberg-Limited Spectroscopy with Multiparticle Entangled States," *Science* **304**(5676), pp. 1476–1478, 2004.

[7] W. Wasilewski, K. Jensen, H. Krauter, J. J. Renema, M. V. Balabas, and E. S. Polzik, "Quantum Noise Limited and Entanglement-Assisted Magnetometry," *Phys. Rev. Lett.* **104**, p. 133601, Mar 2010.

[8] M. Koschorreck, M. Napolitano, B. Dubost, and M. W. Mitchell, "Sub-Projection-Noise Sensitivity in Broadband Atomic Magnetometry," *Phys. Rev. Lett.* **104**, p. 093602, Mar 2010.

[9] V. Giovannetti, S. Lloyd, and L. Maccone, "Quantum-enhanced positioning and clock synchronization," *Nature* **412**, pp. 417–419, 2001.

[10] E. H. Allen and M. Karageorgis, "Radar systems and methods using entangled quantum particles," May 20 2008. US Patent 7,375,802.

[11] J. Taylor, P. Cappellaro, L. Childress, L. Jiang, D. Budker, P. Hemmer, A. Yacoby, R. Walsworth, and M. Lukin, "High-sensitivity diamond magnetometer with nanoscale resolution," *Nature Physics* **4**(10), pp. 810–816, 2008.

[12] K. Goda, O. Miyakawa, E. E. Mikhailov, S. Saraf, R. Adhikari, K. McKenzie, R. Ward, S. Vass, A. J. Weinstein, and N. Mavalvala, "A quantum-enhanced prototype gravitational-wave detector," *Nature Physics* **4**, pp. 472–476, 2008.

[13] J. Aasi, J. Abadie, B. Abbott, R. Abbott, T. Abbott, M. Abernathy, C. Adams, T. Adams, P. Addesso, R. Adhikari, *et al.*, "Enhanced sensitivity of the LIGO gravitational wave detector by using squeezed states of light," *Nature Photonics* **7**(8), pp. 613–619, 2013.

[14] L. Pezzè, A. Smerzi, M. K. Oberthaler, R. Schmied, and P. Treutlein, "Quantum metrology with nonclassical states of atomic ensembles," *Reviews of Modern Physics* **90**(3), p. 035005, 2018.

[15] B. Escher, R. de Matos Filho, and L. Davidovich, "General framework for estimating the ultimate precision limit in noisy quantum-enhanced metrology," *Nature Physics* **7**(5), p. 406, 2011.

[16] R. Demkowicz-Dobrzański, J. Kołodyński, and M. Guţă, "The elusive heisenberg limit in quantum-enhanced metrology," *Nature communications* **3**, p. 1063, 2012.

[17] L. J. Fiderer and D. Braun, "Quantum metrology with quantum-chaotic sensors," *Nature communications* **9**(1), p. 1351, 2018.

[18] F. Haake, M. Kuś, and R. Scharf, "Classical and quantum chaos for a kicked top," *Zeitschrift für Physik B Condensed Matter* **65**(3), pp. 381–395, 1987.

[19] F. Haake, M. Kuś, and R. Scharf in *Coherence, Cooperation, and Fluctuations*, F. Haake, L. Narducci, and D. Walls, eds., Cambridge University Press, (Cambridge), 1986.

[20] F. Haake, *Quantum Signatures of Chaos*, vol. 54, Springer Science & Business Media, Berlin, 2013.

[21] S. Chaudhury, A. Smith, B. Anderson, S. Ghose, and P. S. Jessen, "Quantum signatures of chaos in a kicked top," *Nature* **461**(7265), pp. 768–771, 2009.

[22] V. Krithika, V. Anjusha, U. T. Bhosale, and T. Mahesh, "Nmr studies of quantum chaos in a two-qubit kicked top." 2018.

[23] J. Allred, R. Lyman, T. Kornack, and M. Romalis, "High-Sensitivity Atomic Magnetometer Unaffected by Spin-Exchange Relaxation," *Phys. Rev. Lett.* **89**(13), p. 130801, 2002.

[24] I. K. Kominis, T. W. Kornack, J. C. Allred, and M. V. Romalis, "A subfemtotesla multichannel atomic magnetometer," *Nature* **422**, pp. 596–599, 2003.

[25] I. Savukov and M. Romalis, "Effects of spin-exchange collisions in a high-density alkali-metal vapor in low magnetic fields," *Phys. Rev. A* **71**(2), p. 023405, 2005.

[26] D. Budker and M. Romalis, "Optical magnetometry," *Nature Physics* **3**(4), pp. 227–234, 2007.

[27] D. Sheng, S. Li, N. Dural, and M. Romalis, "Subfemtotesla Scalar Atomic Magnetometry Using Multipass Cells," *Phys. Rev. Lett.* **110**(16), p. 160802, 2013.

[28] M. Balabas, T. Karaulanov, M. Ledbetter, and D. Budker, "Polarized Alkali-Metal Vapor with Minute-Long Transverse Spin-Relaxation Time," *Phys. Rev. Lett.* **105**(7), p. 070801, 2010.

[29] I. H. Deutsch and P. S. Jessen, "Quantum control and measurement of atomic spins in polarization spectroscopy," *Optics Communications* **283**(5), pp. 681–694, 2010.

[30] T. Fernholz, H. Krauter, K. Jensen, J. F. Sherson, A. S. Sørensen, and E. S. Polzik, "Spin squeezing of atomic ensembles via nuclear-electronic spin entanglement," *Physical review letters* **101**(7), p. 073601, 2008.

[31] N. Bhaskar, J. Pietras, J. Camparo, W. Happer, and J. Liran, "Spin destruction in collisions between cesium atoms," *Phys. Rev. Lett.* **44**(14), p. 930, 1980.

[32] M. Ledbetter, I. Savukov, V. Acosta, D. Budker, and M. Romalis, "Spin-exchange-relaxation-free magnetometry with Cs vapor," *Phys. Rev. A* **77**(3), p. 033408, 2008.

[33] S. Appelt, A. B.-A. Baranga, C. Erickson, M. Romalis, A. Young, and W. Happer, "Theory of spin-exchange optical pumping of ^{3}He and ^{129}Xe," *Phys. Rev. A* **58**(2), pp. 1412–1439, 1998.

[34] D. A. Steck, "Cesium D line data," 2003.

[35] C. W. Helstrom, "Quantum detection and estimation theory," *Journal of Statistical Physics* **1**(2), pp. 231–252, 1969.

[36] S. L. Braunstein and C. M. Caves, "Statistical distance and the geometry of quantum states," *Phys. Rev. Lett.* **72**, pp. 3439–3443, May 1994.

[37] T. Gorin, T. Prosen, T. H. Seligman, and M. Žnidarič, "Dynamics of Loschmidt echoes and fidelity decay," *Physics Reports* **435**(2), pp. 33–156, 2006.

[38] P. Jacquod, P. Silvestrov, and C. Beenakker, "Golden rule decay versus Lyapunov decay of the quantum Loschmidt echo," *Phys. Rev. E* **64**, p. 055203, Oct 2001.

[39] G. Benenti and G. Casati, "Quantum-classical correspondence in perturbed chaotic systems," *Phys. Rev. E* **65**, p. 066205, Jun 2002.

[40] G. Agarwal, R. Puri, and R. Singh, "Atomic Schrödinger cat states," *Phys. Rev. A* **56**(3), pp. 2249–2254, 1997.

[41] M. Takeuchi, S. Ichihara, T. Takano, M. Kumakura, T. Yabuzaki, and Y. Takahashi, "Spin Squeezing via One-Axis Twisting with Coherent Light," *Phys. Rev. Lett.* **94**(2), p. 023003, 2005.

[42] B. Julsgaard, A. Kozhekin, and E. S. Polzik, "Experimental long-lived entanglement of two macroscopic objects," *Nature* **413**, pp. 400–403, 2001.

Maximal Quantum Fisher Information for Mixed States

Lukas J. Fiderer,[1] Julien M. E. Fraïsse,[2] and Daniel Braun[1]

[1]*Eberhard-Karls-Universität Tübingen, Institut für Theoretische Physik, 72076 Tübingen, Germany*
[2]*Seoul National University, Department of Physics and Astronomy,
Center for Theoretical Physics, 151-747 Seoul, Korea*

We study quantum metrology for unitary dynamics. Analytic solutions are given for both the optimal unitary state preparation starting from an arbitrary mixed state and the corresponding optimal measurement precision. This represents a rigorous generalization of known results for optimal initial states and upper bounds on measurement precision which can only be saturated if pure states are available. In particular, we provide a generalization to mixed states of an upper bound on measurement precision for time-dependent Hamiltonians that can be saturated with optimal Hamiltonian control. These results make precise and reveal the full potential of mixed states for quantum metrology.

The standard paradigm of quantum metrology involves the preparation of an initial state, a parameter-dependent dynamics, and a consecutive quantum measurement of the evolved state. From the measurement outcomes the parameter can be estimated [1–3]. Naturally, it is the goal to estimate the parameter as precisely as possible, i.e., to reduce the uncertainty $\Delta\hat{\alpha} = \mathrm{Var}(\hat{\alpha})^{1/2}$ of the estimator $\hat{\alpha}$ of the parameter α that we want to estimate. We consider single parameter estimation in the local regime where one already has a good estimate $\hat{\alpha}$ at hand (typically from prior measurements) such that this prior knowledge can be used to prepare and control consecutive measurements. Quantum coherence and nonclassical correlations in quantum sensors help to reduce the uncertainty $\Delta\hat{\alpha}$ compared to what is possible with comparable classical resources [4,5]. The ultimate precision limit for unbiased estimators is given by the quantum Cramér-Rao bound $\Delta\hat{\alpha} \geq (MI_\alpha)^{-1/2}$, which depends on the number of measurements M and the quantum Fisher information (QFI) I_α which is a function of the state [6,7]. When the number of measurements is fixed, as they correspond to a limited resource, precision is optimal when the QFI is maximal which involves an optimization with respect to the state.

In this Letter, we consider a freely available state ρ, unitary freedom to prepare an initial state from ρ, and unitary parameter-dependent dynamics of the quantum system (see Fig. 1). The parameter-dependent dynamics will be called sensor dynamics in the following in order to distinguish it from the state preparation dynamics. For instance, in a spin system the unitary freedom can be used to squeeze the spin before it is subjected to the sensor dynamics, as it is the case in many quantum-enhanced measurements [8–11]. In the worst-case scenario, only the maximally mixed state is available, which does not change under unitary state preparation or unitary sensor dynamics

and, thus, no information about the parameter can be gained. In the best-case scenario, the available state is pure, and the maximal QFI as well as the optimal state to be prepared are well known [12,13].

The appeal and advantage of the theoretical study of unitary sensor dynamics lies in the analytic solutions that can be found that allow fundamental insights in the limits of quantum metrology and the role of resources such as measurement time and system size. The QFI maximized with respect to initial states, also known as channel QFI, can be reached only with pure initial states. If only mixed states are available, as it is usually the case under realistic conditions, this upper bound cannot be saturated and therefore has limited significance. In fact, if pure states are not available, the question for the maximal QFI and optimal state to be prepared is an important open problem [14,15]. The main result of this Letter, Theorem 1 below, is the complete solution of this problem.

The solution is relevant for practically all quantum sensors, as perfect initialization to a pure state can only be achieved to a certain degree that varies with the quantum system and the available technology. For example, nitrogen-vacancy (NV) center arrays [16,17] or atomic-vapor magnetometers [18,19] operate with mixed initial states due to imperfect polarization and competing depolarization effects [20,21]. Particularly relevant is the example of sensors based on nuclear spin ensembles that typically
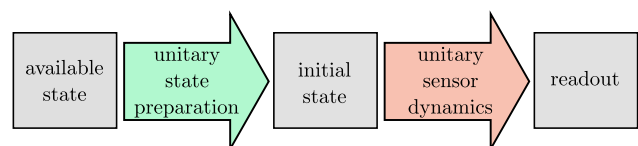

FIG. 1. Schematic representation of the metrology protocol.

operate with nuclear spins in thermal equilibrium, such that at room temperature the available state is strongly mixed [22]. Hence, the full potential of quantum metrology is exploited only when the mixedness of initial states is taken into account [14,23–25].

We consider arbitrary, possibly time-dependent Hamiltonians $H_\alpha(t)$ for the sensor dynamics. The corresponding unitary evolution operator is $U_\alpha := \mathcal{T}(\exp[-i/\hbar \int_0^T H_\alpha(t)dt])$, where $\mathcal{T}$ denotes time ordering, T is the total time of the sensor dynamics, and we set $\hbar = 1$ in the following. In the simplest case, dynamics is generated by a "phase-shift" or "precession" Hamiltonian proportional to the parameter α, $H_\alpha = \alpha G$, with some parameter-independent operator G. The parameter dependence of the sensor dynamics is characterized by the generator $h_\alpha := iU_\alpha^\dagger(\partial U_\alpha/\partial \alpha)$, which simplifies to G for phase-shift Hamiltonians [12,26–28].

By introducing the eigendecomposition of the prepared initial state $\rho = \sum_{k=1}^d p_k|\psi_k\rangle\langle\psi_k|$, where d is the dimension of the Hilbert space, the QFI can be expressed as [7], [14]

$$I_\alpha(\rho) := 2\sum_{k,\ell=1}^d p_{k,\ell}|\langle\psi_k|h_\alpha|\psi_\ell\rangle|^2, \quad (1)$$

with coefficients

$$p_{k,\ell} := \begin{cases} 0 & \text{if } p_k = p_\ell = 0, \\ \frac{(p_k - p_\ell)^2}{p_k + p_\ell} & \text{else.} \end{cases} \quad (2)$$

Also, let $\mathcal{U}(d)$ denote the set of $d \times d$ unitary matrices.

Theorem 1: For any state ρ and any generator h_α with ordered eigenvalues $p_1 \geq \cdots \geq p_d$ and $h_1 \geq \cdots \geq h_d$, respectively, the maximal QFI with respect to all unitary state preparations $U\rho U^\dagger$, $U \in \mathcal{U}(d)$, is given by

$$I_\alpha^* := \max_U I_\alpha(U\rho U^\dagger) = \frac{1}{2}\sum_{k=1}^d p_{k,d-k+1}(h_k - h_{d-k+1})^2. \quad (3)$$

Let $|h_k\rangle$ be the eigenvectors of the generator, $h_\alpha|h_k\rangle = h_k|h_k\rangle$. The maximum I_α^* is obtained by preparing the initial state

$$\rho^* = \sum_{k=1}^d p_k|\phi_k\rangle\langle\phi_k|, \quad (4)$$

with [29]

$$|\phi_k\rangle = \begin{cases} \frac{|h_k\rangle + |h_{d-k+1}\rangle}{\sqrt{2}} & \text{if } 2k < d+1, \\ |h_k\rangle & \text{if } 2k = d+1, \\ \frac{|h_k\rangle - |h_{d-k+1}\rangle}{\sqrt{2}} & \text{if } 2k > d+1. \end{cases} \quad (5)$$

The proof is based on the Bloomfield-Watson inequality on the Hilbert-Schmidt norm of off-diagonal blocks of a Hermitian matrix [30,31] and is given in the Supplemental Material [32]. The idea of the proof is to construct an upper bound for the QFI in Eq. (3) that exhibits a simpler dependence on the coefficients $p_{k,\ell}$. Then we maximize the upper bound by exploiting the Bloomfield-Watson inequality. The proof is concluded by showing that at its maximum the upper bound equals the QFI.

It is important to notice that the rank r of the state ρ plays a crucial role both for the maximal QFI and for the optimal state: in order to reach the maximal QFI I_α^*, the choice of the $|\phi_k\rangle$ corresponding to vanishing p_k, i.e., for $k > r$, is irrelevant. This is best exemplified by considering the well-known case of pure states, characterized by $p_1 = 1$ and $r = 1$ [12,26,27,33,34]. Then, the maximal QFI in Eq. (3) simply becomes $(h_1 - h_d)^2$ and is obtained by preparing an equal superposition $(|h_1\rangle + |h_d\rangle)/\sqrt{2}$ of the eigenvectors corresponding to the minimal and maximal eigenvalues of h_α. When the rank is increased but remains less than or equal to $(d+1)/2$, the optimal QFI is equal to $\sum_{i=1}^r p_i(h_i - h_{d-i+1})^2$. This can be seen as a convex sum of pure-state QFIs [35].

The situation changes when the rank is increased even further. For example with $r = 4$ and $d = 5$, the maximal QFI is equal to $p_1(h_1 - h_5)^2 + [(p_2 - p_4)^2/(p_2 + p_4)](h_2 - h_4)^2$. Further, for a Hilbert space of odd dimension, the vector $|\phi_{(d+1)/2}\rangle = |h_{(d+1)/2}\rangle$ is an eigenstate of the generator: it remains invariant under the dynamics and does not contribute to the QFI. For example for both $r = 2$ and $r = 3$ with $d = 5$, the optimal QFI is given by $p_1(h_1 - h_5)^2 + p_2(h_2 - h_4)^2$.

We obtained I_α^* by optimizing with respect to unitary state preparation while keeping the sensor dynamics fixed (see Fig. 1). However, in practice it is often possible not only to manipulate the available state but also the sensor dynamics by adding a parameter-independent control Hamiltonian $H_c(t)$ to the original Hamiltonian $H_\alpha(t)$. While Theorem 1 holds for any $H_\alpha(t)$, it is an interesting question to what extent the maximal QFI in Eq. (3) can be increased by adding a time-dependent control Hamiltonian. Again, the answer is only known for pure states [34]. The question, how this generalizes if the available state is mixed, brings us to

Theorem 2: For any state ρ with ordered eigenvalues $p_1 \geq \cdots \geq p_d$ and any time-dependent Hamiltonian $H_\alpha(t)$, where $\mu_1(t) \geq \cdots \geq \mu_d(t)$ are the ordered eigenvalues of $\partial_\alpha H_\alpha(t) := \partial H_\alpha(t)/\partial\alpha$, an upper bound for the QFI is given by

$$K_\alpha = \frac{1}{2}\sum_{k=1}^d p_{k,d-k+1}\left(\int_0^T [\mu_k(t) - \mu_{d-k+1}(t)]dt\right)^2. \quad (6)$$

Let $|\mu_k(t)\rangle$ be the time-dependent eigenvectors of $\partial_\alpha H_\alpha(t)$, $\partial_\alpha H_\alpha(t)|\mu_k(t)\rangle = \mu_k(t)|\mu_k(t)\rangle$. The upper bound K_α is reached by preparing the initial state

$$\rho^* = \sum_{k=1}^{d} p_k |\phi_k\rangle\langle\phi_k|, \qquad (7)$$

with

$$|\phi_k\rangle = \begin{cases} \frac{|\mu_k(0)\rangle + |\mu_{d-k+1}(0)\rangle}{\sqrt{2}} & \text{if } 2k < d+1, \\ |\mu_k(0)\rangle & \text{if } 2k = d+1, \\ \frac{|\mu_k(0)\rangle - |\mu_{d-k+1}(0)\rangle}{\sqrt{2}} & \text{if } 2k > d+1, \end{cases} \qquad (8)$$

and choosing the Hamiltonian control $H_c(t)$ such that

$$U_\alpha(t)|\mu_k(0)\rangle = |\mu_k(t)\rangle \quad \forall \ k = 1,...,d \quad \forall \ t, \quad (9)$$

where

$$U_\alpha(t) = \mathcal{T}\left[\exp\left(-i \int_0^t [H_\alpha(\tau) + H_c(\tau)]d\tau\right)\right]. \quad (10)$$

The proof (see the Supplemental Material [32]) starts by rewriting h_α as in Ref. [[34] Eq. (6)] and shows that Eq. (6) is an upper bound for Eq. (3). We use the Schur convexity [38] of Eq. (3) and the inequalities from K. Fan [39,40] for eigenvalues of the sum of two Hermitian matrices.

One of the strengths of the bound K_α is that it is given by the eigenvalues of $\partial_\alpha H_\alpha(t)$ and does not depend on the full unitary operator of the sensor dynamics which is hard to calculate for time-dependent Hamiltonians. The optimal initial state with Hamiltonian control in Theorem 2 differs from the optimal initial state without Hamiltonian control in Theorem 1 by the fact that the eigenvectors of the generator h_α in Eq. (5) are replaced by those of $\partial_\alpha H_\alpha(0)$ in Eq. (8). The reason for this is that the optimal initial state of Theorem 1 is the most sensitive state with respect to the sensor dynamics U_α. However, if the Hamiltonian is time dependent, the state which is most sensitive to the sensor dynamics at time t will also be time dependent in general. Since the Hamiltonian control is allowed to be time dependent, we can take this into account and ensure that the optimal initial state evolves such that it is most sensitive to the sensor dynamics for all times t. This corresponds to the condition in Eq. (9). Only in special cases, such as phase-shift Hamiltonians $H_\alpha = \alpha G$, we have $h_\alpha = \partial_\alpha H_\alpha$ and, thus, the optimal initial states of Theorems 1 and 2 are the same. If they are not the same, a Hamiltonian H_α can be seen as suboptimal and requires correction by means of the Hamiltonian control in order to reach the upper bound of Theorem 2.

Formally, the optimal control Hamiltonian from Theorem 2 depends on the (unknown) parameter α. Since we are in the local parameter estimation regime, we have knowledge (from prior measurements) about α such that α can be replaced by the estimate $\hat{\alpha}$. It was shown that replacing α by $\hat{\alpha}$ in the optimal control Hamiltonian does not ruin the

benefits from introducing Hamiltonian control [34], and Hamiltonian control was applied experimentally with great success in Ref. [41]. For a more detailed discussion of control Hamiltonians we refer to the work of Pang *et al.* [34,42].

As applications of our theorems we consider two examples: the estimation of a magnetic field amplitude and the estimation of the frequency of an oscillating magnetic field. Both cases can be described with the general Hamiltonian of a system of N spin-j particles subjected to a (time-dependent) magnetic field

$$H(t) = \sum_{k=1}^{N} Bf(t)S_z^{(k)} + H_{\text{int}}, \qquad (11)$$

with the magnetic field amplitude B, some time-dependent real-valued modulation function $f(t)$, and spin operator $S_z^{(k)}$ in the z direction of the kth spin. We use the standard angular momentum algebra, $S_z^{(k)}|j,m\rangle = m|j,m\rangle$ with $m = -j,...,j$. H_{int} is independent of B and takes into account possible interactions between spins. This rather general Hamiltonian can be seen as an idealization of quantum sensors based on arrays of NV centers [16,17,43], nuclear spin ensembles [44], or vapor of alkali atoms [19]. Due to imperfect polarization and competing depolarization effects [20,21,45,46], the available states are mixed.

Here, we consider the available state of each of the N spins to be described by a spin-temperature distribution [independent of the Hamiltonian in Eq. (11)]

$$\rho_{\text{th}} = \frac{e^{\beta S_z}}{Z}, \qquad (12)$$

with partition function $Z = \sum_{m=-j}^{j} e^{\beta m}$, and inverse (effective) temperature β. Equation (12) was derived for optically polarized alkali vapors in [[20] Eq. (112)], and we assume that it is also a good approximation for the other spin-based magnetometers mentioned. β is related to the degree of polarization $P \in [0,1]$ by $\beta = \ln[1 + P/(1-P)]$; $P = 1$ corresponds to a perfectly polarized spin in z direction, described by a pure state, and $P = 0$ corresponds to an unpolarized spin, i.e., a maximally mixed state. The available state of the total system is a tensor product of spin-temperature distributions, $\rho = \rho_{\text{th}}^{\otimes N}$.

For the estimation of the amplitude B we assume that the modulation $f(t)$ is known [the case of unknown $f(t)$ would correspond to waveform estimation [47,48]]. This is naturally the case for (quasi)constant magnetic fields, periodic fields of known frequency, or, for example, when the modulation originates from a relative movement of sensor and environment (the source of B) that is tracked separately with another sensor. The maximal QFI obtained by using control Hamiltonians (cf. Theorem 2) for estimating the amplitude B is found to be
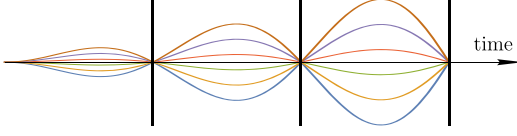
FIG. 2.   Exemplary sketch of time-dependent eigenvalues $\mu_1 \geq \cdots \geq \mu_6$ of $\partial H(t)/\partial \omega$ corresponding to $f(t) = \cos(\omega t)$. Vertical black lines indicate the position of single-spin π pulses about the x axis in order to interchange eigenvectors $|j, m\rangle \leftrightarrow |j, -m\rangle$.

$$K_B = g^2(T) \sum_{k=-Nj}^{Nj} q(k) \frac{\sinh^2(\beta k)}{Z^N \cosh(\beta k)} (2k)^2, \quad (13)$$

where $q(k)$ takes into account the degeneracy of eigenvalues of ρ and $\partial_B H(t) := \partial H(t)/\partial B$. It follows from the definition of the tensor product that the degeneracy of the kth eigenvalue of both, ρ and $\partial_B H(t)$, where eigenvalues are in weakly decreasing order, equals the number of possibilities $q(k)$ of getting a sum k when rolling N fair dice, each having $2j + 1$ sides corresponding to values $\{-j, \ldots, j\}$ (see the Supplemental Material [32]) [[49] p. 23–24]:

$$q(k) := \sum_{\ell=0}^{N} (-1)^\ell \binom{N}{\ell} \binom{k + N(j+1) - 1 - \ell(2j+1)}{N - 1},$$

$$(14)$$

where the binomial coefficient $\binom{a}{b}$ is set to zero if one or both of its coefficients are negative. The dependence on measurement time T is given by $g(T) = \int_0^T |f(t)| dt$.

The QFI in Eq. (13) exhibits a complicated dependence on the number of thermal states N and their spin size j. However, by deriving a lower bound for Eq. (13), we prove that the QFI scales $\propto N^2$ for any j as well as $\propto j^2$ for any N. In particular, we find $K_B = 4N^2 \langle S_z \rangle^2 + \mathcal{O}(N)$ where $\langle S_z \rangle = \text{tr}[\rho_{\text{th}} S_z]$, and $\mathcal{O}(N)$ denotes terms of order N and

lower order. In the limit of large temperatures, $\langle S_z \rangle^2$ decays as β^2 (see the Supplemental Material [32]).

This means that Heisenberg scaling [1,50,51], i.e., the quadratic scaling with the system size j or the number of particles N, is obtained for the optimal unitary state preparation even if only thermal states are available. Note that this also holds in the context of Theorem 1 if the generator equals S_z. Importantly, Heisenberg scaling is found for any finite temperature of the thermal state; only in the limit of infinite temperature, the available state is fully mixed and the QFI vanishes.

In order to attain the QFI (13), the conditions (9) must be fulfilled. In particular the Hamiltonian control must cancel interactions between the spins; i.e., H_{int} must be compensated. Also, every time the modulation function $f(t)$ changes its sign, we must apply a transformation which interchanges the eigenstates corresponding to a (degenerate) eigenvalue $e^{\beta k}/Z^N$ of ρ with the eigenstates corresponding to the (degenerate) eigenvalue $e^{-\beta k}/Z^N$ for all $k = 1, \ldots, Nj$. This is realized, for instance, with a local π pulse about the x axis, which interchanges $|j, m\rangle$ and $|j, -m\rangle$ for every single spin. The π pulses ensure optimal phase accumulation of the optimal state given by Eq. (7) (cf. Fig. 2).

The degeneracy of eigenvalues of ρ and $\partial_B H(t)$ leads to a freedom in preparing the optimal initial state. The special case of qubits, $j = 1/2$, constant magnetic field, $f(t) = 1$, and no interactions, $H_{\text{int}} = 0$, was studied by Modi et al. [14]. In this case, no Hamiltonian control is required, which brings us back to Theorem 1. They conjectured that a unitary state preparation consisting of a mixture of GHZ states is optimal in their case and calculated the QFI. Theorem 1 confirms their conjecture.

If, instead of the amplitude, we want to estimate the frequency ω of a periodic magnetic field with known amplitude B, $f(t) = \cos(\omega t)$, the eigenvalues of $\partial H(t)/\partial \omega$ are modulated not with $f(t)$ but with $\partial f(t)/\partial \omega = -t \sin(\omega t)$, see Fig. 2. The maximal QFI K_ω equals Eq. (13)
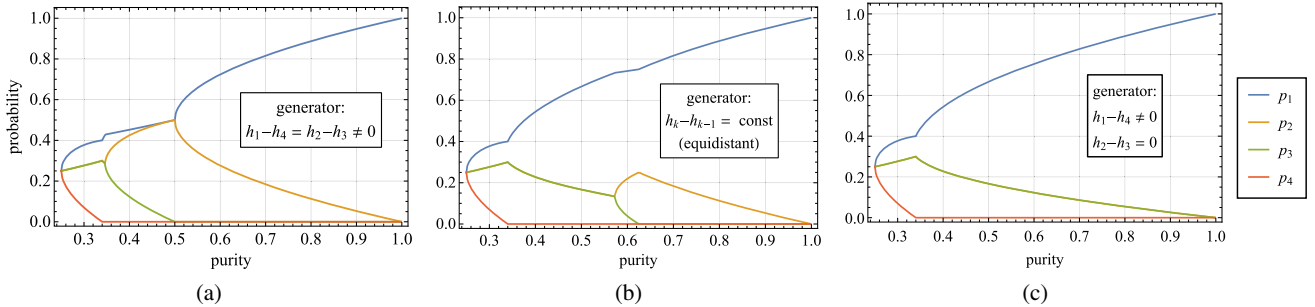
FIG. 3.   Eigenvalues $p_1 \geq \cdots \geq p_4$ of initial two-qubit states that maximize the QFI for different values of purity γ. For each value of purity, eigenvalues p_i are found numerically by maximizing the expression for maximal QFI from Theorem 1 in Eq. (3) under the constraints of fixed purity and conservation of probability, $\sum_k p_k = 1$. Different panels correspond to different spectra of the generator with eigenvalues $h_1 \geq \cdots \geq h_4$ as indicated in the insets. The generator used in panel (a) has two degeneracies, the one in panel (b) has an equidistant spectrum, and the one in panel (c) has one degeneracy. In panel (c), the line corresponding to p_3 overlays the line of p_2.

with the only difference that $g(T)$ is replaced by $g_\omega(T) = \int_0^T Bt |\sin(\omega t)| dt \simeq BT^2/\pi$, corresponding to a T^4 scaling of QFI, similar to what was reported in Ref. [34]. The optimal control is similar to the estimation of B: interactions must be canceled and local π pulses about the x axis must be applied whenever $\partial f(t)/\partial \omega$ crosses zero.

Theorem 1 also allows us to study the problem of optimal initial states of given purity $\gamma = \text{tr}\rho^2$. Fixing only γ amounts to an additional optimization over the spectrum of the initial state, which we solve numerically. As an example, we consider a two-qubit system with eigenvalues $p_1 \geq \cdots \geq p_4$, see Fig. 3. We observe that different levels of degeneracy of the spectrum of the generator results in distinct solutions for the optimal eigenvalues p_k.

In conclusion, Theorems 1 and 2 give an answer to the question of optimal unitary state preparation and optimal Hamiltonian control for an available mixed state and given unitary sensor dynamics that encodes the parameter to be measured in the quantum state. In comparison, distilling pure from mixed states at the cost of reducing the number of available probes would be an alternative. However, probes are typically a valuable resource that is utilized most efficiently along the lines of Theorem 1 and 2. The two theorems allow one to study quantum metrology with mixed states with the same analytical rigor as for pure states, and the well-known results about optimal pure states are recovered as special cases. We find that Heisenberg scaling of the QFI can be reached with thermal states: initial mixedness is not as detrimental as Markovian decoherence during or after the sensor dynamics, which is known to generally destroy the Heisenberg scaling of the QFI [52–54].

---

[1] V. Giovannetti, S. Lloyd, and L. Maccone, Quantum-enhanced measurements: Beating the standard quantum limit, Science **306**, 1330 (2004).

[2] M. G. A. Paris, Quantum estimation for quantum technology, Int. J. Quantum. Inform. **07**, 125 (2009).

[3] V. Giovannetti, S. Lloyd, and L. Maccone, Advances in quantum metrology, Nat. Photonics **5**, 222 (2011).

[4] L. Pezzè, A. Smerzi, M. K. Oberthaler, R. Schmied, and P. Treutlein, Quantum metrology with nonclassical states of atomic ensembles, Rev. Mod. Phys. **90**, 035005 (2018).

[5] D. Braun, G. Adesso, F. Benatti, R. Floreanini, U. Marzolino, M. W. Mitchell, and S. Pirandola, Quantum-enhanced measurements without entanglement, Rev. Mod. Phys. **90**, 035006 (2018).

[6] C. W. Helstrom, *Quantum Detection and Estimation Theory, Mathematics in Science and Engineering* Vol. 123 (Elsevier, New York, 1976).

[7] S. L. Braunstein and C. M. Caves, Statistical Distance and the Geometry of Quantum States, Phys. Rev. Lett. **72**, 3439 (1994).

[8] T. Fernholz, H. Krauter, K. Jensen, J. F. Sherson, A. S. Sørensen, and E. S. Polzik, Spin Squeezing of Atomic Ensembles via Nuclear-Electronic Spin Entanglement, Phys. Rev. Lett. **101**, 073601 (2008).

[9] A. André and M. D. Lukin, Atom correlations and spin squeezing near the Heisenberg limit: Finite-size effect and decoherence, Phys. Rev. A **65**, 053819 (2002).

[10] I. D. Leroux, M. H. Schleier-Smith, and V. Vuletić, Implementation of Cavity Squeezing of a Collective Atomic Spin, Phys. Rev. Lett. **104**, 073602 (2010).

[11] C. Orzel, A. K. Tuchman, M. L. Fenselau, M. Yasuda, and M. A. Kasevich, Squeezed states in a Bose-Einstein condensate, Science **291**, 2386 (2001).

[12] V. Giovannetti, S. Lloyd, and L. Maccone, Quantum Metrology, Phys. Rev. Lett. **96**, 010401 (2006).

[13] A. Fujiwara and H. Imai, A fibre bundle over manifolds of quantum channels and its application to quantum statistics, J. Phys. A **41**, 255304 (2008).

[14] K. Modi, H. Cable, M. Williamson, and V. Vedral, Quantum Correlations in Mixed-State Metrology, Phys. Rev. X **1**, 021022 (2011).

[15] S. A. Haine and S. S. Szigeti, Quantum metrology with mixed states: When recovering lost information is better than never losing it, Phys. Rev. A **92**, 032317 (2015).

[16] L. M. Pham, D. L. Sage, P. L. Stanwix, T. K. Yeung, D. Glenn, A. Trifonov, P. Cappellaro, P. R. Hemmer, M. D. Lukin, H. Park, A. Yacoby, and R. L. Walsworth, Magnetic field imaging with nitrogen-vacancy ensembles, New J. Phys. **13**, 045021 (2011).

[17] J. F. Barry, M. J. Turner, J. M. Schloss, D. R. Glenn, Y. Song, M. D. Lukin, H. Park, and R. L. Walsworth, Optical magnetic detection of single-neuron action potentials using quantum defects in diamond, Proc. Natl. Acad. Sci. U.S.A. **113**, 14133 (2016).

[18] I. M. Savukov and M. V. Romalis, Effects of spin-exchange collisions in a high-density alkali-metal vapor in low magnetic fields, Phys. Rev. A **71**, 023405 (2005).

[19] D. Budker and M. Romalis, Optical magnetometry, Nat. Phys. **3**, 227 (2007).

[20] S. Appelt, A. B. -A. Baranga, C. J. Erickson, M. V. Romalis, A. R. Young, and W. Happer, Theory of spin-exchange optical pumping of ^{3}He and ^{129}Xe, Phys. Rev. A **58**, 1412 (1998).

[21] J. Choi, S. Choi, G. Kucsko, P. C. Maurer, B. J. Shields, H. Sumiya, S. Onoda, J. Isoya, E. Demler, F. Jelezko, N. Y. Yao, and M. D. Lukin, Depolarization Dynamics in a Strongly Interacting Solid-State Spin Ensemble, Phys. Rev. Lett. **118**, 093601 (2017).

[22] N. A. Gershenfeld and I. L. Chuang, Bulk spin-resonance quantum computation, Science **275**, 350 (1997).

[23] J. A. Jones, S. D. Karlen, J. Fitzsimons, A. Ardavan, S. C. Benjamin, G. A. D. Briggs, and J. J. L. Morton, Magnetic field sensing beyond the standard quantum limit using 10-spin NOON states, Science **324**, 1166 (2009).

[24] S. Simmons, J. A. Jones, S. D. Karlen, A. Ardavan, and J. J. L. Morton, Magnetic field sensors using 13-spin cat states, Phys. Rev. A **82**, 022330 (2010).

[25] M. Schaffry, E. M. Gauger, J. J. L. Morton, J. Fitzsimons, S. C. Benjamin, and B. W. Lovett, Quantum metrology with molecular ensembles, Phys. Rev. A **82**, 042114 (2010).

[26] S. Boixo, S. T. Flammia, C. M. Caves, and J. M. Geremia, Generalized Limits for Single-Parameter Quantum Estimation, Phys. Rev. Lett. **98**, 090401 (2007).

[27] S. Pang and T. A. Brun, Quantum metrology for a general Hamiltonian parameter, Phys. Rev. A **90**, 022117 (2014).

[28] J. Liu, X.-X. Jing, and X. Wang, Quantum metrology with unitary parametrization processes, Sci. Rep. **5**, 8565 (2015).

[29] More generally, the eigenvectors of ρ^* may be written with a relative phase in the superpositions of $|h_k\rangle$ [$|\mu_k(0)\rangle$ in case of Theorem 2] such that the orthonormality condition remains fulfilled, i.e., $(|h_k\rangle + e^{i\varphi_k}|h_{d-k+1}\rangle)/\sqrt{2})$ if $2k < d+1$ and $(|h_k\rangle - e^{i\varphi_k}|h_{d-k+1}\rangle)/\sqrt{2})$ if $2k > d+1$, where the same applies for Theorem 2 when replacing the $|h_k\rangle$ by $|\mu_k(0)\rangle$.

[30] P. Bloomfield and G. S. Watson, The inefficiency of least squares, Biometrika **62**, 121 (1975).

[31] S. Drury, S. Liu, C.-Y. Lu, S. Puntanen, and G. P. Styan, Some comments on several matrix inequalities with applications to canonical correlations: historical background and recent developments, Sankhyā (The Indian Journal of Statistics) **64**, 453 (2002).

[32] See Supplemental Material at http://link.aps.org/supplemental/10.1103/PhysRevLett.123.250502 for proofs of Theorems 1 and 2, as well as the proofs of Heisenberg scaling for thermal states.

[33] J. M. E. Fraïsse and D. Braun, Enhancing sensitivity in quantum metrology by Hamiltonian extensions, Phys. Rev. A **95**, 062342 (2017).

[34] S. Pang and A. N. Jordan, Optimal adaptive control for quantum metrology with time-dependent Hamiltonians, Nat. Commun. **8**, 14695 (2017).

[35] Yu showed that *any* state ρ can be decomposed as $\sum_k u_k |U_k\rangle\langle U_k|$ with weights u_k and (generally nonorthonormal) pure states $|U_k\rangle$ such that the QFI equals $\sum_k u_k I_\alpha(|U_k\rangle\langle U_k|)$ [36,37]. For ρ^* in Eq. (4), with rank $r \leq (d+1)/2$, Yu's state decomposition of ρ^* is given by the eigendecomposition of ρ^*, $|U_k\rangle = |\phi_k\rangle$ and $u_k = p_k$. This is not the case for $r > (d+1)/2$.

[36] G. Tóth and D. Petz, Extremal properties of the variance and the quantum Fisher information, Phys. Rev. A **87**, 032324 (2013).

[37] S. Yu, Quantum Fisher information as the convex roof of variance, arXiv:1302.5311.

[38] A. W. Marshall, I. Olkin, and B. C. Arnold, *Inequalities: Theory of Majorization and Its Applications* (Springer, New York, 1979), Vol. 143.

[39] K. Fan, On a theorem of Weyl concerning eigenvalues of linear transformations I, Proc. Natl. Acad. Sci. U.S.A. **35**, 652 (1949).

[40] W. Fulton, Eigenvalues, invariant factors, highest weights, and Schubert calculus, Bull. Am. Math. Soc. **37**, 209 (2000).

[41] S. Schmitt, T. Gefen, F. M. Stürner, T. Unden, G. Wolff, C. Müller, J. Scheuer, B. Naydenov, M. Markham, S. Pezzagna, J. Meijer, I. Schwarz, M. Plenio, A. Retzker, L. P. McGuinness, and F. Jelezko, Submillihertz magnetic spectroscopy performed with a nanoscale quantum sensor, Science **356**, 832 (2017).

[42] The optimal control Hamiltonian of Pang *et al.* [34] fulfills exactly the condition in Eq. (9) which makes it optimal not only for pure but also for mixed states. For pure states, control Hamiltonians that ensure $U_\alpha(t)|\mu_i(0)\rangle = |\mu_i(t)\rangle$ only for $i = 1, d$ would have been sufficient because only μ_1 and μ_d contribute to the upper bound.

[43] S. Choi, N. Y. Yao, and M. D. Lukin, Quantum metrology based on strongly correlated matter, arXiv:1801.00042.

[44] N. De Zanche, C. Barmet, J. A. Nordmeyer-Massner, and K. P. Pruessmann, NMR probes for measuring magnetic fields and field dynamics in MR systems, Magn. Reson. Med. **60**, 176 (2008).

[45] J. Scheuer, I. Schwartz, S. Müller, Q. Chen, I. Dhand, M. B. Plenio, B. Naydenov, and F. Jelezko, Robust techniques for polarization and detection of nuclear spin ensembles, Phys. Rev. B **96**, 174436 (2017).

[46] D. Pagliero, A. Laraoui, J. D. Henshaw, and C. A. Meriles, Recursive polarization of nuclear spins in diamond at arbitrary magnetic fields, Appl. Phys. Lett. **105**, 242402 (2014).

[47] M. Tsang, H. M. Wiseman, and C. M. Caves, Fundamental Quantum Limit to Waveform Estimation, Phys. Rev. Lett. **106**, 090401 (2011).

[48] D. W. Berry, M. Tsang, M. J. W. Hall, and H. M. Wiseman, Quantum Bell-Ziv-Zakai Bounds and Heisenberg Limits for Waveform Estimation, Phys. Rev. X **5**, 031018 (2015).

[49] J. V. Uspensky, *Introduction to Mathematical Probability* (McGraw-Hill Book Company, New York, 1937).

[50] M. J. Holland and K. Burnett, Interferometric Detection of Optical Phase Shifts at the Heisenberg Limit, Phys. Rev. Lett. **71**, 1355 (1993).

[51] M. Zwierz, C. A. Pérez-Delgado, and P. Kok, General Optimality of the Heisenberg Limit for Quantum Metrology, Phys. Rev. Lett. **105**, 180402 (2010).

[52] S. F. Huelga, C. Macchiavello, T. Pellizzari, A. K. Ekert, M. B. Plenio, and J. I. Cirac, Improvement of Frequency Standards with Quantum Entanglement, Phys. Rev. Lett. **79**, 3865 (1997).

[53] J. Kolodynski, Precision bounds in noisy quantum metrology, arXiv:1409.0535.

[54] B. M. Escher, R. L. de Matos Filho, and L. Davidovich, General framework for estimating the ultimate precision limit in noisy quantum-enhanced metrology, Nat. Phys. **7**, 406 (2011).

Supplemental material for 'Maximal quantum Fisher information for mixed states'

Lukas J. Fiderer[1], Julien M. E. Fraïsse[2], Daniel Braun[1]

[1]*Eberhard-Karls-Universität Tübingen,*

Institut für Theoretische Physik, 72076 Tübingen, Germany

[2]*Seoul National University, Department of Physics and Astronomy,*

Center for Theoretical Physics, 151-747 Seoul, Korea
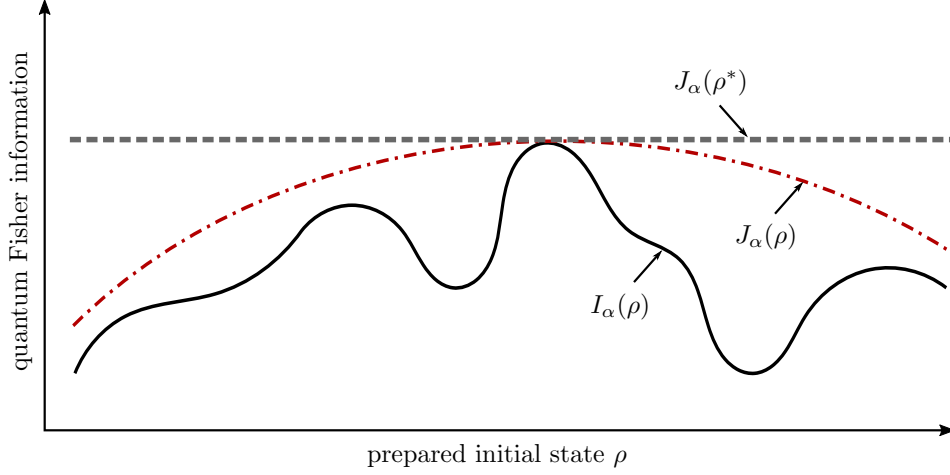
I. PROOF OF THEOREM 1

FIG. 1. Schematic sketch of the mechanism used to prove theorem 1 from the Letter. First an upper bound $J_\alpha(\rho)$ (red dash-dotted line) for the quantum Fisher information $I_\alpha(\rho)$ (black solid line) is constructed. This upper bound is shown to be maximal for $\rho = \rho^*$ (gray dashed line). Then, it is shown that $I_\alpha(\rho^*) = J_\alpha(\rho^*)$ from which it follows that $I_\alpha(\rho^*)$ must be the maximum of $I_\alpha(\rho)$.

The idea of the proof of theorem 1 from the Letter is the following, see also Fig. 1: We carefully construct an upper bound $J_\alpha(\rho) \geq I_\alpha(\rho)$ for the QFI $I_\alpha(\rho)$. Then, we show that (i) $J_\alpha(\rho)$ is maximized by setting $\rho = \rho^*$ and (ii) $J_\alpha(\rho^*) = I_\alpha(\rho^*)$. It follows that $I_\alpha(\rho^*)$ is the maximum of $I_\alpha(\rho)$.

We first give a technical lemma which introduces inequalities for the $p_{i,j}$ coefficients which are defined as

$$p_{i,j} := \begin{cases} 0 & \text{if } p_i = p_j = 0, \\ \frac{(p_i - p_j)^2}{p_i + p_j} & \text{else.} \end{cases} \tag{1}$$

These inequalities will be used to prove proposition I.1 about the existence of coefficients $q_{i,j}$ which fulfill specific conditions. Proposition I.1 enables us to find the desired upper bound $J_\alpha(\rho)$ for the QFI $I_\alpha(\rho)$. This is then used in the proof of theorem I.1 which corresponds to theorem 1 from the Letter.

To facilitate the understanding of the following lemma and proposition, we introduce a schematic arrangement of a set of coefficients $p_{i,j}$, see Fig. 2. We consider only coefficients with $1 \leq i < j \leq d$ because of the symmetry $p_{i,j} = p_{j,i}$ and because $p_{i,i} = 0$.

$$\begin{array}{cccccccc}
p_{1,2} & & p_{2,3} & p_{3,4} & p_{4,5} & p_{5,6} & p_{6,7} \\
& p_{1,3} & p_{2,4} & \boxed{p_{3,5}} & p_{4,6} & p_{5,7} \\
& & p_{1,4} & p_{2,5} & p_{3,6} & p_{4,7} \\
& & & p_{1,5} & \boxed{p_{2,6}} & p_{3,7} \\
& & & & p_{1,6} & p_{2,7} \\
& & & & & \boxed{p_{1,7}}
\end{array}$$

FIG. 2. Scheme of $p_{i,j}$ for $1 \leq i < j \leq d = 7$. Coefficients inside the red squared boxes are denoted as *central coefficients*.

Lemma I.1. *Let $p_1 \geq \cdots \geq p_d \geq 0$. Then, the following inequalities hold:*

$$(i) \qquad p_{i,l} \geq p_{i,j} + p_{j,l} \qquad \text{for } 1 \leq i < j < l \leq d,$$

$$(ii) \quad p_{i,l} - p_{i+1,l} \geq p_{i,k} - p_{i+1,k} \quad \text{for } 1 < i + 1 < k < l \leq d,$$

$$(iii) \quad p_{i,l} - p_{i,l-1} \geq p_{j,l} - p_{j,l-1} \quad \text{for } 1 \leq i < j < l - 1 < d.$$

Proof. First we prove that

$$p_{i,l} + p_{j,k} \geq p_{i,k} + p_{j,l} \quad \text{for } 1 \leq i < j < k < l \leq d. \tag{2}$$

If $p_i \geq p_j = p_k = p_l = 0$, inequality (2) holds trivially. Otherwise, we find

$$p_{i,l} + p_{j,k} - p_{i,k} - p_{j,l} = \frac{4(p_i - p_j)(p_k - p_l)(p_i p_j p_k + p_j p_k p_l + p_i(p_j + p_k)p_l)}{(p_i + p_k)(p_j + p_k)(p_i + p_l)(p_j + p_l)}, \tag{3}$$

which is clearly nonnegative because all factors in the denominator are positive and all factors in the numerator are nonnegative. This proves inequality (2).

Inequalities (i), (ii), and (iii) from the lemma are special cases of inequality (2): If $p_j = p_k$, inequality (2) holds also for $j = k$ and it follows inequality (i). Further, from inequality (2) we find $p_{i,l} - p_{j,l} \geq p_{i,k} - p_{j,k}$ which for $j = i + 1$ gives inequality (ii), and we find $p_{i,l} - p_{i,k} \geq p_{j,l} - p_{j,k}$ which for $k = l - 1$ gives inequality (iii). $\qquad \square$

In analogy to the coefficients $p_{i,j}$, we introduce another set of coefficients defined by

$$q_{i,j} := \sum_{k=i}^{j-1} q_{k,k+1}, \tag{4}$$

for $i < j$. This means that the set of coefficients $\{q_{i,j}\}$ is fully defined by the coefficients $q_{i,i+1}$ with $i = 1, \ldots, d - 1$.

3

Proposition I.1. *For any dimension $d \geq 2$ and for any $p_1 \geq \cdots \geq p_d \geq 0$, there exist coefficients $q_{k,k+1} \geq 0$ with $1 \leq k \leq d-1$ such that for $1 \leq i < j \leq d$:*

$$q_{i,j} = p_{i,j} \quad \text{if} \quad j = d - i + 1 \qquad \text{(central coefficients)}, \tag{5}$$

$$q_{i,j} \geq p_{i,j} \quad \text{else}, \tag{6}$$

where coefficients $p_{i,j}$ and $q_{i,j}$ are defined in Eqs. (1) and (4), respectively.

Proof. The proof works by induction in dimension d, once for even d and once for odd d.

Even dimension d

Base case $d = 2$: There is only one coefficient $p_{i,j}$ with $1 \leq i < j \leq 2$, which is $p_{1,2}$. The proposition for $d = 2$ holds because $q_{1,2} := p_{1,2}$ fulfills conditions (5) and (6) trivially.

Inductive step: Suppose the proposition holds for $d = n$. We will prove the proposition for $d = n + 2$.

First, the induction hypothesis is applied to n coefficients $p_2, \ldots, p_{n+1}$: For any $p_2 \geq \cdots \geq p_{n+1} \geq 0$, there exist coefficients $q_{k,k+1} \geq 0$ for $2 \leq k \leq n$ such that for $2 \leq i < j \leq n + 1$:

$$q_{i,j} = p_{i,j} \quad \text{if} \quad j = n - i + 3 \qquad \text{(central coefficients)}, \tag{7}$$

$$q_{i,j} \geq p_{i,j} \quad \text{else}. \tag{8}$$

Second, we show that for any p_1 and p_{n+2} with $p_1 \geq p_2$ and $p_{n+1} \geq p_{n+2} \geq 0$ there exist two further coefficients $q_{1,2}$ and $q_{n+1,n+2}$ such that

$$q_{1,n+2} = p_{1,n+2} \quad \text{(central coefficients)}, \tag{9}$$

$$q_{1,j} \geq p_{1,j} \quad \text{for } j = 2, \ldots, n + 1 \quad \text{(left flank)}, \tag{10}$$

$$q_{i,n+2} \geq p_{i,n+2} \quad \text{for } i = 2, \ldots, n + 1 \quad \text{(right flank)}. \tag{11}$$

A graphical visualization of the inductive step is shown in Fig. 3 which explains the terms left flank and right flank used to designate the inequalities above. The existence of $q_{1,2}$ and $q_{n+1,n+2}$ such that conditions (9),(10), and (11) hold is shown explicitly by setting

$$q_{1,2} := p_{1,n+2} - p_{2,n+2}, \tag{12}$$

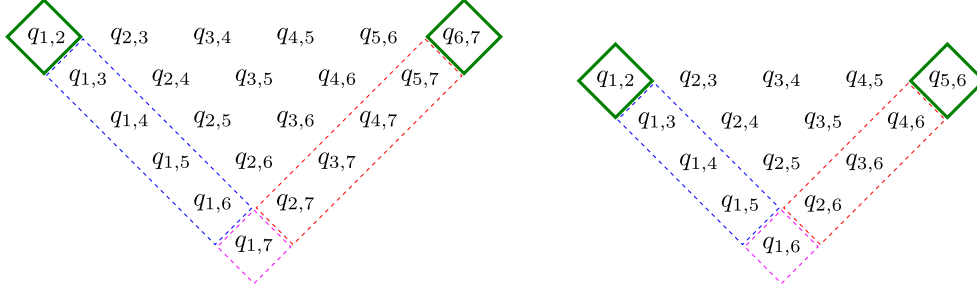$$q_{n+1,n+2} := p_{2,n+2} - p_{2,n+1}, \tag{13}$$

FIG. 3. Recursion steps from $d = 5$ to $d = 7$ (left) and from $d = 4$ to $d = 6$ (right). In the green squares are the two new elements we need to choose. In the blue (resp. red) rectangles are the new left (resp. right) flanks that need to fulfill conditions (6) ; in the magenta squares are the new central coefficients that need to fulfill condition (5).

and checking conditions (9),(10), and (11): We find

$$q_{1,n+2} = q_{1,2} + q_{2,n+1} + q_{n+1,n+2} \qquad\qquad\qquad\text{[Eq. (4)]}$$
$$= p_{1,n+2} - p_{2,n+2} + p_{2,n+1} + p_{2,n+2} - p_{2,n+1} \quad\text{[Eqs. (12),(13), and Eq. (7) for } i = 2\text{]}$$
$$= p_{1,n+2}$$

which fulfills the condition for central coefficients [condition (9)]. Further, for $j = 3, \ldots, n+1$:

$$q_{1,j} = q_{1,2} + q_{2,j} \qquad\qquad\qquad\qquad\text{[Eq. (4)]}$$
$$\geq p_{1,n+2} - p_{2,n+2} + p_{2,j} \qquad\qquad\text{[Eq. (12) and inequality (8)]}$$
$$\geq p_{1,j} - p_{2,j} + p_{2,j} \qquad\qquad\qquad\text{[lemma I.1 } (ii)\text{]}$$
$$= p_{1,j},$$

and

$$q_{1,2} = p_{1,n+2} - p_{2,n+2} \qquad\qquad\qquad\text{[Eq. (12)]}$$
$$\geq p_{1,2} + p_{2,n+2} - p_{2,n+2} \qquad\qquad\text{[lemma I.1 } (i)\text{]}$$
$$= p_{1,2},$$

which fulfill the conditions for the left flank [condition (10)]. The proof for the right flank

5

is similar: For $i = 2, \ldots, n$:

$$q_{i,n+2} = q_{i,n+1} + q_{n+1,n+2} \qquad\qquad \text{[Eq. (4)]}$$

$$\geq p_{i,n+1} + p_{2,n+2} - p_{2,n+1} \qquad \text{[Eq. (13) and inequality (8)]}$$

$$\geq p_{i,n+1} + p_{i,n+2} - p_{i,n+1} \qquad\qquad \text{[lemma I.1 } (iii)\text{]}$$

$$= p_{i,n+2},$$

and

$$q_{n+1,n+2} = p_{2,n+2} - p_{2,n+1} \qquad\qquad \text{[Eq. (13)]}$$

$$\geq p_{2,n+1} + p_{n+1,n+2} - p_{2,n+1} \qquad \text{[lemma I.1 } (i)\text{]}$$

$$= p_{n+1,n+2},$$

which fulfill the conditions for the right flank [condition (11)]. This proves the proposition for $d = n + 2$, concluding the proof by induction for even dimensions.

Odd dimension d

Base case d=3: There are only three coefficients $p_{i,j}$ with $1 \leq i < j \leq 3$, which are $p_{1,2}, p_{2,3}$, and $p_{1,3}$. The proposition for $d = 3$ holds because $q_{1,2} \coloneqq p_{1,3} - p_{2,3}$, $q_{2,3} \coloneqq p_{2,3}$, and $q_{1,3} = q_{1,2} + q_{2,3}$ fulfill the conditions (5) and (6): $q_{1,2} = p_{1,3} - p_{2,3} \geq p_{1,2} + p_{2,3} - p_{2,3} = p_{1,2}$ where inequality (i) from lemma I.1 was used, while the other conditions hold trivially.

Inductive step: Analog to the inductive step for even d. $\qquad\qquad\square$

Equipped with proposition I.1 we can prove theorem 1 from the Letter:

Theorem I.1. *For any state ρ and any generator h_α with ordered eigenvalues $p_1 \geq \cdots \geq p_d$ and $h_1 \geq \cdots \geq h_d$, respectively, the maximal QFI with respect to all unitary state preparations $U\rho U^\dagger$, $U \in \mathrm{U}(d)$, is given by*

$$I_\alpha^* \coloneqq \max_U I_\alpha(U\rho U^\dagger) = \frac{1}{2} \sum_{k=1}^d p_{k,d-k+1}(h_k - h_{d-k+1})^2. \qquad (14)$$

Let $|h_k\rangle$ be the eigenvectors of the generator, $h_\alpha |h_k\rangle = h_k |h_k\rangle$. The maximum I_α^* is obtained by preparing the initial state

$$\rho^* \coloneqq \sum_{k=1}^d p_k |\phi_k\rangle \langle\phi_k| \qquad (15)$$

6

with

$$
|\phi_k\rangle := \begin{cases} \frac{|h_k\rangle + e^{i\chi_k}|h_{d-k+1}\rangle}{\sqrt{2}} & \text{if } 2k < d+1, \\[2mm] |h_k\rangle & \text{if } 2k = d+1, \\[2mm] \frac{|h_k\rangle - e^{i\chi_k}|h_{d-k+1}\rangle}{\sqrt{2}} & \text{if } 2k > d+1. \end{cases} \tag{16}
$$

where χ_k are arbitrary real phases (the theorem as formulated in the Letter is recovered by setting $\chi_k = 0$).

Proof. First we reformulate the optimization problem in a more convenient way:

The unitary state preparation $U\rho U^\dagger$ has invariant eigenvalues for all $U \in \mathrm{U}(d)$. However, the unitary freedom $U \in \mathrm{U}(d)$ allows one to change the basis from the ordered orthonormal basis of eigenvectors $(|\psi_i\rangle)_{i=1}^d$ of ρ, where $\rho|\psi_i\rangle = p_i|\psi_i\rangle$, to any other ordered orthonormal basis. Therefore, the optimization problem with respect to unitary transformations $U \in \mathrm{U}(d)$ on the state ρ is equivalent to optimizing over ordered bases $B \in S$ where

$$
S := \{(|\xi_i\rangle)_{i=1}^d : \langle\xi_i|\xi_j\rangle = \delta_{i,j} \ \forall i, j \in \{1, \ldots, d\}\}. \tag{17}
$$

Note that the ordering of eigenvectors corresponds to the ordering of eigenvalues p_i which plays a crucial role in the theorem. The basis corresponding to ρ^* is given by $B^* = (|\phi_i\rangle)_{i=1}^d$, and the maximization in Eq. (14) is equivalent to

$$
I_\alpha^* := \max_{B \in S} I_\alpha(B), \tag{18}
$$

where the QFI was redefined as a function of B:

$$
I_\alpha(B) = 2 \sum_{i,j=1}^d p_{i,j} |[h_\alpha(B)]_{i,j}|^2. \tag{19}
$$

The coefficients $p_{i,j}$ are defined in Eq. (1) with respect to the eigenvalues p_i and $[h_\alpha(B)]_{i,j} = \langle\xi_i|h_\alpha|\xi_j\rangle$ are the coefficients of h_α with respect to $B = (|\xi_i\rangle)_{i=1}^d$.

In order to prove that the maximum is reached by B^*, we introduce an upper bound for the QFI. We start by rewriting the QFI, exploiting the symmetries $p_{i,j} = p_{j,i}$ and $\left|[h_\alpha(B)]_{i,j}\right|^2 = \left|[h_\alpha(B)]_{j,i}\right|^2$:

$$
I_\alpha(B) = 2 \sum_{i,j=1}^d p_{i,j} \left|[h_\alpha(B)]_{i,j}\right|^2 \tag{20}
$$

$$
= 4 \sum_{i=1}^{d-1} \sum_{j=i+1}^d p_{i,j} \left|[h_\alpha(B)]_{i,j}\right|^2. \tag{21}
$$

7

Then, an upper bound for $I_\alpha(B)$ is obtained by replacing coefficients $p_{i,j}$ in Eq. (21) with new coefficients $q_{i,j} \geq p_{i,j}$ for all $1 \leq i < j \leq d$:

$$I_\alpha(B) \leq J_\alpha(B) \coloneqq 4 \sum_{i=1}^{d-1} \sum_{j=i+1}^{d} q_{i,j} \left| [h_\alpha(B)]_{i,j} \right|^2, \tag{22}$$

where $J_\alpha(B)$ denotes the upper bound. We choose coefficients $q_{i,j}$ according to proposition I.1, i.e., besides $q_{i,j} \geq p_{i,j}$ they fulfill $p_{i,j} = q_{i,j}$ for $j = d - i + 1$ and $q_{i,j} = \sum_{k=i}^{j-1} q_{k,k+1}$ for all $1 \leq i < j \leq d$. We rewrite the upper bound $J_\alpha(B)$:

$$J_\alpha(B) = 4 \sum_{i=1}^{d-1} \sum_{j=i+1}^{d} q_{i,j} \left| [h_\alpha(B)]_{i,j} \right|^2 \tag{23}$$

$$= 4 \sum_{i=1}^{d-1} \sum_{j=i+1}^{d} \sum_{k=i}^{j-1} q_{k,k+1} \left| [h_\alpha(B)]_{i,j} \right|^2 \tag{24}$$

$$= 4 \sum_{k=1}^{d-1} q_{k,k+1} \sum_{i=1}^{k} \sum_{j=k+1}^{d} \left| [h_\alpha(B)]_{i,j} \right|^2 \tag{25}$$

$$= 4 \sum_{k=1}^{d-1} q_{k,k+1} \left\| h_\alpha(B,k) \right\|_2^2, \tag{26}$$

where $h_\alpha(B,k)$ denotes the subblock of $h_\alpha(B)$ with coefficients from the 1st to the kth row and from the $(k+1)$th to the dth column, and $\|\cdot\|_2^2$ denotes the Hilbert–Schmidt norm which is defined for a $m \times n$ matrix A as $\|A\|_2^2 \coloneqq \mathrm{tr}\left[A^\dagger A\right] = \sum_{i,j=1}^{m,n} |A_{i,j}|^2$. Since $h_\alpha(B)$ is Hermitian it divides in subblocks as

$$h_\alpha(B) = \begin{pmatrix} \bullet & h_\alpha(B,k) \\ h_\alpha^\dagger(B,k) & \bullet \end{pmatrix}, \tag{27}$$

where the quadratic subblocks on the diagonal are not further specified.

Next, we maximize the upper bound $J_\alpha(B)$ and show that it equals the QFI at its maximum. In order to maximize $J_\alpha(B)$, we use the Bloomfield–Watson inequality [1] on the Hilbert–Schmidt norm of off-diagonal blocks such as $h_\alpha(B,k)$. We take a convenient formulation of the inequality from Ref.[2, Eqs. (1.14) and (4.3)] and apply it to $h_\alpha(B,k)$:

$$\left\| h_\alpha(B,k) \right\|_2^2 \leq \frac{1}{4} \sum_{i=1}^{m(k)} (h_i - h_{d-i+1})^2, \tag{28}$$

where $m(k) = \min(k, d - k)$. We evaluate the left-hand side of the Bloomfield–Watson

inequality (28) for $B = B^*$, where B^* is the eigenbasis of ρ^*, defined above Eq. (18):

$$\|h_\alpha(B^*, k)\|_2^2 = \sum_{i=1}^{k} \sum_{j=k+1}^{d} \left| [h_\alpha(B^*)]_{i,j} \right|^2 \tag{29}$$

$$= \sum_{i=1}^{k} \sum_{j=k+1}^{d} \left| \langle \phi_i | h_\alpha | \phi_j \rangle \right|^2 \tag{30}$$

$$= \sum_{i=1}^{k} \sum_{j=k+1}^{d} \left(\delta_{i,j} \frac{h_i + h_{d-i+1}}{2} + \delta_{i,d-j+1} \frac{|h_i - h_{d-i+1}|}{2} \right)^2 \tag{31}$$

$$= \frac{1}{4} \sum_{i=1}^{m(k)} (h_i - h_{d-i+1})^2, \tag{32}$$

where we used the definition of $|\phi_i\rangle$ [Eq. (16)] to get from Eq. (30) to (31). In Eq. (31), the first summand (within the brackets) evaluates always to zero while the second summand is nonzero in $m(k)$ cases as given in Eq. (32). Note, that Eq. (32) equals the right-hand side of inequality (28). Therefore, the Bloomfield–Watson inequality (28) is saturated for $B = B^*$ and, in particular, $\|h_\alpha(B, k)\|_2^2 \le \|h_\alpha(B^*, k)\|_2^2$ for all $B \in S$.

This implies $J_\alpha(B) \le J_\alpha(B^*)$ for all $B \in S$ which can be seen from Eq. (26) and by realizing that the coefficients $q_{i,j}$ in $J_\alpha(B)$ are nonnegative, which follows from the nonnegativity of $p_{i,j}$. Thus, $J_\alpha(B^*)$ is the maximum of $J_\alpha(B)$ with respect to B.

Now, we show that $J_\alpha(B^*) = I_\alpha(B^*)$ starting from the definition of $J_\alpha(B)$ in Eq. (22):

$$J_\alpha(B^*) = 4 \sum_{i=1}^{d-1} \sum_{j=i+1}^{d} q_{i,j} \left(\delta_{i,j} \frac{h_i + h_{d-i+1}}{2} + \delta_{i,d-j+1} \frac{h_i - h_{d-i+1}}{2} \right)^2 \tag{33}$$

$$= \sum_{i=1}^{d-1} \sum_{j=i+1}^{d} q_{i,j} \delta_{i,d-j+1} (h_i - h_{d-i+1})^2 \tag{34}$$

$$= \frac{1}{2} \sum_{i=1}^{d} p_{i,i-d+1} (h_i - h_{d-i+1})^2 = I_\alpha(B^*), \tag{35}$$

where we used $q_{i,i-d+1} = p_{i,i-d+1}$ and, to get from Eq. (34) to (35), we first came back to a summation over all $1 \le i, j \le d$ before evaluating $\delta_{i,d-j+1}$ which explains the factor $1/2$ in Eq. (35).

It follows from $J_\alpha(B) \ge I_\alpha(B) \ \forall B \in S$ that $\max_{B \in S} J_\alpha(B) \ge \max_{B \in S} I_\alpha(B)$, and, then, it follows from $\max_{B \in S} J_\alpha(B) = I_\alpha(B^*)$ that $I_\alpha(B^*)$ is the maximum of $I_\alpha(B)$ with respect to $B \in S$. $\quad\square$

II.   PROOF OF THEOREM 2

Let us first introduce some notation. The real, nonnegative coordinate space of d dimensions is denoted by $\mathbb{R}_+^d$. For two vectors $\boldsymbol{x}, \boldsymbol{y} \in \mathbb{R}_+^d$, the element-wise vector ordering $x_i \le y_i$

9

for all $i \in \{1, \ldots, d\}$ is denoted as $\boldsymbol{x} \leq \boldsymbol{y}$. For any $\boldsymbol{x} \in \mathbb{R}_+^d$, let $x_{[1]}, \ldots, x_{[d]}$ be the components of $\boldsymbol{x}$ in decreasing order, and let

$$\boldsymbol{x}_\downarrow \coloneqq (x_{[1]}, \ldots, x_{[d]}) \tag{36}$$

denote the decreasing rearrangement of $\boldsymbol{x}$. Let

$$\mathcal{D}_+^d \coloneqq \{(x_1, \ldots, x_d) : x_1 \geq \cdots \geq x_d \geq 0\} \tag{37}$$

be the set of decreasing rearrangements of elements from $\mathbb{R}_+^d$.

Definition II.1. For a hermitian matrix X with eigenvalues $x_1 \geq x_2 \geq \cdots \geq x_d$ define

$$\boldsymbol{d}(X) \coloneqq (x_1 - x_d, x_2 - x_{d-1} \ldots, x_{\lceil d/2 \rceil} - x_{d - \lceil d/2 \rceil + 1}), \tag{38}$$

where $\lceil d/2 \rceil$ denotes the smallest integer j with $j \geq d/2$.

Note that the entries of $\boldsymbol{d}(X)$ are nonnegative and in decreasing order, i.e., $\boldsymbol{d}(X) \in \mathcal{D}_+^{\lceil d/2 \rceil}$.

Definition II.2. Let $\boldsymbol{x}, \boldsymbol{y} \in \mathbb{R}_+^d$. We say that $\boldsymbol{x}$ is weakly majorized by $\boldsymbol{y}$, denoted by $\boldsymbol{x} \prec_w \boldsymbol{y}$, if

$$\sum_{i=1}^k x_{[i]} \leq \sum_{i=1}^k y_{[i]} \quad \forall k = 1, \ldots, d. \tag{39}$$

Lemma II.1. *Let A, B, and $C = A + B$ be hermitian matrices with eigenvalues $a_1 \geq \cdots \geq a_d$, $b_1 \geq \cdots \geq b_d$, and $c_1 \geq \cdots \geq c_d$, respectively. Then, $\boldsymbol{d}(C) \prec_w \boldsymbol{d}(A) + \boldsymbol{d}(B)$.*

Proof. The inequalities of K. Fan (see for instance [3, eq.3]) for the eigenvalues of A, B, and $C = A + B$ are

$$\sum_{i=1}^r c_i \leq \sum_{i=1}^r a_i + b_i \quad \forall r = 1, \ldots, d - 1. \tag{40}$$

Subtracting them from the trace condition

$$\sum_{i=1}^d c_i = \sum_{i=1}^d a_i + b_i \tag{41}$$

and rearranging the indices gives

$$\sum_{i=1}^r c_{d-i+1} \geq \sum_{i=1}^r a_{d-i+1} + b_{d-i+1} \quad \forall r = 1, \ldots, d - 1. \tag{42}$$

Subtracting inequality (42) from inequality (40) gives

$$\sum_{i=1}^r c_i - c_{d-i+1} \leq \sum_{i=1}^r a_i - a_{d-i+1} + b_i - b_{d-i+1} \quad \forall r = 1, \ldots, d - 1, \tag{43}$$

which are for $r = 1, \ldots, \lceil d/2 \rceil$ the weak majorization conditions for $\boldsymbol{d}(C) \prec_w \boldsymbol{d}(A) + \boldsymbol{d}(B)$. $\quad\square$

Definition II.3. For any $\boldsymbol{p} \in \mathcal{D}_+^d$ define

$$\phi_{\boldsymbol{p}} : \mathbb{R}_+^d \to \mathbb{R}, \phi_{\boldsymbol{p}}(\boldsymbol{x}) \coloneqq \sum_{i=1}^d p_i x_{[i]}^2. \tag{44}$$

Lemma II.2. *For any $\boldsymbol{p} \in \mathcal{D}_+^d$, $\phi_{\boldsymbol{p}}$ is increasing and Schur convex on $\mathbb{R}_+^d$, i.e., the following conditions hold [4, part I,ch.3,A.4]:*

 (i) $\boldsymbol{x} \le \boldsymbol{y} \Rightarrow \phi_{\boldsymbol{p}}(\boldsymbol{x}) \le \phi_{\boldsymbol{p}}(\boldsymbol{y})$ *(increasing),*

 (ii) $\phi_{\boldsymbol{p}}(\boldsymbol{x})$ *is invariant under permutation of coefficients of $\boldsymbol{x}$ for any $\boldsymbol{x} \in \mathbb{R}_+^d$ (symmetric),*

 (iii) $(x_i - x_j) \left(\frac{\partial \phi_{\boldsymbol{p}}(\boldsymbol{x})}{\partial x_i} - \frac{\partial \phi_{\boldsymbol{p}}(\boldsymbol{x})}{\partial x_j} \right) \ge 0 \ \forall \boldsymbol{x} \in \mathbb{R}_+^d$ *and $\forall i \ne j$ (Schur's condition).*

Proof. From $\boldsymbol{x} \le \boldsymbol{y}$ it follows that $x_{[i]} \le y_{[i]} \ \forall i$, which implies $p_i x_{[i]}^2 \le p_i y_{[i]}^2 \ \forall i$ for any $p_i \ge 0$. Finally it follows $\sum_i p_i x_{[i]}^2 \le \sum_i p_i y_{[i]}^2$ which proves condition (i). Condition (ii) follows directly from the definition of $\phi_{\boldsymbol{p}}$. Finally, we have

$$(x_i - x_j) \left(\frac{\partial \phi_{\boldsymbol{p}}(\boldsymbol{x})}{\partial x_i} - \frac{\partial \phi_{\boldsymbol{p}}(\boldsymbol{x})}{\partial x_j} \right) = (x_i - x_j) 2(q x_i - r x_j), \tag{45}$$

where q, r are some components of $\boldsymbol{p}$ with $q \ge r$ if $x_i \ge x_j$ and $q \le r$ if $x_i \le x_j$ due to the definition of $\phi_{\boldsymbol{p}}$. It follows condition (iii). $\qquad\square$

Lemma II.3. *Let A, B, and $C = A + B$ be Hermitian matrices. For any $\boldsymbol{p} \in \mathcal{D}_+^d$,*

$$\boldsymbol{d}(C) \prec_w \boldsymbol{d}(A) + \boldsymbol{d}(B) \ \Rightarrow \ \phi_{\boldsymbol{p}}(\boldsymbol{d}(C)) \le \phi_{\boldsymbol{p}}(\boldsymbol{d}(A) + \boldsymbol{d}(B)). \tag{46}$$

Proof. The proof follows from a theorem given in Ref. [4, part I,ch.3,A.8] about weak majorization and lemma II.2. $\qquad\square$

We are now ready to prove the following inequality:

Lemma II.4. *Let $\boldsymbol{p} \in \mathcal{D}_+^d$, and let $p_{i,j}$ be defined as in Eq. (1) for the components of $\boldsymbol{p}$. Let A, B, and $C = A + B$ be Hermitian matrices with eigenvalues $a_1 \ge \cdots \ge a_d$, $b_1 \ge \cdots \ge b_d$, and $c_1 \ge \cdots \ge c_d$, respectively. Then,*

$$\sum_{i=1}^d p_{i,d-i+1} (c_i - c_{d-i+1})^2 \le \sum_{i=1}^d p_{i,d-i+1} \left(a_i - a_{d-i+1} + b_i - b_{d-i+1} \right)^2. \tag{47}$$

11

Proof. Let us first show that coefficients $p_{i,d-i+1}$ satisfy

$$(p_{i,d-i+1})_{i=1}^{\lceil d/2 \rceil} \in \mathcal{D}_+^{\lceil d/2 \rceil}. \tag{48}$$

For $1 \leq i < \lfloor d/2 \rfloor$, where $\lfloor d/2 \rfloor$ denotes the largest integer j with $j \leq d/2$, we have

$$p_{i,d-i+1} \geq p_{i,i+1} + p_{i+1,d-i+1} \geq p_{i,i+1} + p_{i+1,d-i} + p_{d-i,d-i+1}, \tag{49}$$

where inequality (i) from lemma I.1 was applied twice, and it follows $p_{i,d-i+1} \geq p_{i+1,d-i}$. For even d it follows Eq. (48). For odd d, we further have $p_{\lfloor d/2 \rfloor,d-\lfloor d/2 \rfloor+1} \geq p_{\lceil d/2 \rceil,d-\lceil d/2 \rceil+1}$ because $p_{\lceil d/2 \rceil,d-\lceil d/2 \rceil+1} = p_{\lceil d/2 \rceil,\lceil d/2 \rceil} = 0$ by definition of $p_{i,j}$. This proves Eq. (48).

Together with lemmata II.1 and II.3 it follows that

$$\sum_{i=1}^{\lceil d/2 \rceil} p_{i,d-i+1}(c_i - c_{d-i+1})^2 \leq \sum_{i=1}^{\lceil d/2 \rceil} p_{i,d-i+1} \left(a_i - a_{d-i+1} + b_i - b_{d-i+1} \right)^2, \tag{50}$$

which, due to the symmetries $p_{i,d-i+1} = p_{d-i+1,i}$ and $(c_i - c_j)^2 = (c_j - c_i)^2$, is equivalent to

$$\sum_{i=d-\lceil d/2 \rceil+1}^{d} p_{i,d-i+1}(c_i - c_{d-i+1})^2 \leq \sum_{i=d-\lceil d/2 \rceil+1}^{d} p_{i,d-i+1} \left(a_i - a_{d-i+1} + b_i - b_{d-i+1} \right)^2. \tag{51}$$

Adding inequalities (50) and (51) proves the lemma since, in case of odd d, $p_{\lceil d/2 \rceil,\lceil d/2 \rceil} = 0$. $\quad\square$

We are now in the position to prove theorem 2 from the Letter:

Theorem II.1. *For any state ρ with ordered eigenvalues $p_1 \geq \cdots \geq p_d$ and any time-dependent Hamiltonian $H_\alpha(t)$, where $\mu_1(t) \geq \cdots \geq \mu_d(t)$ are the ordered eigenvalues of $\partial_\alpha H_\alpha(t) \coloneqq \partial H_\alpha(t)/\partial\alpha$, an upper bound for the QFI is given by*

$$K_\alpha = \frac{1}{2} \sum_{k=1}^{d} p_{k,d-k+1} \left(\int_0^T [\mu_k(t) - \mu_{d-k+1}(t)]\mathrm{d}t \right)^2. \tag{52}$$

Let $|\mu_k(t)\rangle$ be the time-dependent eigenvectors of $\partial_\alpha H_\alpha(t)$, $\partial_\alpha H_\alpha(t)|\mu_k(t)\rangle = \mu_k(t)|\mu_k(t)\rangle$. The upper bound K_α is reached by preparing the initial state

$$\rho^* = \sum_{k=1}^{d} p_k |\phi_k\rangle \langle\phi_k|, \tag{53}$$

with

$$|\phi_k\rangle = \begin{cases} \frac{|\mu_k(0)\rangle + e^{\mathrm{i}\chi_k}|\mu_{d-k+1}(0)\rangle}{\sqrt{2}} & \text{if } 2k < d+1, \\ |\mu_k(0)\rangle & \text{if } 2k = d+1, \\ \frac{|\mu_k(0)\rangle - e^{\mathrm{i}\chi_k}|\mu_{d-k+1}(0)\rangle}{\sqrt{2}} & \text{if } 2k > d+1, \end{cases} \tag{54}$$

where χ_k are arbitrary real phases (the theorem as formulated in the Letter is recovered by setting $\chi_k = 0$), and by choosing the Hamiltonian control $H_c(t)$ such that

$$U_\alpha(t)\,|\mu_k(0)\rangle = |\mu_k(t)\rangle \quad \forall k = 1,\ldots,d \quad \forall t, \tag{55}$$

where

$$U_\alpha(t) = \mathcal{T}\left[\exp\left(-\mathrm{i}\int_0^t [H_\alpha(\tau) + H_c(\tau)]\,\mathrm{d}\tau\right)\right]. \tag{56}$$

Proof. From theorem I.1 we have that for any state ρ and any generator h_α with ordered eigenvalues $p_1 \geq \cdots \geq p_d$ and $h_1 \geq \cdots \geq h_d$, respectively, the maximal QFI with respect to all unitary state preparations $U\rho U^\dagger$, $U \in \mathrm{U}(d)$, is given by

$$I_\alpha^* \coloneqq \max_U I_\alpha(U\rho U^\dagger) = \frac{1}{2}\sum_{j=1}^d p_{j,d-j+1}(h_j - h_{d-j+1})^2. \tag{57}$$

Further, the generator can be written as [5, Eq. 6]

$$h_\alpha = \int_0^T U_\alpha^\dagger(t)\partial_\alpha H_\alpha(t)U_\alpha(t)\,\mathrm{d}t, \tag{58}$$

Writing the integral as an infinite sum,

$$h_\alpha = \lim_{n\to\infty}\sum_{l=0}^n U_\alpha^\dagger(lT/n)\partial_\alpha H_\alpha(lT/n)U_\alpha(lT/n)T/n, \tag{59}$$

repeated application of lemma II.4 to bipartitions of the sum yields in the limit of infinite many applications of lemma II.4

$$I_\alpha^* = \frac{1}{2}\sum_{j=1}^d p_{j,d-j+1}(h_j - h_{d-j+1})^2 \leq \frac{1}{2}\sum_{j=1}^d p_{j,d-j+1}\left(\int_0^T [\mu_j(t) - \mu_{d-j+1}(t)]\,\mathrm{d}t\right)^2 = K_\alpha. \tag{60}$$

It remains to show that Eq. (52) can be saturated. In order to show this it suffices to calculate the QFI for the initial state as defined in Eqs. (53) and (54) and a generator as given in Eq. (59) with the unitary transformation fulfilling Eq. (56):

$$I_\alpha(\rho^*) = 2\sum_{i,j=1}^d p_{i,j}\,|\langle\phi_i|\,h_\alpha\,|\phi_j\rangle|^2 \tag{61}$$

where $|\phi_j\rangle$ are defined in Eq. (54). More explicitly, in

$$\langle\phi_i|\,h_\alpha\,|\phi_j\rangle = \lim_{n\to\infty}\sum_{l=0}^n \langle\phi_i|\,U_\alpha^\dagger(lT/n)\partial_\alpha H_\alpha(lT/n)U_\alpha(lT/n)\,|\phi_j\rangle\,T/n \tag{62}$$

13

we use the definition of $|\phi_j\rangle$ and Eq. (55) which gives, due to

$$\langle\mu_i(lT/n)|\partial_\alpha H_\alpha(lT/n)|\mu_j(lT/n)\rangle = \delta_{i,j}\mu_i(lT/n), \qquad (63)$$

the following expression for the matrix coefficients in Eq. (62):

$$\langle\phi_i|U_\alpha^\dagger(lT/n)\partial_\alpha H_\alpha(lT/n)U_\alpha(lT/n)|\phi_j\rangle$$
$$= \delta_{i,j}\frac{\mu_i(lT/n)+\mu_{d-i+1}(lT/n)}{2} + \delta_{i,d-j+1}\frac{|\mu_i(lT/n)-\mu_{d-i+1}(lT/n)|}{2}. \quad (64)$$

Due to $p_{i,i} = 0$ one obtains

$$I_\alpha(\rho^*) = 2\sum_{j=1}^{d}p_{j,d-j+1}\left|\lim_{n\to\infty}\sum_{l=0}^{n}\frac{\mu_j(lT/n)-\mu_{d-j+1}(lT/n)}{2}T/n\right|^2 \qquad (65)$$

$$= \frac{1}{2}\sum_{j=1}^{d}p_{j,d-j+1}\left(\int_0^T[\mu_j(t)-\mu_{d-j+1}(t)]\,\mathrm{d}t\right)^2 = K_\alpha. \qquad (66)$$

$\square$

III. PROOF OF HEISENBERG SCALING FOR THERMAL STATES

In this section we will prove that if a product of N thermal spin-j states (at arbitrary finite temperature) is available and sensor dynamics is unitary, one can reach Heisenberg scaling of the QFI I_α for unitary dynamics in N and j by preparing the optimal initial state according theorem 1 in the Letter (or theorem 2, in case of Hamiltonian control). Heisenberg scaling in N and j means $I_\alpha \propto N^2$ for any $j = \frac{1}{2}, 1, \frac{3}{2}, \dots$ and $I_\alpha \propto j^2$ for any $N = 1, 2, 3, \dots$.

According to the pinching theorem (also known as squeeze theorem) a function scales with N^2 (j^2) if there are upper and lower bounds scaling as N^2 (j^2). Clearly, the QFI of a product of N thermal spin-j states is upper bounded by the pure-state case obtained in the limiting case of zero temperature. For pure states, it is well known that the QFI, optimized over unitary state preparations, scales as N^2 (j^2). We will find lower bounds for the QFI of a product of N thermal spin-j states that scale as N^2 (j^2).

Let the QFI be given by (compared to Eq. (14) in the Letter, we set $g(T) = 1$ because we are only interested in the scaling with N and j in the following)

$$K_B = \frac{4}{Z_\beta^N}\sum_{k=-Nj}^{Nj}q(k)\frac{\sinh^2(\beta k)}{\cosh(\beta k)}k^2, \qquad (67)$$

14

with $q(k)$ the number of possibilities of getting a sum k when rolling N fair dice, each having $2j+1$ sides corresponding to values $\{-j,\ldots,j\}$, and with Z_β the partition function

$$Z_\beta = \sum_{m=-j}^{j} e^{\beta m} = \cosh(\beta j) + \frac{\sinh(\beta j)}{\tanh(\beta/2)}, \tag{68}$$

which was rewritten (for $\beta > 0$) making use of the geometric series. First, we find a lower bound L_B for K_B:

$$K_B = \frac{4}{Z_\beta^N} \sum_{k=-Nj}^{Nj} q(k) \frac{\sinh^2(\beta k)}{\cosh(\beta k)} k^2 = \frac{4}{Z_\beta^N} \sum_{k=-Nj}^{Nj} q(k) \left(\cosh(\beta k) - \frac{1}{\cosh(\beta k)}\right) k^2 \tag{69}$$

$$\geq \frac{4}{Z_\beta^N} \sum_{k=-Nj}^{Nj} q(k) \left(\cosh(\beta k) - 1\right) k^2 =: L_B, \tag{70}$$

where we used that each summand is nonnegative and

$$\frac{\sinh^2(\beta k)}{\cosh(\beta k)} = \frac{\cosh^2(\beta k) - 1}{\cosh(\beta k)} = \cosh(\beta k) - \frac{1}{\cosh(\beta k)} \geq \cosh(\beta k) - 1, \tag{71}$$

which follows from the trigonometric identity $\sinh^2(x) - \cosh^2(x) = 1$ and $\cosh(x) \geq 1$. Next, we rewrite L_B as

$$L_B = \frac{4}{Z_\beta^N} \sum_{k=-Nj}^{Nj} q(k) \left(e^{\beta k} - 1\right) k^2, \tag{72}$$

where we used that $\cosh(x) = (e^x + e^{-x})/2$ and $\sum_{k=-Nj}^{Nj} q(k) e^{\beta k} k^2 = \sum_{k=-Nj}^{Nj} q(k) e^{-\beta k} k^2$ because $q(k)k^2$ is symmetric around $k = 0$.

Then, we make use of the generating function of $q(k)$ [6]:

$$\left(x^{-j} + x^{-j+1} + \cdots + x^j\right)^N = \sum_{k=-Nj}^{Nj} q(k) x^k. \tag{73}$$

By setting $x = e^\beta$, we find $Z_\beta^N = \sum_{k=-Nj}^{Nj} q(k) e^{\beta k}$. Taking the second derivative with respect to β yields

$$\frac{\partial Z_\beta^N}{\partial \beta^2} = \sum_{k=-Nj}^{Nj} q(k) e^{\beta k} k^2. \tag{74}$$

With this, we rewrite L_B as

$$L_B = \left(\frac{\partial^2 Z_\beta^N}{\partial \beta^2} - \left.\frac{\partial^2 Z_\beta^N}{\partial \beta^2}\right|_{\beta=0}\right) \frac{4}{Z_\beta^N}, \tag{75}$$

where the second term is evaluated for $\beta = 0$ and corresponds the negative part of L_B in Eq. (72). Since $Z_\beta \geq Z_{\beta=0}$, we find the lower bound

$$-\left.\frac{\partial^2 Z_\beta^N}{\partial\beta^2}\right|_{\beta=0} \frac{4}{Z_\beta^N} \geq -\left.\frac{\partial^2 Z_\beta^N}{\partial\beta^2}\right|_{\beta=0} \frac{4}{Z_0^N}, \tag{76}$$

which is readily evaluated:

$$-\left.\frac{\partial^2 Z_\beta^N}{\partial\beta^2}\right|_{\beta=0} \frac{4}{Z_0^N} = -4\left[N(N-1)\left(\frac{\partial Z_\beta/\partial\beta|_{\beta=0}}{Z_0}\right)^2 + N\frac{\partial^2 Z_\beta/\partial\beta^2|_{\beta=0}}{Z_0}\right], \tag{77}$$

and with $\partial Z_\beta/\partial\beta|_{\beta=0} = \sum_{m=-j}^{j} m = 0$ we find

$$-\left.\frac{\partial^2 Z_\beta^N}{\partial\beta^2}\right|_{\beta=0} \frac{4}{Z_0^N} = -4N\sum_{m=-j}^{j} m^2/(2j+1) = -\frac{4}{3}Nj(j+1), \tag{78}$$

again using the geometric series. Together with

$$\frac{\partial^2 Z_\beta^N}{\partial\beta^2}\frac{4}{Z_\beta^N} = 4N(N-1)\left(\frac{\partial Z_\beta/\partial\beta}{Z_\beta}\right)^2 + 4N\frac{\partial^2 Z_\beta/\partial\beta^2}{Z_\beta}, \tag{79}$$

this brings us to another lower bound:

$$L_B \geq M_B := 4\left[N(N-1)\left(\frac{\partial Z_\beta/\partial\beta}{Z_\beta}\right)^2 + N\frac{\partial^2 Z_\beta/\partial\beta^2}{Z_\beta} - \frac{1}{3}Nj(j+1)\right] \tag{80}$$

Neglecting terms proportional to N we find after trivial algebraic transformations

$$M_B \propto 4N^2\left(\frac{\partial Z_\beta/\partial\beta}{Z_\beta}\right)^2 \tag{81}$$

$$= N^2\frac{\{(1+j)\sinh(\beta j) - j\sinh[\beta(1+j)]\}^2}{\sinh^2\left(\frac{\beta}{2}\right)\sinh^2\left[\beta(j+\frac{1}{2})\right]}, \tag{82}$$

which is clearly nonnegative for finite temperatures ($\beta > 0$). In order to become zero,

$$\frac{\sinh[\beta j]}{\beta j} = \frac{\sinh[\beta(j+1)]}{\beta(j+1)} \tag{83}$$

would have to be fulfilled. However, since $\frac{\sinh(x)}{x} = 1 + \frac{x^2}{3!} + \frac{x^4}{5!} + \cdots$ is an increasing function on $x \in [0,\infty)$, Eq. (83) leads to a contradiction for $\beta > 0$. Therefore, the expression in Eq. (82) is positive for finite temperatures which proves the N^2 scaling for all $j = \frac{1}{2}, 1, \frac{3}{2}, \ldots$.

There are two remarks in order:

(i) In summary the lower bound M_B was obtained from QFI K_B by finding a lower bound for the negative term of the QFI in Eq. (69),

$$-\frac{4}{Z_\beta^N} \sum_{k=-Nj}^{Nj} q(k) \frac{k^2}{\cosh(\beta k)} \ge -\frac{4}{3} Nj(j+1). \tag{84}$$

Since the right-hand side scales linearly in N, the left-hand side scales at most linearly in N and, in particular, cannot scale quadratically. Thus, the N^2-scaling of the QFI solely comes from the positive term in Eq. (69). Therefore, in leading order of N we find for the QFI exactly Eq. (81), i.e.,

$$K_B = 4N^2 \left(\frac{\partial Z_\beta / \partial \beta}{Z_\beta}\right)^2 + \mathcal{O}(N) = 4N^2 \left(\frac{\partial \ln Z_\beta}{\partial \beta}\right)^2 + \mathcal{O}(N), \tag{85}$$

where $\mathcal{O}(N)$ denotes terms $\propto N$ and lower-order terms. With the operator S_z of a spin j in z-direction and corresponding thermal state $\rho_{\text{th}} = e^{\beta S_z}/Z_\beta$, we rewrite $Z_\beta = \text{tr}\left[e^{\beta S_z}\right]$ and

$$4N^2 \left(\frac{\partial \ln Z_\beta}{\partial \beta}\right)^2 = 4N^2 \langle S_z \rangle^2, \tag{86}$$

where $\langle S_z \rangle = \text{tr}\left[\rho_{\text{th}} S_z\right]$.

(ii) Let us identify $\beta = 1/\chi$ with a temperature χ. A Taylor expansion of the prefactor $Q(\beta) := 4\left(\frac{\partial \ln Z_\beta}{\partial \beta}\right)^2$ in Eq. (86) around $\beta = 0$ yields

$$Q(\beta) = \frac{4}{9} [j(j+1)]^2 \beta^2 + \mathcal{O}(\beta^4), \tag{87}$$

where $\mathcal{O}(\beta^4)$ denotes terms $\propto \beta^4$ and higher-order terms which can be neglected for small β. This shows that for small β, i.e., for large temperatures χ, the prefactor decays quadratically, $\propto \chi^{-2}$. Also, in this regime of high temperatures, the QFI scales with j^4. However, if the product $j\beta$ is of order one (or larger), we are no longer in the range of validity of the second-order Taylor expansion in Eq. (87). As we will see in the next section, the QFI scales $\propto j^2$ in the limit of large j.

In order to prove j^2 scaling, we first consider

$$M_B(N) - NM_B(N=1) = N(N-1)\left(\frac{\partial Z_\beta / \partial \beta}{Z_\beta}\right)^2 \ge 0 \tag{88}$$

17

for any $N \geq 1$. It follows that $M_B(N) \geq N M_B(N = 1)$. We find after some simple algebraic transformations using the partition function as given in Eq. (68),

$$NM_B(1) = 4N\left[\frac{\partial^2 Z_\beta/\partial\beta^2}{Z_\beta} - \frac{j(j+1)}{3}\right] \tag{89}$$

$$= N\left[j^2\frac{8}{3} - j\frac{10\cosh(\beta j) + 2\cosh[\beta(j+1)]}{3\sinh(\beta/2)\sinh[\beta(j+1/2)]} + \frac{\sinh(\beta)\sinh(\beta j)}{\sinh^3(\beta/2)\sinh[\beta(j+1/2)]}\right], \tag{90}$$

which is well defined for finite temperatures, and the third summand as well as the prefactor of j in the second summand clearly converge to a constant in the limit of large j. This proves the j^2 scaling for finite temperatures for any $N = 1, 2, \ldots$.

---

[1] P. Bloomfield and G. S. Watson, The inefficiency of least squares, Biometrika **62**, 121 (1975).

[2] S. Drury, S. Liu, C.-Y. Lu, S. Puntanen, and G. P. Styan, Some Comments on Several Matrix Inequalities with Applications to Canonical Correlations: Historical Background and Recent Developments, Sankhyā: The Indian Journal of Statistics, Series A , 453 (2002).

[3] W. Fulton, Eigenvalues, invariant factors, highest weights, and Schubert calculus, Bulletin of the American Mathematical Society **37**, 209 (2000).

[4] A. W. Marshall, I. Olkin, and B. C. Arnold, *Inequalities: Theory of Majorization and Its Applications*, Vol. 143 (Springer, 1979).

[5] S. Pang and A. N. Jordan, Optimal adaptive control for quantum metrology with time-dependent Hamiltonians, Nature Communications **8**, 14695 (2017).

[6] J. V. Uspensky, *Introduction to Mathematical Probability* (McGraw-Hill Book Company, New York, 1937).

Improving the dynamics of quantum sensors with reinforcement learning

Jonas Schuff, Lukas J. Fiderer, and Daniel Braun

Institute for Theoretical Physics, University of Tübingen,

Auf der Morgenstelle 14, 72076 Tübingen, Germany

(Dated: September 13, 2019)

Abstract

Recently proposed *quantum-chaotic sensors* achieve quantum enhancements in measurement precision by applying nonlinear control pulses to the dynamics of the quantum sensor while using classical initial states that are easy to prepare. Here, we use the cross entropy method of reinforcement learning to optimize the strength and position of control pulses. Compared to the quantum-chaotic sensors in the presence of superradiant damping, we find that decoherence can be fought even better and measurement precision can be enhanced further by optimizing the control. In some examples, we find enhancements in sensitivity by more than an order of magnitude. By visualizing the evolution of the quantum state, the mechanism exploited by the reinforcement learning method is identified as a kind of spin-squeezing strategy that is adapted to the superradiant damping.

CONTENTS

2

I. INTRODUCTION

The rise of machine learning [1] has led to intense interest in using machine learning in physics, and in particular in combining it with quantum information technology [2, 3]. Recent success stories include discriminating phases of matter [4–6] and efficient representation of many-body quantum states [7–9].

In physics, many problems can be described within control theory which is concerned with finding a way to steer a system to achieve a goal [10]. The search for optimal control can naturally be formulated as reinforcement learning (RL) [11–19], a discipline of machine learning. Reinforcement learning (RL) has been used in the context of quantum control [17], to design experiments in quantum optics [20], and to automatically generate sequences of gates and measurements for quantum error correction [16, 21, 22].

RL has also been applied to control problems in quantum metrology [2]: In the context of global parameter estimation, i.e., when the parameter is a priori unknown, the problem of optimizing single-photon adaptive phase-estimation was investigated [23–25]. There, the goal is to estimate an unknown phase difference between the two arms of a Mach–Zehnder interferometer. After each measurement, an additional controllable phase in the interferometer can be adjusted dependent on the already acquired measurement outcomes. The optimization with respect to policies, i.e., mappings from measurement outcomes to controlled phase shifts, can be formulated as a RL problem and tackled with particle swarm [23, 24, 26, 27] or differential evolution [25, 28] algorithms, where the results of the former were recently applied in an experiment [29].

Also in the regime of local parameter estimation, where the parameter is already known to high precision (typically from previous measurements), actor-critic and proximal-policy-optimization RL algorithms were used to find policies to control the dynamics of quantum sensors [30–32]. There, the estimation of the precession frequency of a dissipative spin-$\frac{1}{2}$ particle was improved by adding a linear control to the dynamics in form of an additional controlled magnetic field [32].

Recently it was shown theoretically that the sensitivity (in the regime of local parameter estimation) of existing quantum sensors based on precession dynamics, such as spin-precession magnetometers, can be increased by adding nonlinear control to their dynamics in such a way that the dynamics becomes non-regular or (quantum-)chaotic [33, 34]. The

3

nonlinear kicks (described by a "nonlinear" Hamiltonian $\propto J_y^2$ compared to the "linear" precession Hamiltonian $\propto J_z$ where J_x, J_y, J_z are the spin angular momentum operators) lead to a torsion, a precession with rotation angle depending on the state of the spins.

Adding nonlinear kicks to the otherwise regular dynamics comes along with a large number of new degrees of freedom that remained so far unexplored: Rather than kicking the system periodically with always the same strength and with the same preferred axis as in Ref. [33], one can try to optimize each kick individually, i.e., vary its timing, strength, or rotation axis. The number of parameters increases linearly with the total measurement time (assuming a fixed upper bound of kicks per unit time), and becomes rapidly too large for brute-force optimization.

In this work, we use cross-entropy RL to optimize the kicking strengths and times in order to maximize the quantum Fisher information, whose inverse constitutes a lower bound on the measurement precision. The cross-entropy method is used to train a neural network that takes the current state as input and gives an action on the current state (the nonlinear kicks) as output. In this way, the neural network generates a sequence of kicks that represents the policy for steering the dynamics.

This represents an offline, model-free approach which is aimed at long-term performance, i.e., the optimization is done based on numerical simulations, without being restricted to a specific class of policies, and with the goal of maximizing the quantum Fisher information only after a given time and not, as it would be the case for greedy algorithms, for each time step. We show that this can lead to largely enhanced sensitivity even compared to the already enhanced sensitivity of the quantum-chaotic sensor with constant periodic kicks [33].

II.   QUANTUM METROLOGY

The standard tool for evaluating the sensitivity with which a parameter can be measured is the quantum Cramér-Rao bound [35–37]. It gives the smallest uncertainty with which a parameter ω encoded in a quantum state (density matrix) ρ_ω can be estimated. The bound is optimized over all possible (POVM=positive operator valued measure) measurements (including but not limited to standard projective von-Neumann measurements of quantum observables), and all possible data-analysis schemes in the sense of using arbitrary unbiased

estimator functions $\hat{\omega}$ of the obtained measurement results. It can be saturated in the limit of a large number M of measurements, and hence gives the ultimate sensitivity that can be reached once technical noise has been eliminated and only the intrinsic fluctuations due to the quantum state itself remain.
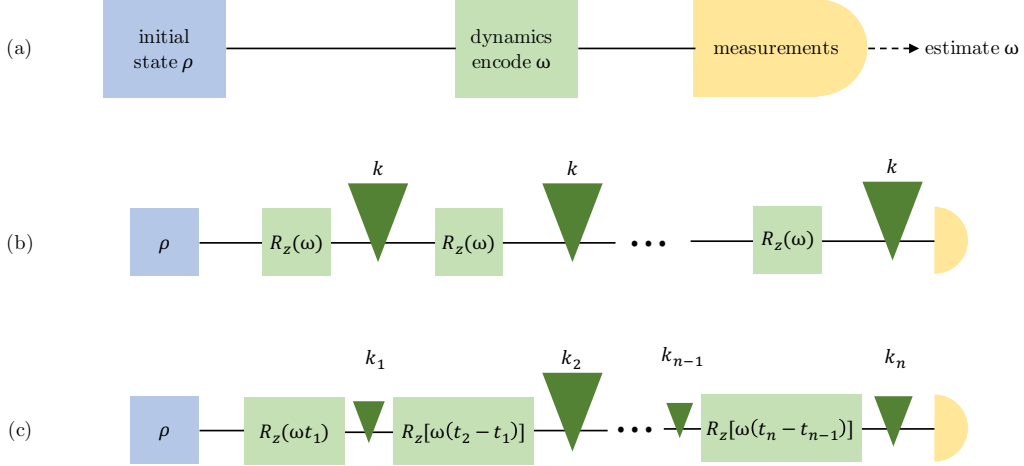

FIG. 1. Schematic representation of parameter encoding in quantum metrology. Panel (a) shows the standard protocol: the parameter ω is encoded in the initial state ρ through the dynamics, the resulting state is measured, and the parameter is inferred by (classical) post processing of the measurement outcomes. In panel (b), the dynamics is given by the kicked top model: the encoding of the parameter ω through linear precession $R_z(\omega)$ about the z-axis is periodically disrupted through parameter-independent, nonlinear, controlled kicks (green triangles) with kicking strength k that can render the dynamics chaotic. In panel (c), the dynamics is given by a generalized kicked top model: the kicking strengths k_ℓ and times t_ℓ between kicks are optimized in order to maximize the sensitivity with which ω can be inferred (varying k_ℓ are indicated by different sizes of the green triangles). Variation of the kicking axis is possible but beyond the scope of this work.

The quantum Cramér-Rao bound for the smallest possible variance of the estimate $\hat{\omega}$ reads

$$\mathrm{Var}(\hat{\omega}) \geq \frac{1}{M I_\omega}. \tag{1}$$

For a state given in diagonalized form, $\rho_\omega := \sum_{\ell=1}^{d} p_\ell \, |\psi_\ell\rangle \langle\psi_\ell|$, where d is the dimension of the Hilbert space, the quantum Fisher information (QFI) is given by [38]

$$I_\omega = 2 \sum_{\ell,m=1}^{d} \frac{\left|\langle\psi_\ell| \, \partial_\omega \rho_\omega \, |\psi_m\rangle\right|^2}{(p_\ell + p_m)^2}, \tag{2}$$

5

where the sum runs over all ℓ, m such that $p_\ell + p_m \neq 0$, and $\partial_\omega \rho_\omega \coloneqq \frac{\partial \rho_\omega}{\partial \omega}$.

III. THE SYSTEM

We consider a spin model based on the angular momentum algebra, with spin operators $\mathbf{J} = (J_x, J_y, J_z)$, $J_z |jm\rangle = \hbar j |jm\rangle$ and $\mathbf{J}^2 |j, m\rangle = \hbar^2 j(j+1) |j, m\rangle$, where j and m are angular momentum quantum numbers. Note that the model can be implemented not only with physical spins but with any physical system with quantum mechanical operators that fulfill the angular momentum algebra. The Hamiltonian of our model is given by

$$\mathcal{H}_{\text{KT}}(t) = \omega J_z + \frac{J_y^2}{(2j+1)\hbar} \sum_{\ell=-\infty}^{\infty} \kappa_\ell \tau \delta(t - t_\ell). \tag{3}$$

The first summand describes a precession about the z-axis with precession frequency ω. The second summand describes the nonlinear kicks, i.e., a torsion about the y-axis, see Fig. 1. This corresponds to a precession about the y-axis with a precession angle proportional to the y-component. The time τ defines a time scale such that t and t_ℓ measure time in units of τ. The ℓth kick is applied at time t_ℓ where κ_ℓ quantifies its kicking strength (in units of a frequency).

In an atomic spin-precession magnetometer, as discussed in Ref. [33], the first summand corresponds to a Larmor precession characterized by the Larmor frequency $\omega = g\mu_{\text{B}}B/\hbar$ with Landé g-factor g, Bohr magneton μ_{B}, and magnetic field strength B, which is the parameter that one wants to estimate. The nonlinear kicks can, for example, be generated with off-resonant light pulses exploiting the ac Stark effect. We introduce a dimensionless kicking strength as $k_l \coloneqq \kappa_\ell \tau$ and, for the sake of simplicity, we set $\tau = 1$ and $\hbar = 1$.

For a pure state, the unitary time evolution of the system between kicks at time $t_{\ell-1}$ and t_ℓ is given by

$$|\psi_\omega(t_\ell)\rangle = U_\omega(k_\ell) |\psi(t_{\ell-1})\rangle, \tag{4}$$

where the unitary transformation $U_\omega(k_\ell)$ propagates the state according to the Hamiltonian (3), from time $t_{\ell-1}$ [directly after the $(\ell-1)$th kick] to t_ℓ [directly after the ℓth kick], as indicated by the index ℓ [in order to simplify notation, the index ℓ of k not only labels the kicking strength at time t_ℓ but also refers to the propagation from $t_{\ell-1}$ to t_ℓ of $U_\omega(k_\ell)$]. We have

$$U_\omega(k_\ell) = \mathcal{T} \exp\left[-\mathrm{i} \int_{t_{\ell-1}}^{t_\ell} dt' \mathcal{H}_{\text{KT}}(t')\right], \tag{5}$$

6

where $\mathcal{T}$ denotes time-ordering. Since the kicks are assumed to be instantaneous, this leads to

$$U_\omega(k_\ell) = \exp\left[-\mathrm{i}\, k_\ell \frac{J_y^2}{(2j+1)}\right] \exp\left[-\mathrm{i}\,\omega(t_\ell - t_{\ell-1})J_z\right], \qquad (6)$$

i.e., a precession for time $t_\ell - t_{\ell-1}$ followed by a kick of strength k_ℓ. The kick occurs at the end of the time interval $[t_{\ell-1}, t_\ell]$.

For the standard kicked top (KT), , see Fig. 1, the kicking strengths are constant, $k_\ell = k$, and kicking times are given by $t_\ell = \ell\tau = \ell$, with $\ell \in \mathbb{N}$. Dynamics of the standard KT is non-integrable for $k > 0$ and has a well defined classical limit that shows a transition from regular to chaotic dynamics when k is increased. In Ref. [33] the behavior of the QFI for regular and chaotic dynamics was studied in this transition regime (for $k = 3$ and $\omega = \pi/2$) which manifests itself by a mixed classical phase space between regular and chaotic dynamics. Quantum chaos is defined as quantum dynamics that becomes chaotic in the classical limit. In contrast to classical chaos, quantum chaos does not exhibit exponential sensitivity to changes of initial conditions due to the properties of unitary quantum evolution, but can be very sensitive to parameters of the evolution [39]. The kicked top has been realized with atomic spins in a cold gas [40] and with a pair of spin-1/2 nuclei using NMR techniques [41]. Here, we generalize the standard KT to kicks of strength k_ℓ at arbitrary times t_ℓ as given in Eq. (6), see also Fig. 1.

Any new quantum metrology method needs to demonstrate its viability in the presence of noise and decoherence. We study two different versions of the KT which differ in the decoherence model used: phase damping and superradiant damping. Both can be described by Markovian master equations and are well studied models for open quantum systems [42–45]. While phase damping conserves the energy and only leads to decoherence in the $|j, m\rangle$ basis, superradiant damping leads in addition to a relaxation to the ground state $|j, -j\rangle$. Its combination with periodic kicking in the chaotic regimes is known to give rise to a non-equilibrium steady state in the form of a smeared-out strange attractor [45] that still conserves information about the parameter ω, whereas without the kicking the system in presence of superradiant damping simply decays to the ground state. The master equations for both processes have the Kossakowski–Lindblad form [46, 47], with

$$\dot{\rho}(t) = \gamma_{\mathrm{pd}}\left([J_z, \rho(t)J_z] + \mathrm{h.c.}\right) \qquad (7)$$

for phase damping, where $\dot{\rho}(t) = \frac{\mathrm{d}}{\mathrm{d}t}\rho(t)$, and

$$\dot{\rho}(t) = \gamma_{\mathrm{sr}}\left(\left[J_-, \rho(t)J_+\right] + \mathrm{h.c.}\right) \tag{8}$$

for superradiant damping, where $J_\pm := J_x \pm iJ_y$ are the ladder operators, and γ_{pd} and γ_{sr} denote the decoherence rates. With the generator Λ, defined by $\dot{\rho}(t) = \Lambda\rho(t)$, one has in both cases the formal solution $\rho(t_n) = D\left(t_n - t_{n-1}\right)\rho(t_{n-1})$ with the continuous-time propagator $D\left(t\right) := e^{\Lambda t}$. The solution of Eq. (7) in the $|j, m\rangle$ basis, where $\rho(t) = \sum_{m,m'=-j}^{j}\rho_{m,m'}(t)|j, m\rangle\langle j, m'|$, is immediate,

$$\rho_{m,m'}(t) = \rho_{m,m'}(0)\exp\left[-\gamma_{\mathrm{pd}}t(m - m')^2\right]. \tag{9}$$

Also for Eq. (8) a formally exact solution has been found [48] and efficient semiclassical (for large j) expressions are available [49, 50]. For our purposes it was the simplest to solve Eq. (8) numerically by diagonalization of Λ. Combining these decoherence mechanisms with the unitary evolution the transformation $\rho(t_{\ell-1}) \rightarrow \rho(t_\ell)$ reads

$$\rho(t_\ell) = U_\omega(k_\ell)\left[D\left(t_\ell - t_{\ell-1}\right)\rho(t_{\ell-1})\right]U_\omega(k_\ell)^\dagger, \tag{10}$$

because in both cases the dissipative generator Λ commutes with the precession.

As initial state we use an SU(2) coherent state, which can be seen as the most classical state of a spin [51, 52], and is usually easy to prepare (for instance by optically polarizing the atomic spins in a SERF magnetometer). Also, it is equivalent to a symmetric state of $2j$ spin-$\frac{1}{2}$ pointing all in the same direction. With respect to the $|j, m\rangle$ basis it reads

$$|j, \theta, \phi\rangle = \sum_{m=-j}^{j}\sqrt{\binom{2j}{j-m}}\sin\left(\frac{\theta}{2}\right)^{j-m}\cos\left(\frac{\theta}{2}\right)^{j+m}e^{i(j-m)\phi}|j, m\rangle. \tag{11}$$

We choose $\theta = \frac{\pi}{2}$, $\phi = \frac{\pi}{2}$.

IV. THE KICKED TOP AS A CONTROL PROBLEM AND REINFORCEMENT LEARNING

We consider the kicked top as a control problem and discretize the kicking strengths k_ℓ and times t_ℓ. The precise parameters of the discretized control problem vary between the following examples and are summarized in Appendix A. In the following, t_{step} denotes a

discrete time step (measured in units of $\tau = 1$), k_{step} is a discrete step of kicking strength, the RL agent optimizes the QFI at time T_{opt}, and we bound the total accumulated kicking strength $\sum_{\ell} k_{\ell} < 15000$ which is never reached in optimized policies though. The frequency ω, that we want to estimate, is set to induce a rotation of the state by $t\pi/2$ (t is measured in units of $\tau = 1$).

Possible control policies are simply given by a vector of kicking strengths $\boldsymbol{k} = (k_1, \ldots, k_N) \in \mathbb{R}^N$ with $k_{\ell} \in \{qk_{\text{step}} : q = 0, 1, 2, \ldots\}$. To each policy corresponds a QFI value, calculated from the resulting state $\rho(T_{\text{opt}})$, which quantifies how well the policy performs. To tackle this type of problem, various numerical algorithms are available, each with its own advantages and drawbacks [2, 3, 15]. We pursue the relatively unexplored (in the context of physics) route of cross-entropy RL.

The system, the kicked top, will be called "environment", and we imagine an "RL agent" interacting with the environment by applying nonlinear kicks ("actions") and getting in response information about the current state of the environment ("observation", which is in our case the full density matrix of the current state), see Fig. 2. The RL agent repeatedly has to take the decision whether to increase the kicking strength (by k_{step}) or to go on from the current position in time ℓt_{step} to $(\ell+1)t_{\text{step}}$. After each decision, it obtains an observation and, only after the total time T_{opt}, a "reward" (the quantum Fisher information of $\rho(T_{\text{opt}})$), that it seeks to maximize. This concludes one "episode" after which the environment is reset [i.e., the spin is reinitialized in the coherent state at $\theta = \frac{\pi}{2}$, $\phi = \frac{\pi}{2}$, see Eq. (11)] and the next episode starts.

In our case, a neural network represents the RL agent: The observation is given to the neural network's input neurons while each output neuron represents one possible action, i.e., we have two output neurons for "kick" and "go on". The activation of these output neurons determines the probability of executing that action. The policy, however, is not given by the neural network directly. Since the environment is deterministic (i.e., the state evolves deterministically for a given policy $\boldsymbol{k}$ of kicking strengths) there is no point in choosing a stochastic policy such as a neural network. Instead, a single choice of kicking strengths $\boldsymbol{k}$ represents the policy which is obtained by first generating a few episodes with several trained neural networks and then picking the episode with the largest QFI. The kicking strengths applied in that episode represent the policy (see Appendix B)[1].

---

[1] In comparison, Sanders et al. [23–25] restricted their policy search for adaptive single-photon interferom-
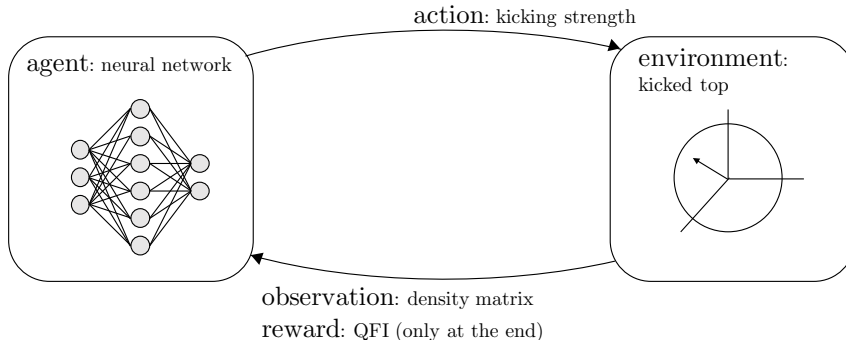
FIG. 2. Typical setup in reinforcement learning: the RL agent acts upon the environment which in return gives the RL agent an observation and a reward. In our case the RL agent is a neural network and the environment is the generalized kicked top.

The RL cross-entropy method [53] we use works as follows: We produce a set of episodes with the neural network, and then we reinforce the actions of the episodes with the highest reward. This is done by choosing the best 10% of episodes and we use the pairs of observations and actions of these episodes to train the neural network with the stochastic gradient descent method called *Adam* (see Appendix for details) [54]. As a result of this training the weights of the neural network are adjusted, i.e., the agent learns from its experience. Future actions taken by the agent are then influenced not only by randomness but also by this experience. The whole process of generating episodes and training the network is iterated. For the parameters of the training process see Appendix B. In Appendix C we study the learning success for different numbers of episodes and iterations.

V. RESULTS

We compare the QFI for different models: (i) the top (simple precession without kicks), (ii) the standard kicked top, as studied in Ref. [33], with periodic kicks (period $\tau = 1$, i.e., a precession angle of $\pi/2$ for one period, and kicking strength $k = 30$), and (iii) the generalized kicked top optimized with RL. In case of superradiance damping (phase damping) we denote the top by SR-T (PD-T), the standard kicked top by SR-KT (PD-KT) and the RL-optimized

etry in such a way that their search space corresponds to points in $\mathbb{R}^N$, making it similar to our problem. However, in their case the observations from the environment are probabilistic measurement outcomes while in our case the observation is the deterministic state ρ.
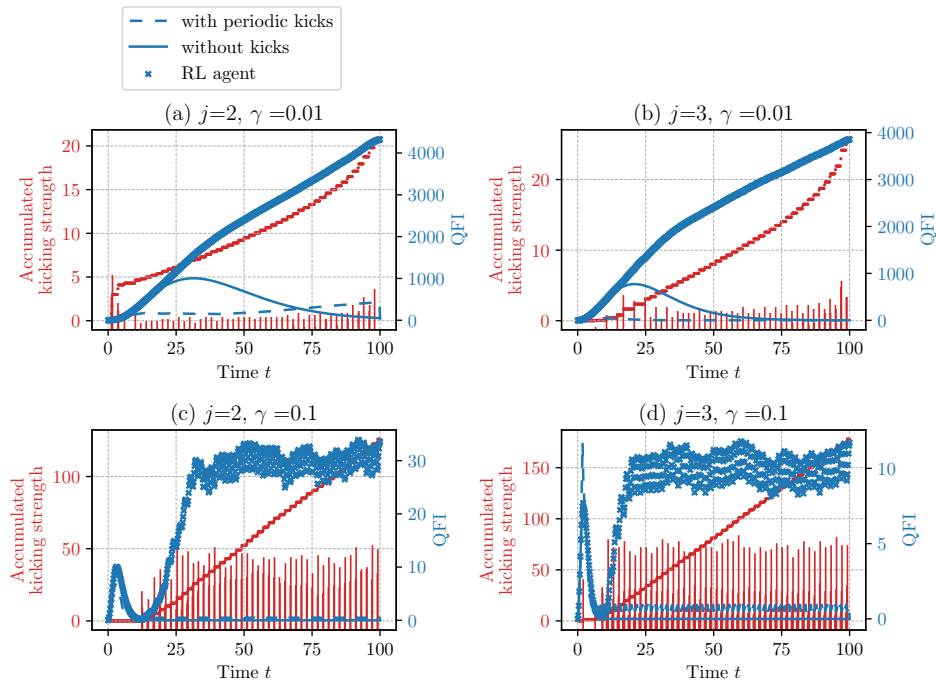
FIG. 3. Examples for the policy adopted by the RL agent for superradiant damping. We plot the accumulated kicking strength on the left axes as red dots and on the right axes in blue the quantum Fisher information for the top (solid line), the periodically kicked top with $k = 30$ chosen as in Ref. [33] (dashed line) and the QFI that corresponds to the policy of the RL agent (crosses). We additionally plot red vertical lines in the places, where the RL agent decides to set a kick. The height of the lines correspond to the kicking strength in arbitrary units and are not on the scale of the left axis. There is a regime where the RL agent manages to increase the QFI with each time step [panel (a) and (b)], and a regime where the RL agent makes the QFI oscillate [panel (c) and (d)].

generalized kicked top by SR-GKT (PD-GKT). Details on the training and the optimization of the RL results are provided in Appendix B.

Let us first consider superradiant damping with results presented in Fig. 3. The QFI for the SR-T exhibits a characteristic growth quadratic in time. However, due to decoherence, the QFI does not maintain this growth but starts to decay rapidly towards zero. The time when the QFI reaches its maximum was found to decay roughly as $1/(\gamma_{\mathrm{sr}}j)$ with spin size j and damping rate γ_{sr} [33].

11

The situation changes with the introduction of nonlinear kicks. There, the QFI for the SR-KT shows the interesting behavior of not decaying to zero for large times. Instead it reaches a plateau value which was found to take surprisingly high values for specific choices of j and dissipation rates [33], in particular, for $j = 2$. The system looses energy through superradiant damping while the nonlinear kicks add energy. This prevents the state from decaying to the ground state, which is an eigenstate of the precession and would lead to a vanishing QFI. From this perspective, the plateau results from a dynamical equilibrium established by the interplay of superradiant damping and kicks.

However, the full potential of exploiting such effects and increasing the QFI with the help of nonlinear kicks is not achieved with constant periodic kicks. Instead, the RL agent[2] finds policies to make the QFI of the SR-GKT increase further even when the QFI of the SR-T decayed already to zero and the QFI of the SR-KT reached its plateau value.

Examples for $j = 2$ and $j = 3$ are presented in Fig. 3. The QFI of the SR-GKT is optimized for a total time T_{opt} which is the largest time plotted in each example. At T_{opt}, the plateau value of the SR-KT for $j = 3$ is relatively low and the RL-optimized policy achieves an improvement in sensitivity (associated with $1/\sqrt{I_\omega}$) of more than an order of magnitude. Panels (a) and (b) show continuous growth of the QFI through an optimized kicking policy. Only if the time T_{opt} (the QFI is optimized to be maximal at T_{opt}) is increased further, the impressive growth of the QFI finally breaks down. Instead of increasing T_{opt}, we choose to increase superradiant damping while keeping T_{opt} constant, which has a similar effect. In that case, see panels (c) and (d), the RL agent chooses a policy which makes the QFI oscillate at a relatively high level before the time T_{opt} is reached.

The superiority of the policies found by the RL agent can be understood by taking a look at the evolution of the quantum state, see Fig. 4: We represent the quantum state in the space of $\boldsymbol{r} = (x, y, z) = (\langle J_x \rangle, \langle J_y \rangle, \langle J_z \rangle)$ where $\langle J_\ell \rangle := \text{tr}(\rho J_\ell)$ and, due to the conservation of angular momentum, $|\boldsymbol{r}| = 1$ which restricts the space to a sphere. This is represented in Fig. 4 with either a sphere parametrized with x, y, and z, or in a plane (the phase space) spanned by the z-coordinate and the azimuthal angle $\phi \in (-\pi, \pi]$ such that $\phi = z = 0$ corresponds to the positive x-axis, $\phi = \pi/2$, $z = 0$ to the positive y-axis, and $z = \pm 1$ with arbitrary ϕ to the positive (negative) z-axis.

The quantum state can be represented in the phase space with the help of the Husimi

---

[2] The training of one RL agent takes about eight hours on a desktop computer.
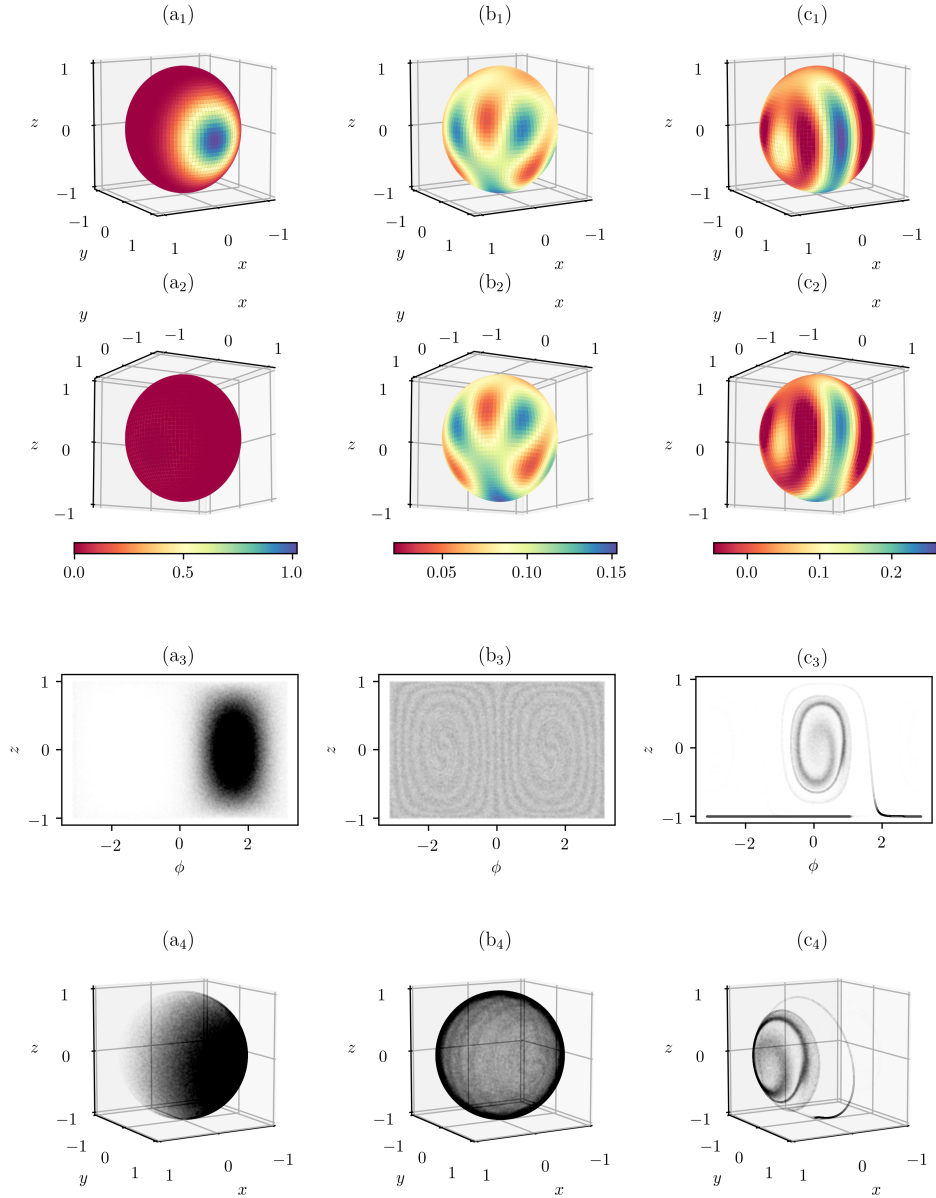
FIG. 4. Illustration of kicked superradiant dynamics with Wigner functions and its classical limit. The spin size is $j = 3$ and the dissipation rate is $\gamma_{sr} = 0.01$. Panels in the left column (a) corresponds to the initial spin coherent state at $\theta = \phi = \pi/2$. The middle and right columns correspond to the state at time T_{opt} generated with periodic kicks (middle column (b), $k = 30$) and with kicks optimized with reinforcement learning [right column (c), the corresponding QFI is shown in panel (b) of Fig. 3]. The top two rows show the Wigner functions of the density matrix, the bottom two rows show the classical phase space, populated by 10^6 points initially distributed according to the Husimi distribution of the initial spin coherent state and then propagated according to the classical equations of motion.

13

or the Wigner distributions which are quasi probability distributions of the quantum state. The first two rows of panels in Fig. 4 depict the Wigner distribution of the initial quantum state (left column) and the quantum states of the SR-KT (middle column, with kicking strength $k = 30$) and SR-GKT (right column) evolved for a time T_{opt} with damping rate $\gamma_{\text{sr}} = 0.01$. The plotted cases for the SR-KT and SR-GKT correspond to the QFI given in panel (b) of Fig. 3, where one can also see the corresponding RL-optimized distribution of kicks.

Due to the small spin size of $j = 3$, we are deep in the quantum mechanical regime which manifests itself in an uncertainty of the initial spin coherent state that is relatively large compared to total size of the phase space. The distribution of the states evolved under dissipative dynamics exhibit remarkable differences for periodic and RL-optimized kicks:

In case of periodic kicks, we find that the initially localized distribution gets distributed over the phase space. It exhibits a maximum on the negative z-axis, see panels (b$_1$) and (b$_2$)in Fig. 4. This is reminiscent of the dissipative evolution in the absence of kicks, where the state is driven towards the ground state $|j, -j\rangle$ which is centered around $z = -1$. The ground state $|j, -j\rangle$ is an eigenstate of the precession and, thus, insensitive to changes in the frequency ω we want to estimate. Similarly, we interpret the part of the state distribution of the SR-KT that is centered around negative z-axis as insensitive. However, the distribution also exhibits non-vanishing parts distributed over the remainder of the phase space that can be understood as being sensitive to changes of ω and therefore explain the non-zero QFI of the SR-KT.

The state corresponding to RL-optimized kicks looks like a strongly squeezed state that almost encircles the whole sphere. Similar to spin squeezing, which is typically applied to the initial state as a part of the state preparation, we interpret the squeezed distribution as particularly sensitive with respect to the precession dynamics. This is due to the reduced uncertainty along the precession trajectories, i.e., with respect to the ϕ coordinate. In the Supplemental Material [3], we provide clips of the evolution over time of the state distributions that illustrate how the RL agent generates the squeezed state. In particular, the squeezed state distribution can be seen as a feature the RL agent is aiming for with its policy. The distribution of RL-optimized kicks is shown in Fig. 3 (in Appendix E, we provide a finer resolution of the distribution of kicks): It is roughly periodic with period corresponding to a

---

[3] The clips are available at https://doi.org/10.6084/m9.figshare.c.4640051.v3.

precession angle of π. Also note that for the SR-GKT the Wigner distribution has negative contributions which is associated with non-classicality of the quantum state [55].

An advantage of the superradiant dynamics lies in its well-defined simple classical limit [45], see also Appendix D. The lower two rows of panels in Fig. 4 depict the corresponding classical limit where the quantum state is represented by a cloud of phase space points (distributed according to the Husimi distribution of the initial spin coherent state) that are propagated according to the classical equations of motion. One of the reasons why the evolved classical distributions differ from the Wigner distributions is the absence of quantum uncertainty in the classical dynamics; in principle, over the course of the dynamics all classical phase space points can be concentrated to an arbitrarily small region of the phase space. In case of the SR-KT, the phase space points are distributed over the whole phase space, reminiscent of classical chaos. However, the distribution is not completely uniform but it exhibits a spiral density inhomogeneity. The plots as in Fig. 4 but for $j = 2$ are shown in the Appendix E.

Fig. 5 shows the gains of the RL-optimized SR-GKT over the SR-T. The gain is defined as the ratio of the RL-optimized QFI at time T_{opt} and the maximum QFI for the SR-T. A broad damping regime is found where gains can be achieved: In the regime of small decoherence rates γ_{sr}, the RL agent can fight decoherence in such a way that the QFI exhibits a continuous growth over the total time T_{opt} [see panels (a) and (b) in Fig. 3]. In comparison with the SR-T, the RL agent benefits of stronger damping in this regime and, therefore, the gain increases with the dissipation rate γ_{sr}. For larger decoherence rates, the RL agent can no longer fight decoherence in the same manner [see panels (c) and (d) in Fig. 3], which manifests itself in a reduction of gains for large decoherence rates. In panel (b) of Fig. 5, we can see the (even larger) gain in QFI compared to the plateau value reached by the SR-KT.

The RL-optimized QFI is associated with a lower bound on the sensitivity (see Eq. 1) for a given measurement time T_{opt}. If measurement time can be chosen arbitrarily, sensitivity is associated with $\max_t I_\omega(t)/t$ [33]. This sensitivity represents the standard quantity reported for experimental parameter estimation because it takes time into account as a valuable resource; sensitivity is given in units of the parameter to be estimated per square root of Hertz. With RL we try to maximize $\max_t I_\omega(t)/t$ with respect to policies.

Fig. 6 compares the SR-T with the SR-GKT where the latter was optimized with RL in
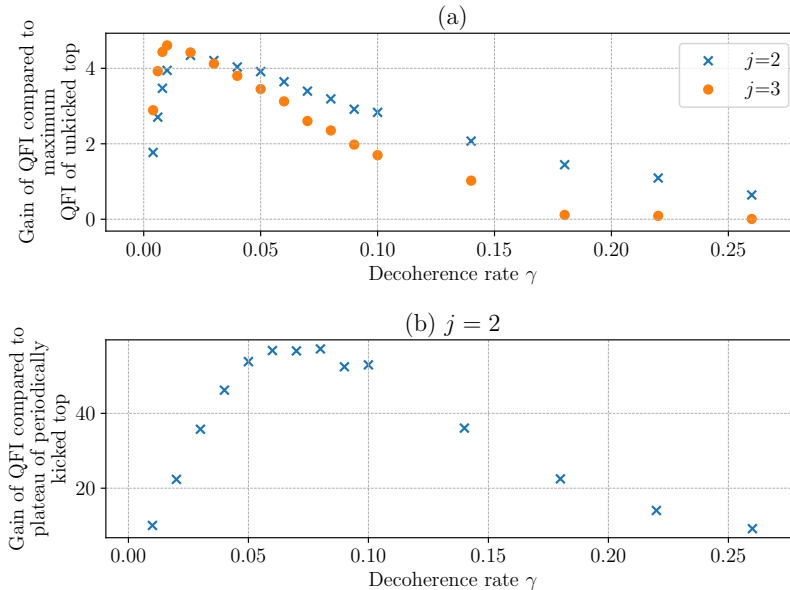
15

FIG. 5. Improvement in the quantum Fisher information due to reinforcement learning for super-radiant damping. The improvement in panel (a) is the ratio of quantum Fisher information at time T_{opt} (100 discretized time steps) optimized with reinforcement learning and the maximum QFI of the top (no kicks). In panel (b) we plot the ratio of the QFI optimized with reinforcement learning and the plateau values achieved by periodic kicking for spin size $j = 2$ and kicking strength $k = 30$. In panel (b), the case of $j = 3$ is omitted due to the very small plateau values in that case. The discretization is coarser than in previous examples: $t_{\text{step}} = 1$ (i.e., a precession angle of $\pi/2$ per time step) and $k_{\text{step}} = 0.1$.

order to maximize the rescaled QFI. Note, that the initial spin coherent state is centered around the positive y-axis, which means it is an eigenstate of the nonlinear kicks; kicks cannot induce spin squeezing at the very beginning of the dynamics. This changes when the spin precesses away from the y axis. Therefore, it makes sense that the RL agent applies the strongest kick only after a precession by about $\pi/2$. The actions that the RL agent takes after the rescaled QFI reached its maximum are irrelevant and can be attributed to random noise generated by the RL algorithm.

As we have seen, the interplay of nonlinear kicks and superradiant damping is very special. However, also for other decoherence models the QFI can be increased significantly, for instance in case of a alkali-vapor magnetometer [33]. To demonstrate the performance
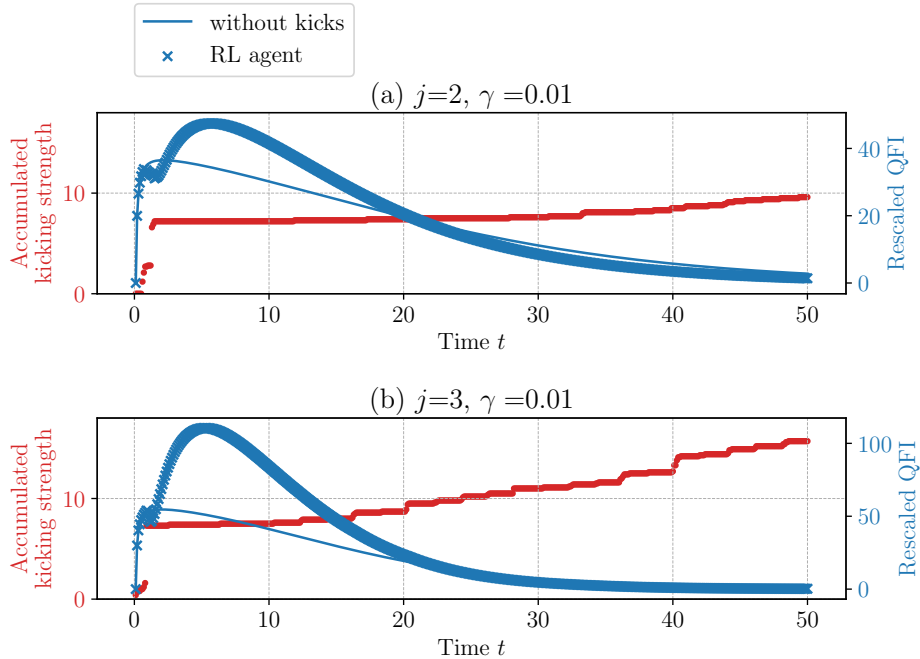
16

FIG. 6. Examples for the policy adopted by the RL agent for maximizing the rescaled quantum Fisher information with superradiant damping. We plot the accumulated kicking strength on the left axis as red dots and on the right axis the rescaled quantum Fisher information for the top (blue solid line) and for the generalized kicked top optimized with reinforcement learning (blue crosses). In case of $j = 2$ ($j = 3$) the strongest kick is applied after an initial rotation angle of $13\pi/20$ ($9\pi/20$).

of the RL agent in connection with another decoherence model, we take a look at phase damping, see Fig. 7. The behavior of the QFI of the PD-T is qualitatively similar to superradiant damping. The introduction of kicks, however, has a qualitatively different effect on the QFI. The RL agent can achieve improvements of the QFI for the PD-GKT at time T_{opt} (the highest time plotted in each panel of Fig. 7) compared with the QFI of the PD-T at the same time. Compared to the superradiant case, improvements are rather small. Notably, the policies applied by the RL agent are also different from superradiant damping; for instance, the RL agent avoids kicks for large parts of the dynamics.
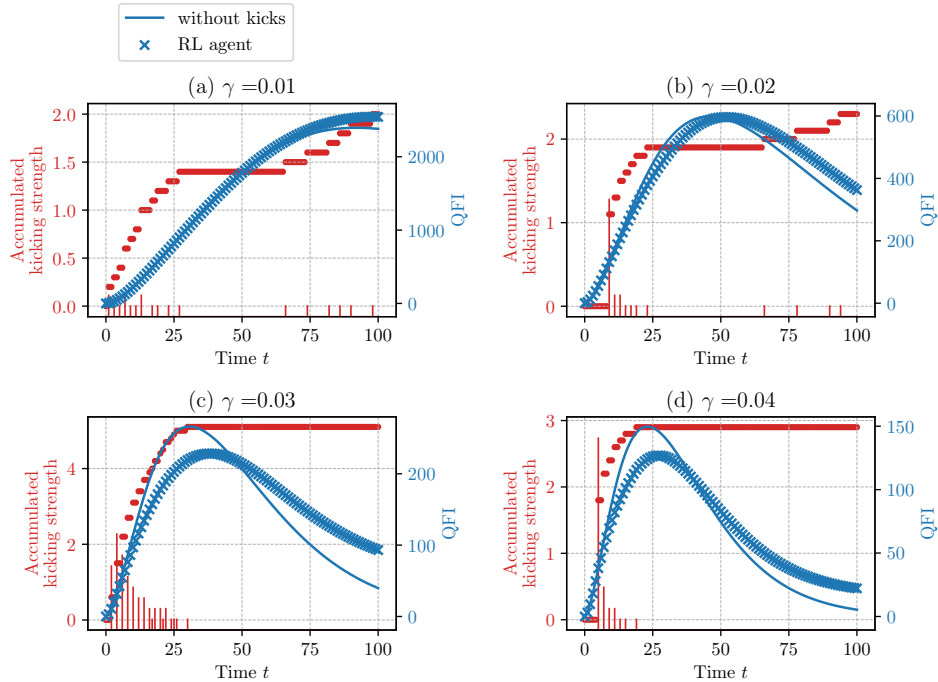
17

FIG. 7. Examples for the strategy adopted by the RL agent for phase damping. All data is for spin $j = 2$ with increasing damping rates γ_{pd} from panel (a) to (d). We plot the accumulated kicking strength on the left axis as red dots and on the right axis the quantum Fisher information for the top (blue solid line) and for the generalized kicked top optimized with reinforcement learning (blue crosses). We additionally plot red vertical lines at times when the RL agent sets a kick. The length of the lines corresponds to the kicking strength in arbitrary units (independent of the scale of the left axis). Note that the RL agent aims to maximize the QFI for $T_{\mathrm{opt}} = 100$ and outperforms the top in all examples.

VI. DISCUSSION

This work builds on recent results on quantum-chaotic sensors [33]. We find that reinforcement learning (RL) techniques can be used to optimize the dynamical control that was used in Ref. [33] to render the sensor dynamics chaotic. The control policies found with RL are tailored to boundary conditions such as the initial state, the targeted measurement time, and the decoherence model under consideration. At the example of superradiant damping we demonstrate improvements in measurement precision and an improved robustness with respect to decoherence. A drawback of RL often lies in the expensive hyperparameter tuning

of the algorithm. However, here we demonstrate that a basic reinforcement algorithm (the cross entropy method) can be used for several choices of boundary conditions with practically no hyperparameter tuning (there was no hyperparameter search necessary, solely parameters that directly influence the computation time were chosen conveniently). Another drawback of RL is its black box character: while the results achieve a good performance the underlying reasons and mechanisms remain hidden. In the example of superradiant damping, we were able to unveil the approach taken by RL by visualizing the quantum dynamics with the help of the Wigner distribution of the quantum state. This revealed that RL favors a policy that is reminiscent of spin squeezing. However, instead of squeezing the state only at the beginning of the dynamics, the squeezing is refreshed and enhanced in roughly periodic cycles in order to fight against the superradiant damping. In the spirit of Ref. [33], these findings emphasize the potential that lies in the optimization of the measurement dynamics. We are optimistic that reinforcement learning will be used in other quantum metrological settings in order to achieve maximum measurement precision with limited quantum resources.

Appendix A: Control problem and optimisation parameters of the examples

Table I shows the parameters of the control problem and for the optimization used in each example. We train n_{agents} RL agents for $n_{\text{iterations}}$ iterations with n_{episodes} episodes in each iteration. Each episode is simulated until a total time T_{opt} is reached. Then we produce n_{samples} sample episodes of each trained RL agent and choose the best episode to plot the sample policies and gains.

TABLE I. Hyperparameters used for the examples in the main text.

Figure	n_{agents}	$n_{\text{iterations}}$	n_{episodes}	n_{samples}	t_{step}	k_{step}	T_{opt}
Samples with superradiant damping (Fig. 3)	5	500	50	20	0.2	0.05	100
Gains of superradiant damping (Fig. 5)	20	300	40	20	1.0	0.10	100
Samples of rescaled QFI (Fig. 6)	2	500	50	20	0.1	0.10	50
Samples with phase damping (Fig. 7)	1	1,000	100	1	1.0	0.10	100

Appendix B: Cross entropy reinforcement learning

Here we give further information on the neural network, the cross entropy method, and the pseudocode for the cross entropy method with discrete actions. The code implementation is based on an example by Jan Schaffranek [4].

The input layer of the neural network is defined by the observation. The output layer is determined by the number of actions (two) and we choose 300 neurons in the hidden layer. The layers are fully connected. The hidden layer has the rectified linear unit (ReLU) as its activation function and the output layer has the softmax function as its activation function [56]. As a cost function we choose the categorical cross entropy [56]. The share of best episodes σ_{share} is always 10%. The number of iterations and number of episodes vary for different settings, see Table I for detailed information. For training we use the Adam optimizer [54] with learning rate 0.001.

---

[4] https://www.udemy.com/artificial-intelligence-und-reinforcement-learning-in-python

---

Algorithm: Cross entropy method

Inputs:
Number of iterations $n_{\text{iterations}}$
Number of episodes n_{episodes}
Share of best episodes σ_{share}

Other variables:
Total Reward R
Current Reward r
Observations o
Actions a
Training set S (consists of observations as inputs and actions as labels)

for 1 **to** $n_{\text{iterations}}$:
    for 1 **to** n_{episodes}:
        $R, o, a \leftarrow$ `Play Game`
    end for
    sort episodes according to R
    $S \leftarrow$ best σ_{share} episodes
    train neural network with S
end for

Function `Play Game()`:
    while episode not finished **do**:
        put observation into neural network and receive probabilities of action as output
        choose action according to probability
        add action and observation to a, o
        tell the environment the action choice and receive a new observation o and reward r
        $R \leftarrow R + r$
    end while
    return R, o, a

Appendix C: Learning curve and stability of the algorithm

At the example of the superradiance decoherence model, we study the learning behavior of the cross entropy reinforcement learning algorithm for different training lengths (i.e. number of iterations) and different numbers of episodes per iteration. The results are summarized in Fig. 8. Spin size is $j = 2$ and dissipation rate is $\gamma_{\text{sr}} = 0.02$.

In order to see the influence of the number of iterations, we set the number of episodes to 100 and let 20 different RL agents (with different random seeds) train for various numbers of iterations. The training of a single RL agent takes about one hour at most (for the higher number of iterations) on a desktop computer. We then use each RL agent to produce 20 episodes, giving us 400 episodes for each data point in Fig. 8. We used those episodes to calculate mean and standard deviation of the reward. The results are shown in the panel
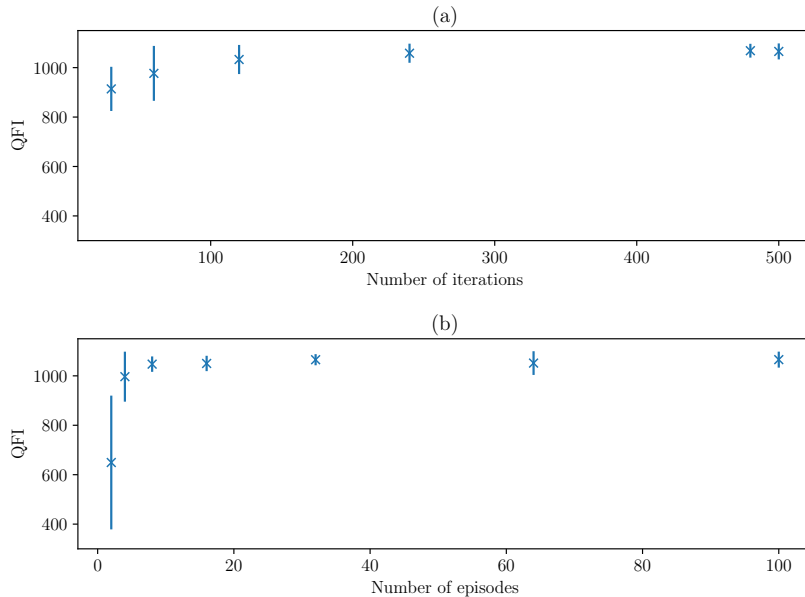
FIG. 8. Learning behavior of the algorithm at the example of superradiant damping with $j = 2$, $\gamma_{\mathrm{sr}} = 0.02$, $k_{\mathrm{step}} = 0.1$, $t_{\mathrm{step}} = 1$, and $T_{\mathrm{opt}} = 100$. Panel (a) shows how the mean QFI and its standard deviation with respect to different runs of the algorithm behaves for various numbers of iterations and fixed number of episodes fixed to 100. In Panel (b) the number of episodes is varied and number of iterations fixed to 500.

(a) of Fig. 8. In order to see the influence of the number of episode in each iteration, we fix the number of iterations to 500 and do the same procedure as before. The results are shown in panel (b) of Fig. 8.

We can see that the standard deviation over policies decreases with the number of iterations while the mean QFI increases. The same is true for the number of episodes (panel (b)), where for 32 episodes a stable plateau of the QFI is reached such that increasing the number of episodes does not achieve any further improvements. Overall, these results demonstrate the stability of the algorithm if the number of episodes and iterations is chosen sufficiently large.

Appendix D: Classical equations of motion

The kicked top with superradiant damping has a well defined classical limit. It is obtained from the quantum equations of motion by taking the limit $j \to \infty$ where $\hbar = 1$ and $\tau = 1$. The

rescaled angular momentum operator $2\boldsymbol{J}/(2j+1) = 2(J_x, J_y, J_z)/(2j+1)$ then becomes the classical coordinate vector $\boldsymbol{r} = (x, y, z)$ and with $\lim_{j\to\infty} \left(\frac{2\boldsymbol{J}}{2j+1}\right)^2 = 1$ the unit sphere becomes the classical phase space with azimuthal angle ϕ and z-coordinate as canonical variables. The equations of motions $\boldsymbol{r} \to \tilde{\boldsymbol{r}}$ are found to be [45]

$$\tilde{x} = x\cos(\alpha) - y\sin(\alpha), \tag{D1}$$

$$\tilde{y} = x\sin(\alpha) + y\cos(\alpha), \tag{D2}$$

$$\tilde{z} = z, \tag{D3}$$

for the precession about the z-axis by an angle α,

$$\tilde{x} = z\sin(ky) + x\cos(ky), \tag{D4}$$

$$\tilde{y} = y, \tag{D5}$$

$$\tilde{z} = z\cos(ky) - x\sin(ky), \tag{D6}$$

for the kicks about the y-axis with kicking strength k, and, with azimuthal angle ϕ (see main text)

$$\tilde{\theta} = \arccos\left(\frac{1 - (\frac{1-z}{1+z}\exp(2\tau))}{1 + (\frac{1-z}{1+z})\exp(2\tau)}\right), \tag{D7}$$

$$\tilde{x} = \sin(\tilde{\theta})\cos(\phi), \tag{D8}$$

$$\tilde{y} = \sin(\tilde{\theta})\sin(\phi), \tag{D9}$$

$$\tilde{z} = \cos(\tilde{\theta}), \tag{D10}$$

for the superradiant damping, where

$$\tau = (2j+1)\gamma_{\mathrm{sr}}t, \tag{D11}$$

for a time t, spin size j, and superradiant decoherence rate γ_{sr}.

Appendix E: A closer look at the kicks set by the reinforcement learning agent

Here we take a closer look at the kicks chosen by the RL agent in the examples with superradiant damping, considered in Fig. 3 in the main text.

In case of $\gamma_{\mathrm{sr}} = 0.01$, for both, $j = 2$ and $j = 3$, we find relatively similar distribution of kicks, see panel (a) in Fig. 9. The most striking difference between the two policies for $j = 2$

and $j = 3$ are the comparatively strong kicks in the beginning of the sequence. By observing the time evolution of the Wigner function (see Supplemental Material), we find that these kicks basically rotate the state by an additional angle $\pi/2$ about the z-axis. This leads to a phase shift of $\pi/2$ between the two policies [see panels (d$_3$) and (d$_4$) of Fig. 10] compared to the initial state [see panels (a$_3$) and (a$_4$) of Fig. 10].

For $\gamma_{sr} = 0.1$ the policies are even more similar with several kicks increasing in strength with a period length of π, see panel (b) in Fig. 9.

Fig. 10 is analog to Fig. 4 in the main text but for $j = 2$ instead of $j = 3$. The only qualitative difference compared to the $j = 3$, is the periodically kicked top: The combination of periodic kicks with $k = 30$ and $j = 2$ seems to be a special configuration. The classical phase space is comparable with the $j = 3$ case, but there is much less structure in the Wigner function. Instead, the state concentrates on the south pole and exhibits a slightly squeezed shape (this is difficult to judge from Fig. 10 though). The rather high value of the QFI for $k = 30$ and $j = 2$, is best explained by this squeezing. When choosing other kicking strength, we observed a Wigner function similar to the case of $j = 3$.
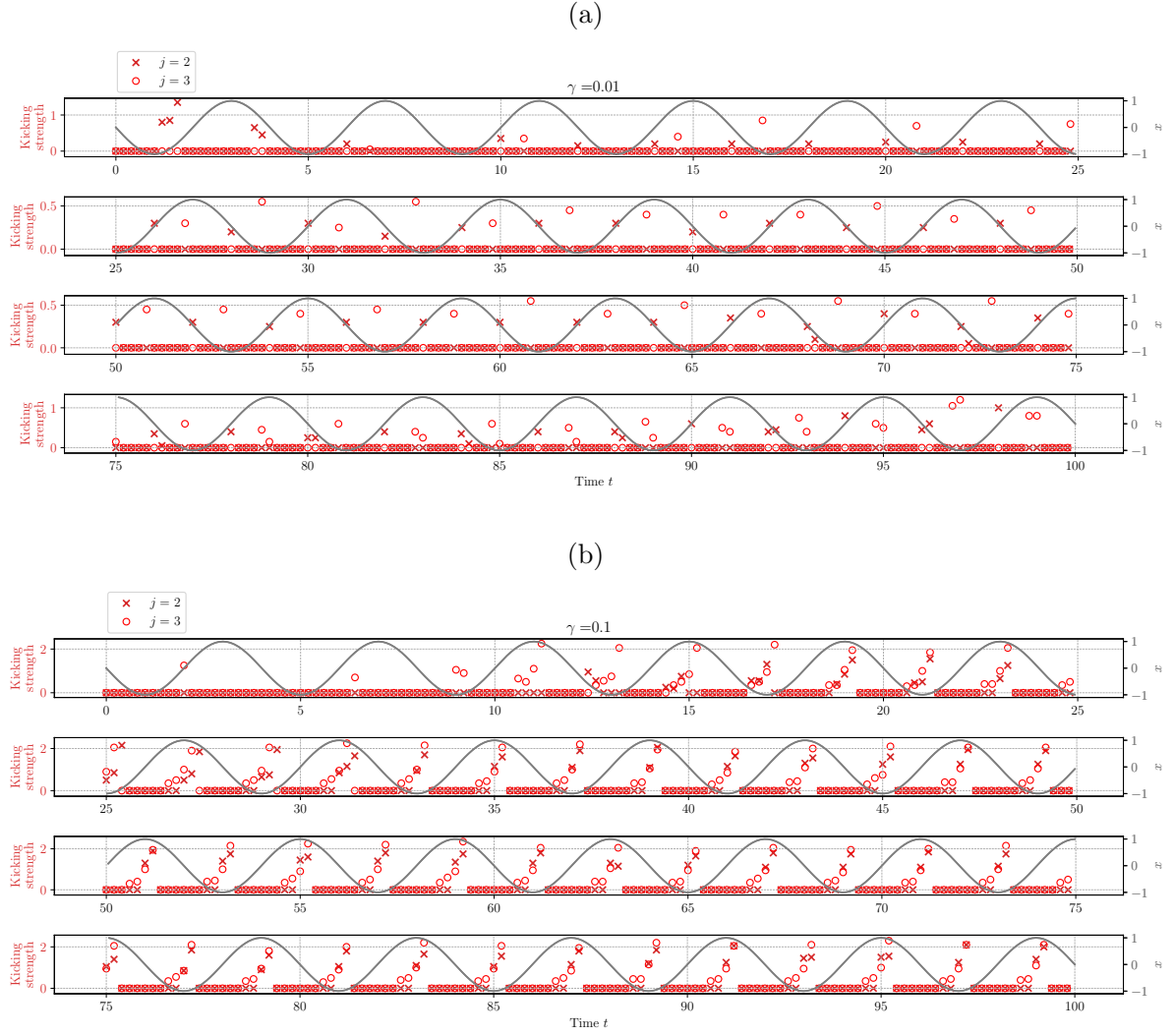
FIG. 9. Kicks set by the RL agent for the SR-GKT. Panel (a) shows the case for $\gamma_{\text{sr}} = 0.01$ and panel (b) for $\gamma_{\text{sr}} = 0.1$. In red on the left axis are the kicking strengths for $j = 2$ (crosses) and $j = 3$ (circles). To show the precession, we plot on the right axis in grey the x component of an unkicked spin coherent state without decoherence.
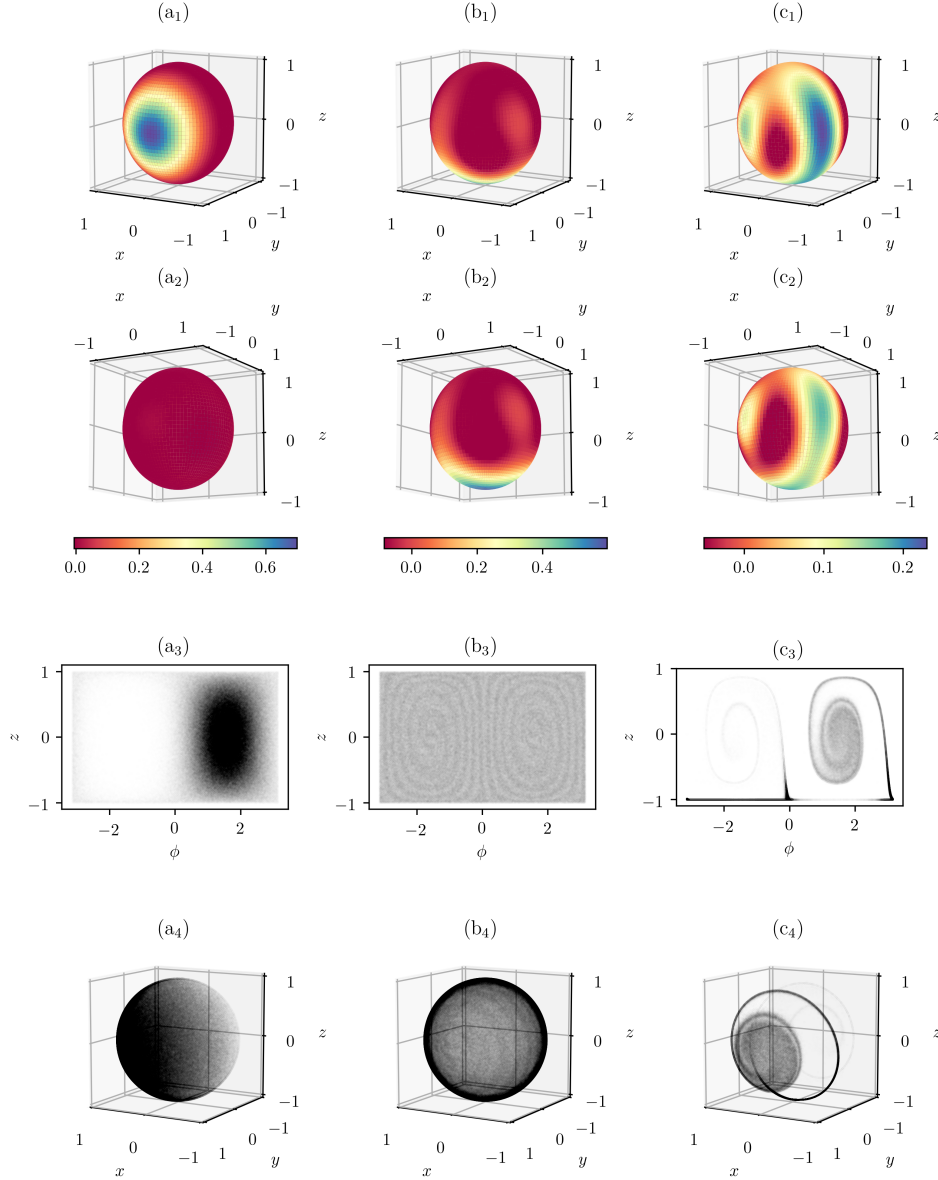
25

FIG. 10. Shows the corresponding data as in Fig. 4 but for $j = 2$ instead of $j = 3$: Illustration of kicked superradiant dynamics with Wigner functions and its classical limit. The dissipation rate is $\gamma_{\mathrm{sr}} = 0.01$. Panels in the left column (a) correspond to the initial spin coherent state at $\theta = \phi = \pi/2$. The middle and right columns correspond to the state at time T_{opt} generated with periodic kicks [middle column (b), $k = 30$] and with kicks optimized with reinforcement learning [right column (c), the corresponding QFI is shown in panel (b) of Fig. 3]. The top two rows show the Wigner functions of the density matrix, the bottom two rows show the classical phase space, populated by 10^6 points initially distributed according to the Husimi distribution of the initial spin coherent state and then propagated according to the classical equations of motion.

[1] K. P. Murphy, *Machine Learning: A Probabilistic Perspective* (MIT press, 2012).

[2] V. Dunjko and H. J. Briegel, Reports on Progress in Physics **81**, 074001 (2018).

[3] P. Mehta, M. Bukov, C.-H. Wang, A. G. Day, C. Richardson, C. K. Fisher, and D. J. Schwab, Physics Reports (2019).

[4] J. Carrasquilla and R. G. Melko, Nature Physics **13**, 431 (2017).

[5] P. Broecker, F. F. Assaad, and S. Trebst, arXiv preprint arXiv:1707.00663 (2017).

[6] E. P. Van Nieuwenburg, Y.-H. Liu, and S. D. Huber, Nature Physics **13**, 435 (2017).

[7] G. Carleo and M. Troyer, Science **355**, 602 (2017).

[8] G. Carleo, Y. Nomura, and M. Imada, Nature communications **9**, 5322 (2018).

[9] X. Gao and L.-M. Duan, Nature communications **8**, 662 (2017).

[10] J. R. Leigh, *Control Theory*, Vol. 64 (Iet, 2004).

[11] L. P. Kaelbling, M. L. Littman, and A. W. Moore, Journal of artificial intelligence research **4**, 237 (1996).

[12] R. S. Sutton and A. G. Barto, *Reinforcement Learning: An Introduction* (MIT press, 2018).

[13] R. S. Sutton, A. G. Barto, and R. J. Williams, IEEE Control Systems Magazine **12**, 19 (1992).

[14] C. Chen, D. Dong, H.-X. Li, J. Chu, and T.-J. Tarn, IEEE transactions on neural networks and learning systems **25**, 920 (2013).

[15] P. Palittapongarnpim, P. Wittek, E. Zahedinejad, S. Vedaie, and B. C. Sanders, Neurocomputing **268**, 116 (2017).

[16] T. Fösel, P. Tighineanu, T. Weiss, and F. Marquardt, Physical Review X **8**, 031084 (2018).

[17] M. Bukov, A. G. Day, D. Sels, P. Weinberg, A. Polkovnikov, and P. Mehta, Physical Review X **8**, 031086 (2018).

[18] F. Albarrán-Arriagada, J. C. Retamal, E. Solano, and L. Lamata, Physical Review A **98**, 042315 (2018).

[19] M. Y. Niu, S. Boixo, V. N. Smelyanskiy, and H. Neven, in *AIAA Scitech 2019 Forum* (2019) p. 0954.

[20] A. A. Melnikov, H. P. Nautrup, M. Krenn, V. Dunjko, M. Tiersch, A. Zeilinger, and H. J. Briegel, Proceedings of the National Academy of Sciences **115**, 1221 (2018).

[21] R. Sweke, M. S. Kesselring, E. P. van Nieuwenburg, and J. Eisert, arXiv preprint arXiv:1810.07207 (2018).

[22] P. Andreasson, J. Johansson, S. Liljestrand, and M. Granath, arXiv preprint arXiv:1811.12338 (2018).

[23] A. Hentschel and B. C. Sanders, in *2010 Seventh International Conference on Information Technology: New Generations* (IEEE, 2010) pp. 506–511.

[24] A. Hentschel and B. C. Sanders, Physical review letters **107**, 233601 (2011).

[25] N. B. Lovett, C. Crosnier, M. Perarnau-Llobet, and B. C. Sanders, Physical review letters **110**, 220501 (2013).

[26] A. Sergeevich and S. D. Bartlett, in *2012 IEEE Congress on Evolutionary Computation* (IEEE, 2012) pp. 1–3.

[27] M. P. Stenberg, O. Köhn, and F. K. Wilhelm, Physical Review A **93**, 012122 (2016).

[28] P. Palittapongarnpim, P. Wittek, and B. C. Sanders, in *24th European Symposium on Artificial Neural Networks, Bruges, April 27–29, 2016* (2016) pp. 327–332.

[29] A. Lumino, E. Polino, A. S. Rab, G. Milani, N. Spagnolo, N. Wiebe, and F. Sciarrino, Physical Review Applied **10**, 044033 (2018).

[30] J. Liu and H. Yuan, Physical Review A **96**, 012117 (2017).

[31] J. Liu and H. Yuan, Physical Review A **96**, 042114 (2017).

[32] H. Xu, J. Li, L. Liu, Y. Wang, H. Yuan, and X. Wang, arXiv preprint arXiv:1904.11298 (2019).

[33] L. J. Fiderer and D. Braun, Nature communications **9**, 1351 (2018).

[34] L. J. Fiderer and D. Braun, in *Optical, Opto-Atomic, and Entanglement-Enhanced Precision Metrology*, Vol. 10934 (International Society for Optics and Photonics, 2019) p. 109342S.

[35] C. W. Helstrom, *Quantum Detection and Estimation Theory* (Academic press, 1976).

[36] A. S. Holevo, *Probabilistic and Statistical Aspects of Quantum Theory* (North-Holland, Amsterdam, 1982).

[37] S. L. Braunstein and C. M. Caves, Phys. Rev. Lett. **72**, 3439 (1994).

[38] M. G. A. Paris, International Journal of Quantum Information **7**, 125 (2009).

[39] A. Peres, *Quantum Theory: Concepts and Methods*, Vol. 57 (Springer Science & Business Media, 2006).

[40] S. Chaudhury, A. Smith, B. Anderson, S. Ghose, and P. S. Jessen, Nature **461**, 768 (2009).

[41] V. Krithika, V. Anjusha, U. T. Bhosale, and T. Mahesh, Physical Review E **99**, 032219 (2019).

[42] R. H. Dicke, Phys. Rev. **93**, 99 (1954).

[43] M. Gross, C. Fabre, P. Pillet, and S. Haroche, Phys. Rev. Lett. **36**, 1035 (1976).

[44] M. Gross and S. Haroche, Phys. Rep. **93**, 301 (1982).

[45] D. Braun, *Dissipative Quantum Chaos and Decoherence*, Springer Tracts in Modern Physics, Vol. 172 (Springer, 2001).

[46] A. Kossakowski, Rep. Math. Phys. **3**, 247 (1972).

[47] G. Lindblad, Math. Phys. **48**, 119 (1976).

[48] R. Bonifacio, P. Schwendimann, and F. Haake, Physical Review A **4**, 302 (1971).

[49] P. A. Braun, D. Braun, and F. Haake, Eur. Phys. J. D **3**, 1 (1998).

[50] P. A. Braun, D. Braun, F. Haake, and J. Weber, Eur. Phys. J. D **2**, 165 (1998).

[51] O. Giraud, P. Braun, and D. Braun, Phys. Rev. A **78**, 042112 (2008).

[52] O. Giraud, P. Braun, and D. Braun, New Journal of Physics **12**, 063005 (2010).

[53] P.-T. De Boer, D. P. Kroese, S. Mannor, and R. Y. Rubinstein, Annals of operations research **134**, 19 (2005).

[54] D. P. Kingma and J. Ba, arXiv preprint arXiv:1412.6980 (2014).

[55] G. S. Agarwal, *Quantum Optics* (Cambridge University Press, 2012).

[56] M. A. Nielsen, *Neural Networks and Deep Learning*, Vol. 25 (Determination press San Francisco, CA, USA:, 2015).

Neural-Network Heuristics for Adaptive Bayesian Quantum Estimation

Lukas J. Fiderer[1], Jonas Schuff[1,2], Daniel Braun[1]

[1]*Eberhard-Karls-Universität Tübingen, Institut für Theoretische Physik, 72076 Tübingen, Germany*
[2]*Department of Materials, University of Oxford, Parks Road, Oxford OX1 3PH, United Kingdom*

Adaptive experiment design is crucial in order to exploit the benefits of Bayesian quantum estimation. We propose and demonstrate a general method for creating fast and strong experiment-design heuristics based on neural networks. Training of the neural networks relies on an evolutionary algorithm and a combination of imitation and reinforcement learning. Based on the well-studied example of frequency estimation with a qubit which suffers from T_2 relaxation, we demonstrate that the trained neural networks are tailored to the properties of the estimation problem and take into account the availability of resources such as time or the number of measurements. The simultaneous estimation of the frequency and the relaxation rate is considered as well. We find that the neural-network heuristics are able to outperform well-established heuristics in all examples.

In quantum metrology we aim to design quantum experiments such that one or multiple parameters can be estimated from the measurement outcomes. Experiment design can involve the preparation of initial states, controlling the dynamics, or choosing measurements for readout. The estimation of parameters is a problem of statistical inference which, broadly speaking, can be tackled with the frequentist or the Bayesian approach.

In the frequentist approach, the experiments are designed *a priori*; repeating experiments several times allows one to estimate the parameters from the statistic of measurement outcomes using, for example, maximum likelihood estimation. The problem of experiment design is often addressed with the Cramér–Rao bound formalism [1, 2] by maximizing the quantum Fisher information with respect to experiment designs [3].

The Bayesian approach, on the other hand, relies on updating the current knowledge about the parameters after each experiment using Bayes' law. Examples for Bayesian quantum estimation involve state and process tomography [4–9], and Bayesian frequency estimation [10–12] with various experimental realizations [13–20]. The Bayesian approach allows for adaptive experiment design: experiments can be optimized depending on the current knowledge about the parameters and the available resources.

While adaptivity can enhance the precision and save time and other resources compared to non-adaptive (frequentist) approaches [21], it involves a computational challenge: The Bayesian update and the consecutive optimization of the experiment design are both analytically intractable (with rare exceptions under idealized conditions [10, 22]) and must be calculated *online*, i.e., after each experiment. In view of the short time scale of quantum experiments, slow numerical computation can drastically increase the total time consumed. In order to approximate the Bayesian update, an efficient framework based on a sequential Monte-Carlo (SMC) algorithm has been developed [6, 7, 23–25]. This framework, however, does not solve the problem of adaptive experiment design, which represents a second computational step, see Fig. 1(a).

Usually, one has to rely on so-called experiment-design heuristics, i.e., fast to evaluate rules for designing experiments, see Fig. 1(a). So far, experiment-design heuristics were mostly chosen manually [11, 26–29], typically motivated by analytic arguments derived for an idealized model [22, 26]. Other approaches numerically optimize with respect to a restricted (in order to keep the problem numerically tractable) set of policies online (between the experiments) [29] or offline (*a priori*) with particle swarm [19, 30–32] or differential evolution algorithms [33]. For example in Refs. [19, 30, 31, 33], the restricted search space grows linearly with the number of measurements N, but the run time grows as $\mathcal{O}(N^6)$ or $\mathcal{O}(N^7)$ (for particle swarm and differential evolution algorithms, respectively) which restricts the optimization to $N \lesssim 100$ due to computational limitations. While for relatively simple cases strong or even close to optimal heuristics were found manually, modifications of the experiments (e.g., a different decoherence rate or even a different decoherence model) or changes in the availability of resources typically lead to a much worse performance of these heuristics.

Here, we propose a method for finding strong and fast heuristics which builds upon and compliments the SMC framework for approximate Bayesian updates [6, 7, 23–25]. The idea is to use a neural network which makes decisions on experiment design based on the current knowledge about the parameters which we want to estimate. The training consists of two steps, see Fig. 1 (b): imitation learning followed by reinforcement learning (RL). The idea of imitation learning is to take advantage of already existing (manually found) heuristics by training a neural network to imitate their behavior. In the second step, which consists of RL, we treat the problem of experiment design as a game: by training the neural network to become a better player we want to create a heuristic (the trained neural network) which outperforms any other (manually found) heuristic. Recently, RL has been used with great success to create programs that play the board games chess and Go better than any other program or human [34]. RL has also been used in quantum
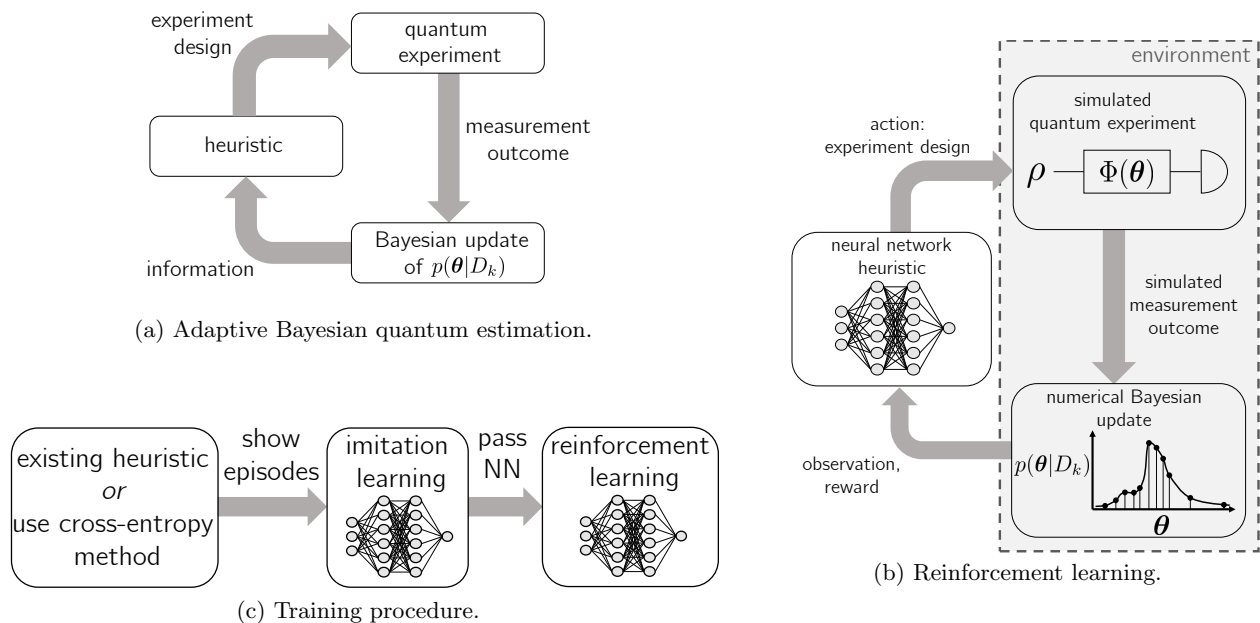
(a) Adaptive Bayesian quantum estimation.

(c) Training procedure.

(b) Reinforcement learning.

FIG. 1: Panel (a) shows the setup for adaptive Bayesian quantum estimation: first, prior information (e.g., about the prior $p(\boldsymbol{\theta})$ and the available resources) is passed to the heuristic which returns an experiment design e_1. With the measurement outcome d_1, we numerically compute the Bayesian update of $p(\boldsymbol{\theta})$. Then, it continues in the same manner and this procedure is repeated until some exit condition is fulfilled (for instance, if a given number of experiments is reached). Panel (b) shows the framework of reinforcement learning, which consists of an agent (depicted as neural network) interacting with a RL environment. The RL environment consists of a simulated quantum experiment [depicted with initial state ρ and parameter-dependent quantum channel $\Phi(\boldsymbol{\theta})$] and a numerical Bayesian update. Panel (c) depicts the training procedure of the neural networks. First, the neural network learns to imitate the behavior of a known heuristic. Then, we use this neural network as a starting point for reinforcement learning.

physics [35, 36] and, in particular, in quantum metrology in the regime of local parameter estimation for improving the dynamics of quantum sensors using cross-entropy [37], actor-critic, and proximal-policy-optimization [38] RL algorithms [39–43].

Before we go into the details of RL, we need to define a figure of merit. Let $\boldsymbol{\theta} = (\theta_1, \dots, \theta_d) \in \Theta$ be the parameters we would like to estimate, and we assume that Θ restricts each θ_j to an interval. Let $D_k = (d_1, \dots, d_k)$ denote the measurement outcomes from a sequence of k independent experiments $E_k = (e_1, \dots, e_k)$, where e_j denotes the design of the jth experiment. Let $p(\boldsymbol{\theta}|D_k)$ (omitting the dependence on experiment designs in the following for the sake of clarity) be a probability distribution on Θ which represents our knowledge about $\boldsymbol{\theta}$ after the kth measurement. Let $\hat{\boldsymbol{\theta}}_k \equiv \hat{\boldsymbol{\theta}}_k(D_k)$ be an estimator of $\boldsymbol{\theta}$ after k experiments. Then, the Bayes risk r is defined (with respect to the loss function $L(\hat{\boldsymbol{\theta}}_k|\boldsymbol{\theta}) = [\|\hat{\boldsymbol{\theta}}_k - \boldsymbol{\theta}\|^2]$) as [11]

$$r\left[\hat{\boldsymbol{\theta}}_k, p(\boldsymbol{\theta})\right] = \mathrm{E}_{\boldsymbol{\theta}}\left(\mathrm{E}_{D_k|\boldsymbol{\theta}}\left[\left\|\hat{\boldsymbol{\theta}}_k - \boldsymbol{\theta}\right\|^2\right]\right), \quad (1)$$

which is the expected value $\mathrm{E}_{\boldsymbol{\theta}}[\bullet] = \int_{\Theta} \mathrm{d}\boldsymbol{\theta}\, p(\boldsymbol{\theta})\bullet$ over the

prior $p(\boldsymbol{\theta}) \equiv p(\boldsymbol{\theta}|0)$ of the risk function $\mathrm{E}_{D_k|\boldsymbol{\theta}}\left[L(\hat{\boldsymbol{\theta}}_k|\boldsymbol{\theta})\right]$. $p(\boldsymbol{\theta})$ represents our knowledge prior to the first measurement. As an estimator $\hat{\boldsymbol{\theta}}_k$ after k experiments we simply use the expected value of $\boldsymbol{\theta}$ over the posterior $p(\boldsymbol{\theta}|D_k)$, $\hat{\boldsymbol{\theta}}_k = \mathrm{E}_{\boldsymbol{\theta}|D_k}[\boldsymbol{\theta}]$. In a Bayesian setting, we aim to minimize the Bayes risk and, thus, we want to choose experiment designs which minimize the Bayes risk.

Let us phrase the problem of experiment design in the language of RL, see Fig. 1(c): In RL, training consists of a RL agent interacting with a RL environment by taking actions and receiving observations and rewards in return [44]. Here, the agent is represented by a neural network, and the RL environment consists of a simulated quantum experiment and a numerical Bayesian update of $p(\boldsymbol{\theta}|D_k)$ [6, 7, 23, 25]. One *episode*, i.e., one game, starts with the RL environment initialized with a prior $p(\boldsymbol{\theta})$ and consists of several steps, i.e., agent-environment interactions. It ends if an exit condition is fulfilled, for example, if a resource such as time is exhausted.

The agent's action at the kth step consists of the experiment design e_k. The observation contains information about the current state of the RL environment, and could in principle include the full SMC representation

of $p(\boldsymbol{\theta}|D_k)$. The observation may also include information about the past, such as prior actions, and about resources, such as the remaining time. The reward should reflect the goodness of the behavior (actions) of the agent (larger reward is better) and is used by the RL algorithm to enforce behavior which leads to larger rewards; the RL agent is learning from its experience.

The negative Bayes risk seems to be an obvious choice for a reward function. However, the computation of the Bayes risk is too time-consuming. Instead, we define the reward after the kth experiment as the difference in the traced covariance of $\boldsymbol{\theta}_{k-1}$ and $\boldsymbol{\theta}_k$,

$$R(D_k) = \mathrm{tr}\left(\mathrm{Cov}_{\boldsymbol{\theta}|D_{k-1}}\left[\boldsymbol{\theta}_{k-1}\right]\right) - \mathrm{tr}\left(\mathrm{Cov}_{\boldsymbol{\theta}|D_k}\left[\boldsymbol{\theta}_k\right]\right). \quad (2)$$

Further, we set $\mathrm{tr}\left(\mathrm{Cov}_{\boldsymbol{\theta}}\left[\boldsymbol{\theta}_0\right]\right) = \mathrm{const}$ in the numerical calculations in order to have a stable reward baseline. It worth noting that averaging the accumulated reward after k steps with respect to data D_k yields

$$\mathrm{E}_{D_k}\left[\sum_{j=1}^{k} R(D_j)\right] = \mathrm{const} - \mathrm{E}_{D_k}\left[\mathrm{tr}\left(\mathrm{Cov}_{\boldsymbol{\theta}|D_k}\left[\boldsymbol{\theta}_k\right]\right)\right], \quad (3)$$

and it turns out (see Appendix) that the right-hand side equals the negative Bayes risk up to a constant offset. Thanks to this important property, maximizing the rewards accumulated for one episode minimizes the Bayes risk at least on average (with respect to data D_k). The reward (2) can be computed efficiently within the SMC framework for Bayesian updates.

Let us demonstrate our method of creating neural-network heuristics with an example of a qubit which evolves under the Hamiltonian $H(\omega) = \frac{\omega}{2}\sigma_z$. The qubit is prepared in $|+\rangle = (|0\rangle + |1\rangle)/2$, evolves under $H(\omega)$ for a controllable time t, and is measured in the σ_x basis (assuming a strong projective measurement). Let us further assume that the qubit suffers from an exponential decay of phase coherence, with characteristic time T_2. According to the Born rule, the likelihood of finding an outcome $d \in \{0, 1\}$ (corresponding to the σ_x measurement) can be expressed as [26]

$$p(0|\omega, t, T_2) = \mathrm{e}^{-\frac{t}{T_2}}\cos^2\left(\frac{\omega}{2}t\right) + \frac{1 - \mathrm{e}^{-\frac{t}{T_2}}}{2}, \quad (4)$$

and $p(1|\omega, t, T_2) = 1 - p(0|\omega, t, T_2)$. Eq. (4) defines all relevant properties of the experiment. An experiment design consists of specifying the evolution time t. We consider the following estimation problems: (i) the estimation of ω without decoherence ($T_2 = \infty$, see the top row of panels in Fig. 2), (ii) the estimation of ω with known T_2 relaxation (we consider this problem twice with different values for T_2, see the second and third row of panels in Fig. 2), and (iii) the simultaneous estimation of ω and T_2^{-1} (see the bottom row of panels in Fig. 2). In all cases we consider $\omega \in (0, 1)$ (making the problem dimensionless). Each estimation problem defines a RL environment

which is either *time-limited* or *experiment-limited*. In the former case, the time available to the agent is limited (which defines the episode length), while in the latter case the number of experiments per episode is fixed. In practice, the first case is relevant if time is a limited resource while the second case is relevant if measurements are expensive, for instance, if experiments involve probing sensitive substances such as biological tissue.

The observation after the kth experiment consists of the mean $\mathrm{E}_{\boldsymbol{\theta}|D_k}[\boldsymbol{\theta}]$ and the covariance $\mathrm{Cov}_{\boldsymbol{\theta}|D_k}[\boldsymbol{\theta}]$ over the posterior (which obviously simplifies to the variance for single-parameter estimation), the last 30 actions and the spent time or the number of experiments (for time-limited or experiment-limited RL environments, respectively).

We use an evolutionary algorithm, the cross entropy method (CEM) for continuous action spaces [45, 46] (see Appendix for pseudocode), and a reinforcement learning algorithm, trust region policy optimization (TRPO) [47] as implemented in the python package Stable Baselines [48] (see Appendix for details on the training). CEM uses a randomly initialized neural network with one hidden layer with 16 neurons. In case of TRPO, we initialize the neural network, which has two hidden layers with 64 neurons each, by doing pretraining as implemented in [48]. Pretraining consists of imitation learning, where the neural network is trained to imitate the behavior of a known heuristic by using episodes (actions and corresponding observations and rewards) created with the known heuristic, see also Fig. 1(c).

Several heuristics have been developed for estimation problems (i) and (ii). As an example for an offline (i.e., non-adaptive) strategy, we consider a heuristic which chooses exponentially sparse times [26], $t_k = (9/8)^k$, denoted as *exp-sparse* heuristic in the following. Further, we consider two adaptive heuristics: We define the first one as $t_k = \left\|\mathrm{Cov}_{\boldsymbol{\theta}|D_{k-1}}(\boldsymbol{\theta})\right\|^{-1/2}$ and we will call it σ^{-1} *heuristic*. This actually represents a generalization to multiparameter estimation of a heuristic which was derived for estimation problem (i) (ω estimation, $T_2 \to \infty$) by Ferrie *et al.* [26]. For single-parameter estimation, the σ^{-1} heuristic chooses the times t_k as the inverse standard deviation of $\boldsymbol{\theta}$ over the posterior and is optimal in the asymptotic limit (number of experiments $N \to \infty$). The second adaptive heuristic that we consider is the *particle guess heuristic* (PGH) [11]. It is based on the SMC framework where probability distributions such as $p(\boldsymbol{\theta}|D_k)$ are represented with a particle filter [6] (see Appendix). PGH chooses times as the inverse distance of two particles $\boldsymbol{\theta}_1$ and $\boldsymbol{\theta}_2$ sampled from $p(\boldsymbol{\theta}|D_{k-1})$, $t_k = \|\boldsymbol{\theta}_1 - \boldsymbol{\theta}_2\|_2^{-1}$. In case of single-parameter estimation, PGH is a proxy for the σ^{-1} heuristic but it is faster to calculate (given the particle filter) and introduces additional randomness (compared to the σ^{-1} heuristic).

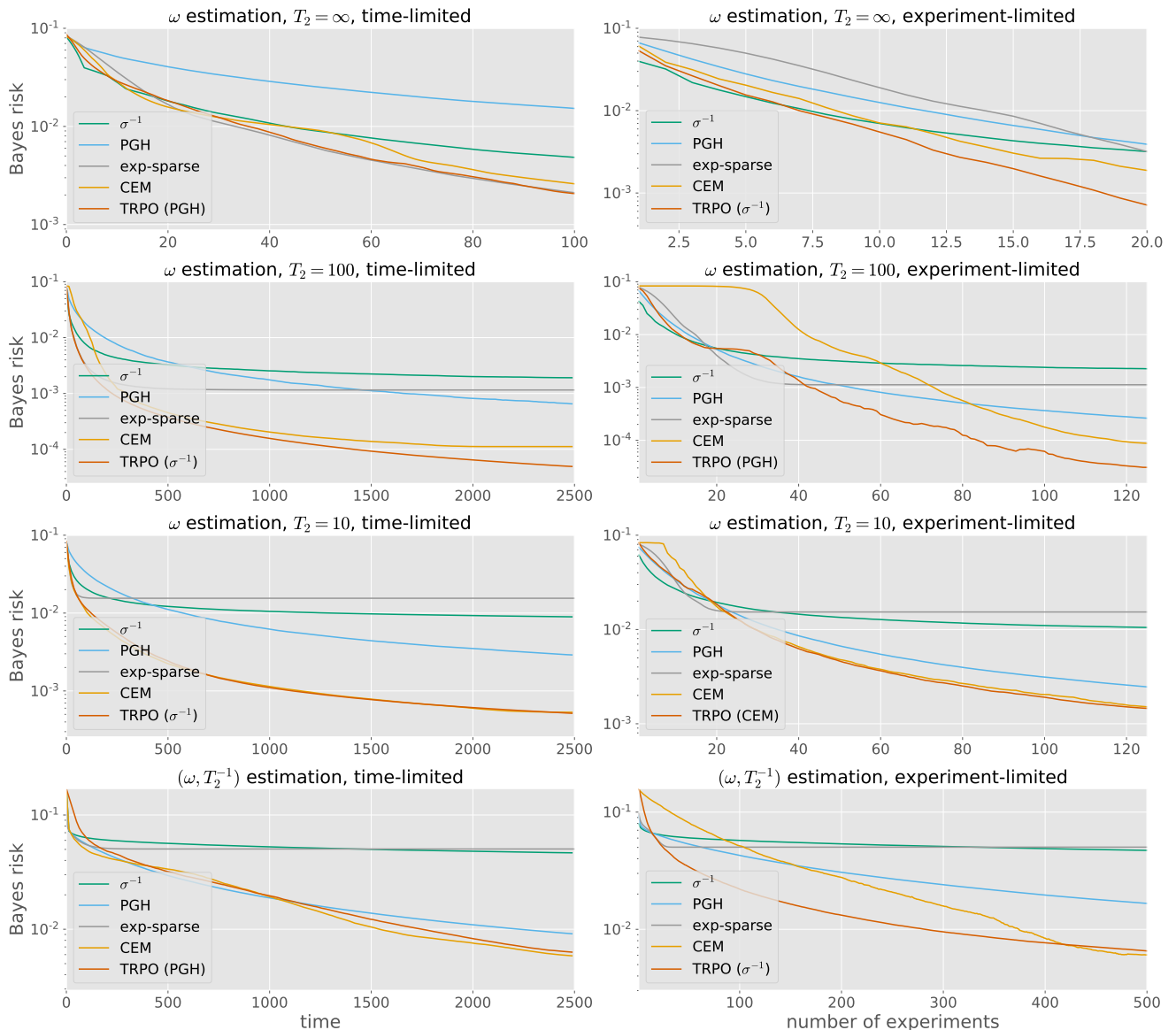We use three different heuristics for the pretraining of

FIG. 2: Comparison of the Bayes risk for different experiment-design heuristics. The left column shows time-limited RL environments, the right column shows RL environments with a limited number of experiments (limited to the maximal value plotted on the x axis, respectively). We study frequency estimation without (top row) and with T_2 relaxation (2nd and 3rd row, with different T_2 as stated in the panel titles) as well as the simultaneous estimation of the frequency ω and relaxation rate T_2^{-1}. The Bayes risk is calculated by averaging $\mathrm{Var}_{\boldsymbol{\theta}|D_k}(\boldsymbol{\theta})$ with respect to 10^4 episodes, sampling for each episode the true parameter(s) from the prior $p(\boldsymbol{\theta})$. For the time-limited RL environment, we interpolate the data for 200 evenly spaced times. TRPO has been pretrained with the heuristic which is specified in brackets in the legends. The lines are linear interpolants to guide the eye.

TRPO: the σ^{-1} heuristic, PGH, and a neural-network heuristic obtained with CEM [49]. Clearly, in the latter case we do not have to rely on known heuristics. The advantage of this two-step procedure over using only one of the RL algorithms is that we can use CEM for exploring the search space (for our RL environments, CEM has proven to be better than TRPO in this respect) and

TRPO for optimizing the heuristic further. Note that CEM considers only accumulated rewards for one episode which means it optimizes only for the maximum time or the maximal number of experiments. TRPO, on the other hand, takes into account rewards at any step of an episode and, therefore, is better suited to train neural networks which are supposed to perform well also for
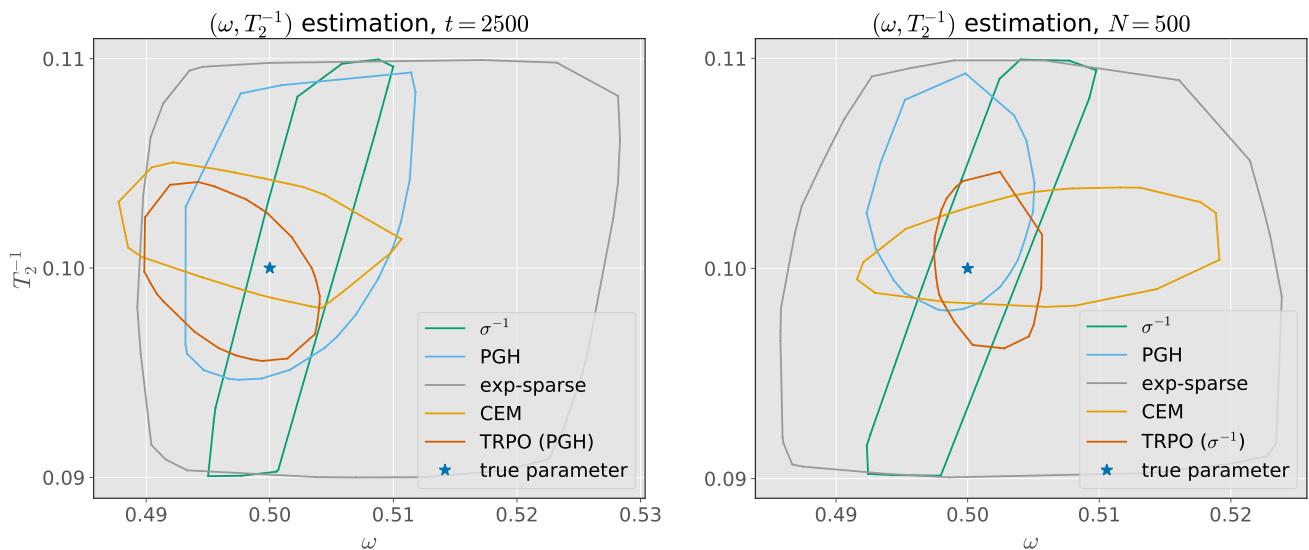
FIG. 3: For the example of (ω, T_2^{-1}) estimation, we plot 95% credible regions for each heuristic from the examples depicted in the bottom row of Fig. 2. The credible regions are obtained by simulating one episode with each heuristic (keeping the true parameter fixed). Then, the credible regions are easily computed from the posterior within the SMC framework. For comparison, the prior is a uniform distribution on $\omega \in (0, 1)$, $T_2^{-1} \in (0.09, 0.11)$.

smaller times or fewer measurements.

Let us turn to the results depicted in Fig. 2. In all examples we consider uniform priors for $\omega \in (0, 1)$. TRPO and CEM outperform the conventional heuristics in all examples for sufficiently large times or sufficiently many measurements.

In the presence of T_2 relaxation, times which exceed T_2 tend to yield no information which explains why the Bayes risk saturates for the exp-sparse heuristic [26]. The largest advantage of neural-network heuristics is obtained at the example of ω estimation with relatively strong relaxation ($T_2 = 100$, second row, left panel in Fig. 2). Compared to PGH, we find an improvement in the Bayes risk by more than a magnitude.

In case of multiparameter estimation we have $T_2^{-1} \in (0.09, 0.11)$ with a corresponding uniform prior. Furthermore, we modify the experiments compared to previous examples in order to facilitate the estimation of T_2^{-1}: here, each experiment produces 100 outcomes at once, and we also give the averaged outcome as an additional observation. Again, the neural networks perform better than the conventional heuristics.

For a single episode, we can visualize the estimation of ω and T_2^{-1} by plotting credible regions corresponding to the heuristics. Fig. 3 shows 95% credible regions obtained with the heuristics used in the panels of the bottom row of Fig. 2.

In conclusion, we propose and demonstrate a method based on imitation and reinforcement learning for training neural networks to become experiment-design heuristics. The practical success of adaptive Bayesian estima-

tion often depends on the run time of the post processing steps. Using neural networks as experiment-design heuristics introduces a computation overhead compared to existing experiment-design heuristics, such as PGH. However, the run time for one call to a neural-network heuristic (trained with TRPO) is comparable to the run time of a Bayesian update (with 1500 particles, single core computation). A speed-up of data processing is expected from implementing the Bayesian update and the neural-network heuristic on a field-programmable gate array [50]. Further, the computational overhead can be reduced by using smaller neural networks or by sacrificing adaptivity in favor of a shorter run time, i.e., by calling the neural-network heuristics only every mth experiment when the neural network would have to return the experiment designs for the next m experiments.

The big advantage of our method is its versatility and adaptivity: the properties of the estimation problem and the quantum experiments, and the availability of resources are encoded in the environment such that the neural networks are trained accordingly. Similarly, we expect that issues with uncertainty in the model or with multimodal probability distributions are automatically taken into account by the trained neural-network heuristics. We provide the complete Python code [51] used for this work in order to facilitate the application of the presented method to other problems such as the detection of time-dependent signals [24, 52] and adaptive Bayesian state tomography [8, 9].

5221/1-1.

––––––––––––

[1] C. W. Helstrom, *Quantum Detection and Estimation Theory*, Mathematics in Science and Engineering, Vol. 123 (Elsevier, 1976).

[2] S. L. Braunstein and C. M. Caves, Statistical distance and the geometry of quantum states, Phys. Rev. Lett. **72**, 3439 (1994).

[3] L. J. Fiderer, J. M. E. Fraïsse, and D. Braun, Maximal Quantum Fisher Information for Mixed States, Phys. Rev. Lett. **123**, 250502 (2019).

[4] V. Bužek, R. Derka, G. Adam, and P. Knight, Reconstruction of Quantum States of Spin Systems: From Quantum Bayesian Inference to Quantum Tomography, Annals of Physics **266**, 454 (1998).

[5] R. Blume-Kohout, Optimal, reliable estimation of quantum states, New Journal of Physics **12**, 043034 (2010).

[6] F. Huszár and N. M. T. Houlsby, Adaptive Bayesian quantum tomography, Phys. Rev. A **85**, 052120 (2012).

[7] C. E. Granade, C. Ferrie, N. Wiebe, and D. G. Cory, Robust online Hamiltonian learning, New Journal of Physics **14**, 103013 (2012).

[8] C. Granade, J. Combes, and D. G. Cory, Practical Bayesian tomography, New Journal of Physics **18**, 033024 (2016).

[9] C. Granade, C. Ferrie, and S. T. Flammia, Practical adaptive quantum tomography, New Journal of Physics **19**, 113017 (2017).

[10] C. Ferrie, C. E. Granade, and D. G. Cory, How to best sample a periodic probability distribution, or on the accuracy of Hamiltonian finding strategies, Quantum Information Processing **12**, 611 (2012).

[11] N. Wiebe, C. Granade, C. Ferrie, and D. G. Cory, Hamiltonian Learning and Certification Using Quantum Resources, Phys. Rev. Lett. **112**, 190501 (2014).

[12] N. Wiebe and C. Granade, Efficient Bayesian Phase Estimation, Phys. Rev. Lett. **117**, 010503 (2016).

[13] K. S. Kravtsov, S. S. Straupe, I. V. Radchenko, N. M. T. Houlsby, F. Huszár, and S. P. Kulik, Experimental adaptive Bayesian tomography, Phys. Rev. A **87**, 062122 (2013).

[14] G. I. Struchalin, I. A. Pogorelov, S. S. Straupe, K. S. Kravtsov, I. V. Radchenko, and S. P. Kulik, Experimental adaptive quantum tomography of two-qubit states, Phys. Rev. A **93**, 012103 (2016).

[15] R. J. Chapman, C. Ferrie, and A. Peruzzo, Experimental Demonstration of Self-Guided Quantum Tomography, Phys. Rev. Lett. **117**, 040402 (2016).

[16] Z. Hou, J.-F. Tang, C. Ferrie, G.-Y. Xiang, C.-F. Li, and G.-C. Guo, Experimental realization of self-guided quantum process tomography, arXiv preprint arXiv:1908.01082 (2019).

[17] J. Wang, S. Paesani, R. Santagati, S. Knauer, A. A. Gentile, N. Wiebe, M. Petruzzella, J. L. O'Brien, J. G. Rarity, A. Laing, and M. G. Thompson, Experimental quantum Hamiltonian learning, Nature Physics **13**, 551 (2017).

[18] S. Paesani, A. A. Gentile, R. Santagati, J. Wang, N. Wiebe, D. P. Tew, J. L. O'Brien, and M. G. Thompson, Experimental Bayesian Quantum Phase Estimation on a Silicon Photonic Chip, Phys. Rev. Lett. **118**, 100503 (2017).

[19] A. Lumino, E. Polino, A. S. Rab, G. Milani, N. Spagnolo, N. Wiebe, and F. Sciarrino, Experimental Phase Estimation Enhanced by Machine Learning, Phys. Rev. Appl. **10**, 044033 (2018).

[20] R. Santagati, A. A. Gentile, S. Knauer, S. Schmitt, S. Paesani, C. Granade, N. Wiebe, C. Osterkamp, L. P. McGuinness, J. Wang, M. G. Thompson, J. G. Rarity, F. Jelezko, and A. Laing, Magnetic-Field Learning Using a Single Electronic Spin in Diamond with One-Photon Readout at Room Temperature, Phys. Rev. X **9**, 021019 (2019).

[21] A. Sergeevich, A. Chandran, J. Combes, S. D. Bartlett, and H. M. Wiseman, Characterization of a qubit Hamiltonian using adaptive measurements in a fixed basis, Phys. Rev. A **84**, 052315 (2011).

[22] A. M. Childs, J. Preskill, and J. Renes, Quantum information and precision measurement, Journal of Modern Optics **47**, 155 (2000).

[23] J. Liu and M. West, Combined Parameter and State Estimation in Simulation-Based Filtering, in *Sequential Monte Carlo Methods in Practice* (Springer New York, 2001) pp. 197–223.

[24] C. Granade, C. Ferrie, I. Hincks, S. Casagrande, T. Alexander, J. Gross, M. Kononenko, and Y. Sanders, QInfer: Statistical inference software for quantum applications, Quantum **1**, 5 (2017).

[25] C. Granade, C. Ferrie, S. Casagrande, I. Hincks, M. Kononenko, T. Alexander, and Y. Sanders, QInfer: Library for Statistical Inference in Quantum Information (2016).

[26] C. Ferrie, C. E. Granade, and D. G. Cory, Adaptive Hamiltonian estimation using Bayesian experimental design, AIP Conference Proceedings **1443**, 165 (2012).

[27] M. P. V. Stenberg, Y. R. Sanders, and F. K. Wilhelm, Efficient estimation of resonant coupling between quantum systems, Phys. Rev. Lett. **113**, 210404 (2014).

[28] I. Hincks, C. Granade, and D. G. Cory, Statistical inference with quantum measurements: methodologies for nitrogen vacancy centers in diamond, New Journal of Physics **20**, 013022 (2018).

[29] I. Hincks, T. Alexander, M. Kononenko, B. Soloway, and D. G. Cory, Hamiltonian Learning with Online Bayesian Experiment Design in Practice, arXiv preprint arXiv:1806.02427 (2018).

[30] A. Hentschel and B. C. Sanders, Machine Learning for Precise Quantum Measurement, Phys. Rev. Lett. **104**, 063603 (2010).

[31] A. Hentschel and B. C. Sanders, Efficient Algorithm for Optimizing Adaptive Quantum Metrology Processes, Phys. Rev. Lett. **107**, 233601 (2011).

[32] M. P. V. Stenberg, O. Köhn, and F. K. Wilhelm, Characterization of decohering quantum systems: Machine learning approach, Phys. Rev. A **93**, 012122 (2016).

[33] N. B. Lovett, C. Crosnier, M. Perarnau-Llobet, and B. C. Sanders, Differential Evolution for Many-Particle Adaptive Quantum Metrology, Phys. Rev. Lett. **110**, 220501 (2013).

[34] D. Silver, T. Hubert, J. Schrittwieser, I. Antonoglou, M. Lai, A. Guez, M. Lanctot, L. Sifre, D. Kumaran, T. Graepel, *et al.*, A general reinforcement learning algorithm that masters chess, shogi, and Go through self-play, Science **362**, 1140 (2018).

[35] V. Dunjko and H. J. Briegel, Machine learning & artifi-

cial intelligence in the quantum domain: a review of recent progress, Reports on Progress in Physics **81**, 074001 (2018).

[36] P. Palittapongarnpim, P. Wittek, E. Zahedinejad, S. Vedaie, and B. C. Sanders, Learning in quantum control: High-dimensional global optimization for noisy quantum dynamics, Neurocomputing **268**, 116 (2017).

[37] P.-T. de Boer, D. P. Kroese, S. Mannor, and R. Y. Rubinstein, A Tutorial on the Cross-Entropy Method, Annals of Operations Research **134**, 19 (2005).

[38] J. Schulman, F. Wolski, P. Dhariwal, A. Radford, and O. Klimov, Proximal policy optimization algorithms, arXiv preprint arXiv:1707.06347 (2017).

[39] J. Liu and H. Yuan, Quantum parameter estimation with optimal control, Phys. Rev. A **96**, 012117 (2017).

[40] J. Liu and H. Yuan, Control-enhanced multiparameter quantum estimation, Phys. Rev. A **96**, 042114 (2017).

[41] H. Xu, J. Li, L. Liu, Y. Wang, H. Yuan, and X. Wang, Transferable control for quantum parameter estimation through reinforcement learning, arXiv preprint arXiv:1904.11298 (2019).

[42] L. J. Fiderer and D. Braun, Quantum metrology with quantum-chaotic sensors, Nature Communications **9**, 1351 (2018).

[43] J. Schuff, L. J. Fiderer, and D. Braun, Improving the dynamics of quantum sensors with reinforcement learning, arXiv preprint arXiv:1908.08416 (2019).

[44] The reward may be obtained only occasionally while each action is followed by an observation.

[45] P.-T. de Boer, D. P. Kroese, S. Mannor, and R. Y. Rubinstein, A Tutorial on the Cross-Entropy Method, Annals of Operations Research **134**, 19 (2005).

[46] D. P. Kingma and J. Ba, Adam: A method for stochastic optimization, arXiv preprint arXiv:1412.6980 (2014).

[47] J. Schulman, S. Levine, P. Abbeel, M. Jordan, and P. Moritz, Trust region policy optimization, in *International conference on machine learning* (2015) pp. 1889–1897.

[48] A. Hill, A. Raffin, M. Ernestus, A. Gleave, A. Kanervisto, R. Traore, P. Dhariwal, C. Hesse, O. Klimov, A. Nichol, M. Plappert, A. Radford, J. Schulman, S. Sidor, and Y. Wu, Stable Baselines, `https://github.com/hill-a/stable-baselines` (2018).

[49] In the case of pretraining with the CEM-trained neural network, it would in principle be easier to directly pass the neural network from CEM to TRPO. However, we use neural networks of different shape (layers and number of neurons) with the two algorithms.

[50] A. R. Omondi and J. C. Rajapakse, *FPGA implementations of neural networks*, Vol. 365 (Springer, 2006).

[51] Add link to repository prior to publication.

[52] M. Isard and A. Blake, Condensation—conditional density propagation for visual tracking, International journal of computer vision **29**, 5 (1998).

[53] A. Doucet and A. M. Johansen, A tutorial on particle filtering and smoothing: Fifteen years later, Handbook of nonlinear filtering **12**, 3 (2009).

[54] S. van der Walt, S. C. Colbert, and G. Varoquaux, The NumPy Array: A Structure for Efficient Numerical Computation, Computing in Science Engineering **13**, 22 (2011).

[55] G. Brockman, V. Cheung, L. Pettersson, J. Schneider, J. Schulman, J. Tang, and W. Zaremba, OpenAI Gym (2016), arXiv:1606.01540.

[56] M. Abadi, A. Agarwal, P. Barham, E. Brevdo, Z. Chen, C. Citro, G. S. Corrado, A. Davis, J. Dean, M. Devin, S. Ghemawat, I. Goodfellow, A. Harp, G. Irving, M. Isard, Y. Jia, R. Jozefowicz, L. Kaiser, M. Kudlur, J. Levenberg, D. Mané, R. Monga, S. Moore, D. Murray, C. Olah, M. Schuster, J. Shlens, B. Steiner, I. Sutskever, K. Talwar, P. Tucker, V. Vanhoucke, V. Vasudevan, F. Viégas, O. Vinyals, P. Warden, M. Wattenberg, M. Wicke, Y. Yu, and X. Zheng, TensorFlow: Large-Scale Machine Learning on Heterogeneous Systems (2015), software available from tensorflow.org.

[57] Currently, pretraining from CEM is not using the best CEM agent but picks one (of the 5) at random. This will be changed in a later version.

[58] M. A. Nielsen, *Neural networks and Deep Learning*, Vol. 25 (Determination press San Francisco, CA, USA, 2015).

The Expected Accumulated Reward and the Bayes Risk

Here we will show that the expected (with respect to data) accumulated reward equals the negative Bayes risk up to a constant offset. In order to simplify the notation, we will omit the dependence on experiment designs E_k.

$$\mathrm{E}_{D_k}\left[\mathrm{tr}\left(\mathrm{Cov}_{\boldsymbol{\theta}|D_k}, [\boldsymbol{\theta}_k]\right)\right] = \mathrm{E}_{D_k}\left(\sum_j \mathrm{Var}_{\boldsymbol{\theta}|D_k}\left[\boldsymbol{\theta}_k^{(j)}\right]\right) \tag{5}$$

$$= \mathrm{E}_{D_k}\left(\sum_j \mathrm{E}_{\boldsymbol{\theta}|D_k}\left[\left(\hat{\boldsymbol{\theta}}_k^{(j)} - \boldsymbol{\theta}_k^{(j)}\right)^2\right]\right) \tag{6}$$

$$= \mathrm{E}_{D_k}\left[\mathrm{E}_{\boldsymbol{\theta}|D_k}\left(\left\|\hat{\boldsymbol{\theta}}_k - \boldsymbol{\theta}\right\|^2\right)\right] \tag{7}$$

$$= \mathrm{E}_{\boldsymbol{\theta}}\left[\mathrm{E}_{D_k|\boldsymbol{\theta}}\left(\left\|\hat{\boldsymbol{\theta}}_k - \boldsymbol{\theta}\right\|^2\right)\right] \tag{8}$$

$$= r\left[\hat{\boldsymbol{\theta}}_k, p(\boldsymbol{\theta})\right], \tag{9}$$

where we used in line (5) that the covariance matrix has the variances of the single parameters on its diagonal, in line (6) we used the definition of the variance and the estimator, in line (7) we interchanged the expected value with the sum in order to rewrite the expression with a vector norm, and in line (8) we used Bayes law to rewrite the expectation values. Line (9) follows with the definition of the Bayes risk. It follows with Eq. (3) from the main text that

$$\mathrm{E}_{D_k}\left[\sum_{j=1}^k R(D_j)\right] = \mathrm{const} - r\left[\hat{\boldsymbol{\theta}}_k, p(\boldsymbol{\theta})\right]. \tag{10}$$

Sequential Monte-Carlo Algorithm for Calculating the Bayesian Update

Bayes rule is given by

$$p(\boldsymbol{\theta}|D_k) = \frac{p(d_k|\boldsymbol{\theta})p(\boldsymbol{\theta}|D_{k-1})}{p(d_k)}, \tag{11}$$

where $p(\boldsymbol{\theta}|D_k)$ is our updated knowledge (posterior), $p(\boldsymbol{\theta}|D_{k-1})$ is our prior knowledge (prior), and $p(d_k)$ is a normalization, $p(d_k) = \mathrm{E}_{\boldsymbol{\theta}}\left[p(d_k|\boldsymbol{\theta})\right]$. The exact solution for the Bayesian update is generally intractable and in particular $p(d_k)$ is hard to calculate. Instead, we use an inference algorithm based on the sequential Monte-Carlo algorithm [6, 7, 53]. The idea is to represent the probability distribution $p(\boldsymbol{\theta}|D_k)$ by a discrete approximation $\sum_{k=1}^n w_k \delta(\boldsymbol{\theta} - \boldsymbol{\theta}_k)$ with n particles with positive weights w_k and positions $\boldsymbol{\theta}_k$. Then, for a Bayesian update, we only need to update the weights of each particle by calculating $p(d_k|\boldsymbol{\theta}_k)$, which means to simulate the experiment for $\boldsymbol{\theta} = \boldsymbol{\theta}_k$ and to use the Born rule, while the expected value in the definition of $p(d_k)$ reduces to a simple sum over the particles. The particle locations need to be resampled if too many weights are close to zero, i.e., the particle filter of $p(\boldsymbol{\theta}|D_k)$ is impoverished. We use Qinfer's[25] implementation of the Liu–West resampling algorithm [23] (with default parameter $a = 0.98$ [25]). We use $n = 2 \times 10^3$ particles for RL environments without decoherence and for RL environments with 2-parameter estimation. For the environments with ω estimation and finite T_2 we use $n = 2 \times 10^4$ particles.

Details on the Training of the Neural Networks

Our results were obtained with NumPy 1.16.4 [54], QInfer 1.0a1 [25], Gym 0.14.0 [55], Stable Baselines 2.8.0 [48], and Tensorflow 1.14.0 [56] libraries for Python 3.6.7.

Trusted Region Policy Optimization

We use TRPO [47] with the MlpPolicy as implemented in Stable Baselines 2.8.0 [48]. Hyperparameters which differ from their default values are $\gamma = 1$, $\lambda = 0.92$ and vf_stepsize = 0.0044. Further, we choose the batch size such that the number of episodes is approximately 1000.

Pretraining uses 10^4 episodes sampled from a heuristic and runs for 10^4 epochs with a batch size of 100 epochs. Training runs for 500 iterations. However, we use an exit condition which can stop the training earlier. The exit conditions stops training if the policy entropy drops below 0.005 [48].

TRPO is pretrained once per heuristics (exp-sparse, σ^{-1}, CEM), and then trained 5 times for each of the pretrainings, and we plot the results in Fig. 2 only for the best neural-network heuristic.

Cross-Entropy Method

CEM is trained 5 times for each RL environment and we plot results in Fig. 2 only for the neural-network heuristic which achieves the smallest Bayes risk after the maximum time or the maximal number of measurements. The input layer of the neural network is defined by the observation. The output layer is determined by the number of actions (one action: time) and we choose 16 neurons in the hidden layer. The layers are fully connected. The hidden layer has the rectified linear unit (ReLU) as its activation function and the output layer has the softmax function as its activation function [58]. The share of best episodes σ_{share} is always 10%. The number of iterations is 1000. Here, we provide pseudocode for cross-entropy method with continuous actions:

Algorithm 1: Cross Entropy Method for Continuous Actions[a]

Result: weights of the neural network
for $i \leftarrow 1$ **to** $NumberOfIterations$ **do**
    for $weight \in WeightsPopulation$ **do**
        $TotalReward \leftarrow$ Play Game;
    end
    sort games according to $TotalReward$;
    $EliteSet \leftarrow$ best X% of games ;
    $BestWeights \leftarrow$ mean weights by averaging over $EliteSet$;
    $WeightsPopulation \leftarrow BestWeights +$ additive random noise
end
Function Play Game():
    while $GameUnfinished$ **do**
        put observation into neural network and receive probabilities of action as output;
        choose action according to probability;
        tell the environment action choice and receive a new observation and reward;
        $TotalReward \leftarrow TotalReward + Reward$
    end
    return $TotalReward$;

---

[a] The implementation of this algorithm is adapted from an example code from the GitHub repository
https://github.com/udacity/deep-reinforcement-learning

Acknowledgements